

# Scanning tunneling spectroscopy of superconductors close to a quantum critical point and at magnetic impurities

**Víctor Barrena Escolar**

Ph.D. thesis  
Universidad Autónoma de Madrid  
Facultad de Ciencias  
2022

*Touch, I remember touch  
Pictures came with touch  
A painter in my mind  
Tell me what you see*

**Daft Punk**

# **Scanning tunneling spectroscopy of superconductors close to a quantum critical point and at magnetic impurities**

**Dissertation submitted in partial satisfaction  
of the requirements for the degree of  
Doctor of Philosophy in Physics**

Víctor Barrena Escolar

2022

Thesis advisers  
Hermann Suderow and Isabel Guillamón  
Universidad Autónoma de Madrid

# Agradecimientos

Siempre fui más de números que de letras. Cualquier intento de plasmar todas las cosas que le agradezco a la gente que me rodea en unos párrafos es injusto, pues si bien para los mencionados serán más de las necesarias, para mí serán ciertamente menos de las merecidas. Me enorgullece echar la vista atrás y ver los logros alcanzados en estos 11 años de recorrido universitario que fueron como la vida misma, con sus alegrías, problemas, sorpresas, dudas, risas, decepciones y esperanzas. Tener a gente tan maravillosa a mi lado fue el impulso que me trajo hasta aquí y que, estoy convencido, me llevará tan lejos como me proponga. Porque esa rueda que es la vida sigue girando, y nuevas aventuras aguardan.

En primer lugar, tengo muchísimo que agradecer a Isabel y Hermann. Para mi sois un ejemplo de talento, constancia y pasión por la ciencia que permea todo a vuestro alrededor, y me siento afortunado de haber podido aprender a vuestro lado. Gracias también a todos los profesores que durante la carrera y el doctorado me supieron transmitir el gusto por la física y la investigación; mención a Sebastián Vieira con sus sabios consejos, a José Vicente Álvarez por sus magníficas clases, y un recuerdo para Chema Gómez. De la carrera también me quedo con Bea y Tere, que consiguieron que los 4 años se pasaran sin darnos cuenta.

También le estoy enormemente agradecido a la gente del laboratorio, empezando por el veterano Edwin, cuya alegría contagiosa e infinito tesón hacían que los problemas lo parecieran menos. A mis compañeros de batalla, Fran y Pepe, que desde aquel Cryocourse siempre fueron una mano amiga. A Raquel y Marta, futuro brillante del grupo quienes siempre convertían los ratos libres en buenos ratos. A Beilun, por no acercarse a mi experimento y, ahora en serio, por estar siempre dispuesto a ayudar. A Chema, capitán indiscutible de la armada de técnicos y voz de la sabiduría. A Sara, por ser todo ternura y dominar como nadie al vidrio y los elementos. A Rafa, por todas las manos que me has echado y todos los km recorridos y por recorrer. A toda la gente que pasó por el laboratorio y lo hizo un poquito mejor: Andrés, Laura, Thomas, David y en especial a Antón, cuya paciente mentoría me ayudó muchísimo en los siempre difíciles comienzos. My deepest gratitude to all the people at Ames that made awesome my stay there: Paul, William, Gil, Scott, Eduar, Na Hyun... You have a home in Madrid.

No sería quien soy sin mis amigos del barrio, quienes consiguen aguantarme nadie sabe cómo y dibujarme una sonrisa por muchos años que pasen o distancia que nos separe. Gracias a Nacno, Julia y Román por convertir la casa de la Gallina en un hogar. A Recio y Tomás, porque si os quiero más me revienta el pecho. A Hueso, Crespo, Puerta, Duri, Pablo, Esther, Lucía, Celia, Sara, Ale, Paula, Bárbara,

## *Agradecimientos*

Charlie, Rodro, Jimbo, Casela, los Guillemos y todos los que me dejo, por estar siempre ahí, porque cada finde con vosotros es un bálsamo para el alma. Gracias también a la bellísima gente de Eresma y Piedralaves con quien he tenido el privilegio de compartir camino durante más o menos años.

Por último, no existen palabras para expresar lo agradecido que le estoy a mi familia por todo lo que es y todo lo que me ha hecho ser. Gracias a mis abuelos, tíos y primos por quererme incondicionalmente. A mi hermano por demostrarme que se puede ser un pesado y que aún así te quieren con locura. A mi madre, porque gracias a su inteligencia y amor infinitos siento que puedo con todo. A mi padre porque sé que estaría orgulloso de mí. Y por último a Irene, porque te quiero tanto que no me cabe en el papel. Si he podido terminar esto es gracias a ti. Lo tenemos todo por delante, y nada me gustaría más que vivirlo contigo.

# Contents

<b>Agradecimientos</b>	<b>i</b>
<b>Abstract</b>	<b>vi</b>
<b>Resumen</b>	<b>viii</b>
<b>1 Introduction</b>	<b>1</b>
1.1 Superconductivity . . . . .	1
1.1.1 Discovery and brief history . . . . .	1
1.1.2 London and Ginzburg-Landau theories . . . . .	2
1.1.3 BCS theory . . . . .	5
1.1.4 Multiband and anisotropic superconductivity . . . . .	7
1.2 Superconductors and magnetic interactions . . . . .	8
1.2.1 Orbital interactions: vortices . . . . .	8
1.2.2 CdGM states in vortex cores . . . . .	10
1.2.3 Vortex core size . . . . .	10
1.2.4 Exchange interaction . . . . .	12
1.2.5 YSR bound states . . . . .	13
1.3 Iron based superconductors . . . . .	14
1.3.1 General electronic properties of iron based superconductors . . . . .	15
1.3.2 Quantum criticality in iron based superconductors . . . . .	17
1.4 The Josephson effect . . . . .	18
1.4.1 The Josephson equations . . . . .	18
1.4.2 The RCSJ model . . . . .	20
1.5 Transition metal dichalcogenides . . . . .	21
1.5.1 The 2H-NbSe <sub>2-x</sub> S <sub>x</sub> system . . . . .	21
1.6 Scope of this work . . . . .	23
<b>2 Experimental Methods</b>	<b>25</b>
2.1 The dilution refrigerator . . . . .	25
2.1.1 Principle of operation . . . . .	25
2.1.2 Improvements to the setup . . . . .	28
2.2 STM at low temperatures . . . . .	31
2.2.1 New micrometric cleaving method . . . . .	33
2.2.2 Image acquisition . . . . .	34
2.3 Synthesis of intermetallic single crystals . . . . .	36
2.3.1 Flux growth of binary intermetallic compounds . . . . .	36

## Contents

2.3.2	International stay at AmesLab . . . . .	38
2.3.3	Growth and characterization of crystals of iron based superconductors: 1144 and Ba122 systems. . . . .	39
2.4	Interpretation of patterns in images of the density of states . . . . .	41
2.4.1	Scanning Tunneling Spectroscopy . . . . .	41
2.4.2	Quasi-Particle Interference imaging . . . . .	42
2.4.3	QPI analysis software . . . . .	44
2.4.4	The autocorrelation function . . . . .	45
2.4.5	The Lawler-Fujita algorithm . . . . .	47
<b>3</b>	<b>Superconductivity and quantum criticality: the <math>\text{BaFe}_2(\text{As}_{1-x}\text{P}_x)_2</math> system</b>	<b>50</b>
3.1	The $\text{BaFe}_2(\text{As}_{1-x}\text{P}_x)_2$ system . . . . .	50
3.2	STM in $\text{BaFe}_2(\text{As}_{0.7}\text{P}_{0.3})_2$ and $\text{BaFe}_2(\text{As}_{0.56}\text{P}_{0.44})_2$ . . . . .	52
3.2.1	Fermi surface . . . . .	53
3.2.2	Nodal superconducting gap . . . . .	54
3.2.3	Vortex lattice . . . . .	55
3.2.4	Vortex cores at the quantum critical point . . . . .	58
3.2.5	Vortex core size vs magnetic field . . . . .	59
3.2.6	Vortex cores in the quantum limit . . . . .	60
3.3	Quasiparticle interference measurements . . . . .	62
3.4	Conclusion . . . . .	64
<b>4</b>	<b>Feedback driven AC Josephson effect</b>	<b>65</b>
4.1	Dynamic Josephson effect observed with STM . . . . .	65
4.1.1	DC Josephson effect . . . . .	65
4.1.2	Low frequency AC Josephson effect . . . . .	66
4.1.3	Low frequency AC Josephson effect in other junctions . . . . .	71
4.2	Model for the low frequency AC Josephson effect . . . . .	71
4.2.1	Delayed feedback-driven RCSJ model . . . . .	71
4.2.2	Dynamics at the Josephson and the feedback frequencies . . . . .	73
4.3	Conclusion . . . . .	74
<b>5</b>	<b>Correlations and bound states in <math>2\text{H-NbSe}_{1.8}\text{S}_{0.2}</math></b>	<b>75</b>
5.1	YSR states in $2\text{H-NbSe}_2$ : state of the art . . . . .	76
5.2	Spatial extension of YSR states in $2\text{H-NbSe}_{1.8}\text{S}_{0.2}$ at zero magnetic field	77
5.2.1	Influence of S doping . . . . .	77
5.2.2	Oscillatory pattern of YSR states in $2\text{H-NbSe}_{1.8}\text{S}_{0.2}$ . . . . .	78
5.2.3	Gapless superconductivity in areas with a very large concentration of Fe impurities . . . . .	83
5.2.4	Discussion . . . . .	85
5.3	Vortex cores with magnetic impurities in $2\text{H-NbSe}_{1.8}\text{S}_{0.2}$ and $2\text{H-NbSe}_2$	86
5.3.1	Asymmetric vortex cores in presence of magnetic impurities in $2\text{H-NbSe}_{1.8}\text{S}_{0.2}$ and $2\text{H-NbSe}_2$ . . . . .	87
5.3.2	Theoretical model for the CdGM - YSR coupling . . . . .	89
5.3.3	Discussion . . . . .	90
5.4	Conclusion . . . . .	91

*Contents*

<b>6 General conclusions</b>	<b>92</b>
<b>7 Conclusiones generales</b>	<b>94</b>
<b>Publications</b>	<b>96</b>
<b>Bibliography</b>	<b>98</b>

# Abstract

Immediately after discovering superconductivity in Pb, H. Kamerlingh Onnes tried to wind a Pb wire to make a magnet and obtain very high magnetic fields. He wanted to address an application with his discovery, aiming at building dissipation-free electrical motors. He rapidly saw, however, that superconductivity disappeared as soon as the current in the solenoid created a field of a few tens of Gauss. His disappointment led him to center efforts in a more fundamental study of superconductivity. But his observation already pointed out a relevant fundamental aspect of superconductivity, developed by Ginzburg 40 years later, namely that superconductivity and magnetism are antagonistic phenomena.

This antagonism provides an interesting playground in modern superconductivity, as there are many situations where it might turn into a positive interaction, often connected with an increase in the critical temperature. In that sense, Kamerlingh Onnes' disappointment was leading us to high critical temperature superconductivity! In this Ph.D. thesis I have explored this issue using scanning tunneling microscopy (STM). STM provides an atomic view of the superconducting properties. I chose to study  $\text{BaFe}_2(\text{As}_{1-x}\text{P}_x)_2$ , a system where superconductivity has maximum  $T_c$  exactly at the P concentration where magnetism disappears (at  $x = 0.3$ ), and isolated magnetic impurities in  $2\text{H-NbSe}_{2-x}\text{S}_x$ . In the course of my studies, I also explored the Josephson effect at atomic level and found features that are completely new.

In the iron based pnictide superconductors, I have analyzed a sample exactly at the quantum critical point where magnetism disappears,  $\text{BaFe}_2(\text{As}_{0.7}\text{P}_{0.3})_2$ , and another sample in the paramagnetic state,  $\text{BaFe}_2(\text{As}_{0.56}\text{P}_{0.44})_2$ . Contrary to other doped superconductors, here the As by P substitution does not influence significantly the sample quality. I have observed the As/P atomic lattice and for the first time the vortex lattice in both samples. In  $\text{BaFe}_2(\text{As}_{0.7}\text{P}_{0.3})_2$ , I find a strong tendency to form a well ordered square vortex lattice locked to the atomic lattice, connected to a strong superconducting gap anisotropy. These effects are absent in  $\text{BaFe}_2(\text{As}_{0.56}\text{P}_{0.44})_2$ , suggesting that they are caused by magnetism. Furthermore, I have measured the band structure using quasiparticle interference, finding a strong superconducting gap anisotropy in  $\text{BaFe}_2(\text{As}_{0.7}\text{P}_{0.3})_2$ . A careful analysis of the scattering patterns allows us to extract information about the gap opening and the band structure. When analyzing the magnetic field dependence of the vortex core size, I found an increase and a subsequent decrease of the vortex core size at  $\text{BaFe}_2(\text{As}_{0.7}\text{P}_{0.3})_2$ . Such a behavior is absent in  $\text{BaFe}_2(\text{As}_{0.56}\text{P}_{0.44})_2$  and is contrary to the expectation for a usual superconductor, which consists of a magnetic field induced decrease in the vortex core size. The peculiar behavior is related to the properties of isolated vortex

## *Abstract*

cores in  $\text{BaFe}_2(\text{As}_{0.7}\text{P}_{0.3})_2$ , which are, at low fields, in the so-called quantum limit, where the core level spacing exceeds the thermal energy. This is an interesting consequence of the diverging mass at the quantum critical point.

I furthermore analyzed the transition metal dichalcogenides  $2\text{H-NbSe}_2$  and  $2\text{H-NbSe}_{1.8}\text{S}_{0.2}$  with Fe magnetic impurities. I show that we can obtain gapless superconductivity with a very small amount of magnetic impurities in  $2\text{H-NbSe}_{1.8}\text{S}_{0.2}$ . I carefully analyzed scattering patterns of the in-gap states induced by the Fe magnetic impurities. I found oscillatory patterns due to the Fe impurities that are associated to portions of the band structure with an increased density of states. The oscillatory patterns are absent in pure  $2\text{H-NbSe}_2$ , suggesting that the S concentration reduces the dimensionality, increasing the scattering signal due to a stronger 2D-character. When there are many magnetic impurities, these overlap and lead to gapless superconductivity. Moreover, I studied in detail the interaction between dilute states from Fe impurities and from quantized states inside vortex cores. I found that the electron-hole asymmetric character of Fe impurity states is transferred to the much larger vortex core states through exchange interaction, causing vortex cores to become axially asymmetric in presence of magnetic impurities.

I have also discovered an unexpected low frequency time dependent AC Josephson signal. I have characterized the effect carefully and shown that it is a novel feedback effect acting on the Josephson junction. The feedback provides a significant enhancement of the Josephson coupling observed in the experiment, improving the sensitivity of Scanning Josephson Spectroscopy. It leads to an interesting bistable behavior, in which the junction switches between the usual AC Josephson effect, with a non-zero voltage, and the zero voltage state with a DC Josephson current.

# Resumen

Inmediatamente tras descubrir superconductividad en el Pb, H. Kammerlingh Onnes intentó crear una bobina con un cable de Pb para hacer un electroimán y obtener campos magnéticos muy altos. Quería encontrar una aplicación para su descubrimiento y se propuso construir motores eléctricos sin disipación. No obstante, no tardó en ver que la superconductividad desaparecía tan pronto como la corriente en el solenoide creaba un campo magnético de unas pocas decenas de Gauss. La decepción consiguiente le llevó a estudiar los aspectos más fundamentales de la superconductividad. Su observación, en cualquier caso, ayudó a señalar uno de los puntos más relevantes de la superconductividad, que sería 40 años después desarrollado por Ginzburg, y es que la superconductividad y el magnetismo son fenómenos antagónicos.

Este antagonismo propicia un interesante escenario en la superconductividad moderna, ya que existen numerosas situaciones donde puede tornarse en una interacción atractiva, normalmente asociada a un incremento de la temperatura crítica. En ese sentido, ¡la decepción de H. Kammerlingh Onnes nos abrió el camino hacia la superconductividad de alta temperatura crítica! En esta tesis doctoral he explorado este tema utilizando un microscopio túnel de barrido (STM, por sus siglas en inglés). El STM proporciona una visión atómica de las propiedades superconductoras. He escogido estudiar el sistema  $\text{BaFe}_2(\text{As}_{1-x}\text{P}_x)_2$ , el cual alcanza su máxima  $T_c$  precisamente en la concentración de P donde el magnetismo desaparece (a  $x = 0.3$ ), y también impurezas magnéticas aisladas en el sistema  $2\text{H-NbSe}_{2-x}\text{S}_x$ . En el curso de mi investigación, también he explorado el efecto Josephson a escala atómica, encontrando fenómenos interesantes y completamente novedosos.

En los pnicturos superconductores basados en hierro he analizado una muestra situada exactamente en el punto crítico cuántico en el que el magnetismo desaparece,  $\text{BaFe}_2(\text{As}_{0.7}\text{P}_{0.3})_2$ , y otra en la fase paramagnética,  $\text{BaFe}_2(\text{As}_{0.56}\text{P}_{0.44})_2$ . Al contrario que en otros superconductores dopados, aquí la sustitución de As por P no influye significativamente en la calidad de las muestras. He observado la red atómica de As/P y, por primera vez, la red de vórtices en ambas muestras. En el  $\text{BaFe}_2(\text{As}_{0.7}\text{P}_{0.3})_2$ , he encontrado una fuerte tendencia a formar una red de vórtices cuadrada alineada con los ejes de la red atómica, asociada a una fuerte anisotropía en el gap superconductor. Estos efectos están ausentes  $\text{BaFe}_2(\text{As}_{0.56}\text{P}_{0.44})_2$ , sugiriendo que podrían tener su origen en la proximidad con el orden antiferromagnético. Además, he medido la estructura de bandas utilizando patrones de dispersión de cuasipartículas, confirmando la fuerte anisotropía del gap en  $\text{BaFe}_2(\text{As}_{0.7}\text{P}_{0.3})_2$ . Un estudio detallado de los patrones de dispersión electrónica nos ha permitido obtener

## Resumen

información acerca de la apertura del gap superconductor y la estructura de bandas. He observado en  $\text{BaFe}_2(\text{As}_{0.7}\text{P}_{0.3})_2$  un inesperado aumento y posterior reducción del tamaño del núcleo de los vórtices. Este comportamiento no se observa en  $\text{BaFe}_2(\text{As}_{0.56}\text{P}_{0.44})_2$  y es contrario a lo esperado para un superconductor normal, donde un campo magnético induce una reducción del tamaño del núcleo. Este peculiar fenómeno está relacionado con las propiedades del núcleo de vórtices aislados en  $\text{BaFe}_2(\text{As}_{0.7}\text{P}_{0.3})_2$ , los cuales a bajos campos están en el llamado límite cuántico, donde el espaciado entre niveles excede la energía térmica. Esto es una interesante consecuencia de la divergencia de la masa efectiva en el punto crítico cuántico.

También he estudiado los dicalcogenuros de metales de transición  $2\text{H-NbSe}_2$  y  $2\text{H-NbSe}_{1.8}\text{S}_{0.2}$  con impurezas magnéticas de Fe. He demostrado que se puede obtener superconductividad sin gap con una muy pequeña cantidad de impurezas en  $2\text{H-NbSe}_{1.8}\text{S}_{0.2}$ . He analizado detenidamente los patrones de dispersión de los estados dentro del gap inducidos por las impurezas magnéticas, encontrando patrones oscilatorios debidos a las impurezas de Fe asociados con porciones de la estructura de bandas con una mayor densidad de estados. Estos patrones oscilatorios no aparecen en  $2\text{H-NbSe}_2$  puro, lo que sugiere que la concentración de S reduce la dimensionalidad, incrementando la señal de dispersión electrónica debido a un mayor carácter bidimensional. Cuando hay muchas impurezas magnéticas, éstas solapan y producen superconductividad sin gap. Además, he estudiado en detalle la interacción entre estados localizados asociados a las impurezas magnéticas cuando están muy diluidas y los estados cuantizados dentro de los núcleos de los vórtices. He observado que la asimetría electrón-hueco característica de los estados localizados en la impurezas de Fe se transfiere a los estados del núcleo de los vórtices a través de interacción de canje, provocando dicho núcleo se vuelva axialmente asimétrico en presencia de impurezas magnéticas.

Asimismo, he descubierto una inesperada señal Josephson alterna de baja frecuencia. He caracterizado este efecto y he mostrado que se trata de un novedoso efecto de retroalimentación que actúa sobre la unión. Dicha retroalimentación causa un aumento significativo del acoplamiento Josephson observado en el experimento, mejorando la sensibilidad de la espectroscopía Josephson de barrido, y conduce a un comportamiento biestable muy interesante, en el cual la unión salta entre el efecto Josephson alterno con un voltaje asociado y una corriente Josephson continua a voltaje cero.

# 1 | Introduction

## 1.1 Superconductivity

### 1.1.1 Discovery and brief history

After the first liquefaction of liquid helium in 1908, H. Kammerling-Onnes at the Leiden Laboratory was studying in 1911 the electrical resistivity of metals when decreasing temperature. He discovered an unexpected drop to almost zero resistance for mercury near 4 K [1] (see Fig. 1.1). This drop was reproducible in several coolings and below that special temperature, the value of the resistivity was always unmeasurably small. Mercury was the first, but soon this behavior was also observed in many other materials, and the term *superconductivity* was coined.

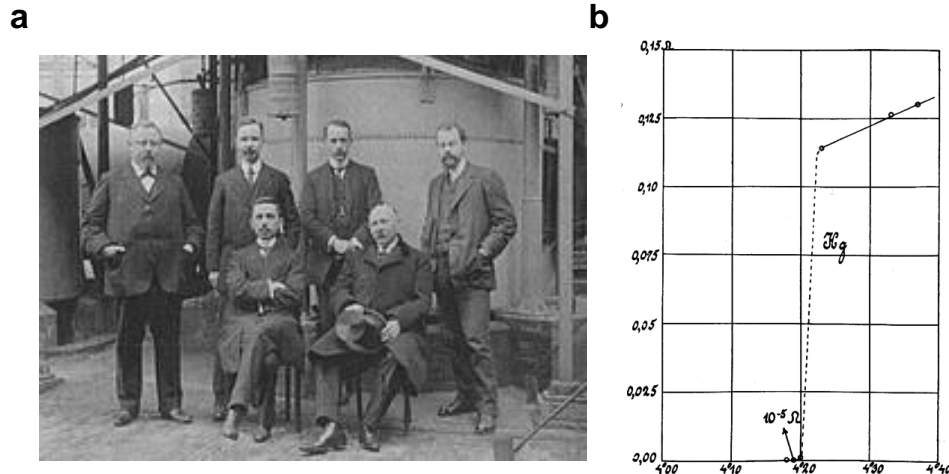


**Figure 1.1:** (a) H. Kammerlingh-Onnes (bottom right) and his team at Leiden Laboratory in 1914. (b) First depiction of the superconducting transition of mercury, extracted from Ref. [1].

Further experiments showed that, in addition to the temperature below which superconductivity appeared (the critical temperature  $T_c$ ), applying a magnetic field lead to the destruction of superconductivity at the critical field  $H_c$ . We can write the difference in free energy between the normal and the superconducting state in

terms of  $H_c$  as:

$$f_N - f_S = \frac{1}{2}\mu_0 H_c^2 \quad (1.1)$$

with  $f_N$  and  $f_S$  being the free energy density of the normal and superconducting state, respectively.

Meissner and Ochsenfeld studied in detail the magnetic field behavior of superconductors [2]. They found that superconductors completely expel the magnetic field. A hypothetical system in which zero resistance appears below a certain temperature would avoid, according to Lenz law, any variation of the magnetic field with time. Thus, if such a sample is at zero field and one applies a magnetic field, the field is expelled. But if one cools such a sample in a magnetic field, nothing happens. In a superconductor, the field is expelled in any case. This is usually referred to as the Meissner effect, which is schematically depicted in Fig. 1.2.

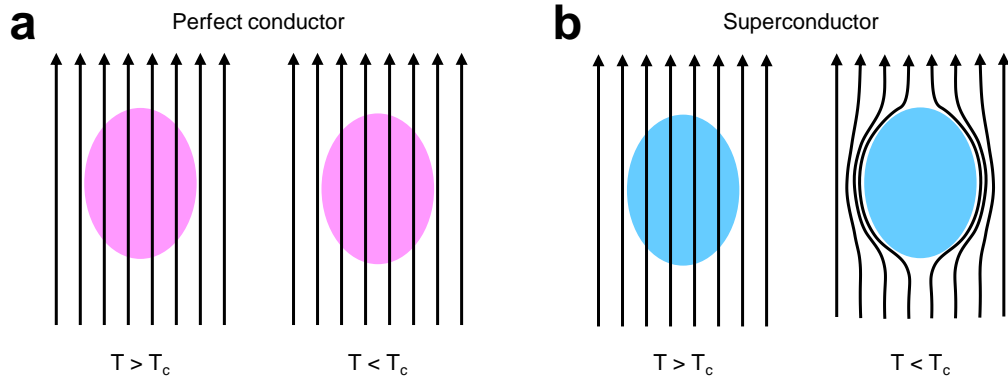


**Figure 1.2:** Comparison of a field cooling process in a perfect conductor (a) and a superconductor (b). Black arrows represent the magnetic flux lines. The superconductor acts as a perfect diamagnet in the Meissner state.

### 1.1.2 London and Ginzburg-Landau theories

The brothers Heinz and Fritz London proposed in 1935 (only two years after Meissner and Ochsenfeld's results) one of the first phenomenological theories to explain superconductivity [3]. The main idea is that external magnetic fields can penetrate inside the superconducting sample a certain characteristic length, called London penetration depth  $\lambda_L$ . These external fields however decay exponentially with distance due to screening by flowing supercurrents, explaining the Meissner effect. The theory can be summarized in the so called London equations:

$$\mathbf{E} = \frac{m_e}{n_s e^2} \frac{\partial \mathbf{J}_s}{\partial t} \quad (1.2)$$

$$\mathbf{H} = -\frac{m_e}{n_s e^2} \nabla \times \mathbf{J}_s \quad (1.3)$$

## Chapter 1 Introduction

where  $m_e$  is the electron mass,  $e$  is the elementary charge and  $n_s$  the density of superconducting electrons. Through the combination of the second London equation and the second Maxwell equation  $\nabla \times \mathbf{H} = \mu_0 \mathbf{J}_s$ , we can extract the solution for the exponentially decaying magnetic field inside a superconductor, from which we can find the London penetration depth:

$$\lambda_L = \sqrt{\frac{m_e}{\mu_0 n_s e^2}} \quad (1.4)$$

A few years later, in 1950, V. Ginzburg and L. Landau worked out a phenomenological quantum model to superconductivity, generally known as the Ginzburg-Landau (GL) theory, based in Landau's study of the thermodynamic properties of phase transitions [4]. They performed a power expansion of the superconducting state's free energy in terms of a small "order parameter", related to the superconducting carrier density  $|\Psi(\mathbf{r})|^2 = n_s$ , which is zero in the normal state and increases continuously in the superconducting state below the critical temperature [5]. According to this framework, the free energy density  $f_s$  of a superconductor can be written as:

$$f_s = \int dr \frac{1}{2\mu_0} (\nabla \times \mathbf{A})^2 - (\nabla \times \mathbf{A}) \mathbf{H} + \alpha |\Psi|^2 + \frac{\beta}{2} |\Psi|^4 + \frac{1}{2m_s} |(i\hbar \nabla + e_s \mathbf{A}) \Psi|^2 \quad (1.5)$$

with  $\mathbf{H}$  the magnetic field,  $\mathbf{A}$  the vector potential,  $e_s$  and  $m_s$  respectively the charge and mass of the superconducting carriers and  $\alpha$  and  $\beta$  material-dependent constants. The so called GL equations can be obtained by minimizing  $f_s$  with respect to  $\mathbf{A}$  and  $\Psi$ :

$$\alpha \Psi + \beta |\Psi|^2 \Psi + \frac{1}{2m_s} (i\hbar \nabla + e_s \mathbf{A})^2 \Psi = 0 \quad (1.6)$$

$$-\frac{i\hbar e_s}{2m_s} (\Psi^* \nabla \Psi - \Psi \nabla \Psi^*) - \frac{e_s^2}{m_s c} |\Psi|^2 \mathbf{A} = \frac{-\nabla^2 \mathbf{A}}{\mu_0} = \mathbf{J} \quad (1.7)$$

These two equations describe the behaviour and coexistence of the normal and the superconducting states in an external magnetic field. The spatial variation of the magnetic field  $\mathbf{H}(\mathbf{r})$  and the order parameter  $\Psi(\mathbf{r})$  is expressed in terms of two characteristic lengths: the penetration depth  $\lambda$  and the coherence length  $\xi$ . The coherence length  $\xi$  is the characteristic distance for spatial variations of  $\Psi$  and the penetration depth  $\lambda$  for spatial variations of  $\mathbf{H}$ . They both have a temperature dependence near  $T_c$  of the type:  $(\lambda, \xi) \propto (T_c - T)^{-\frac{1}{2}}$ . The dimensionless quotient between the two quantities is usually called the Ginzburg-Landau parameter  $\kappa = \lambda/\xi$ .

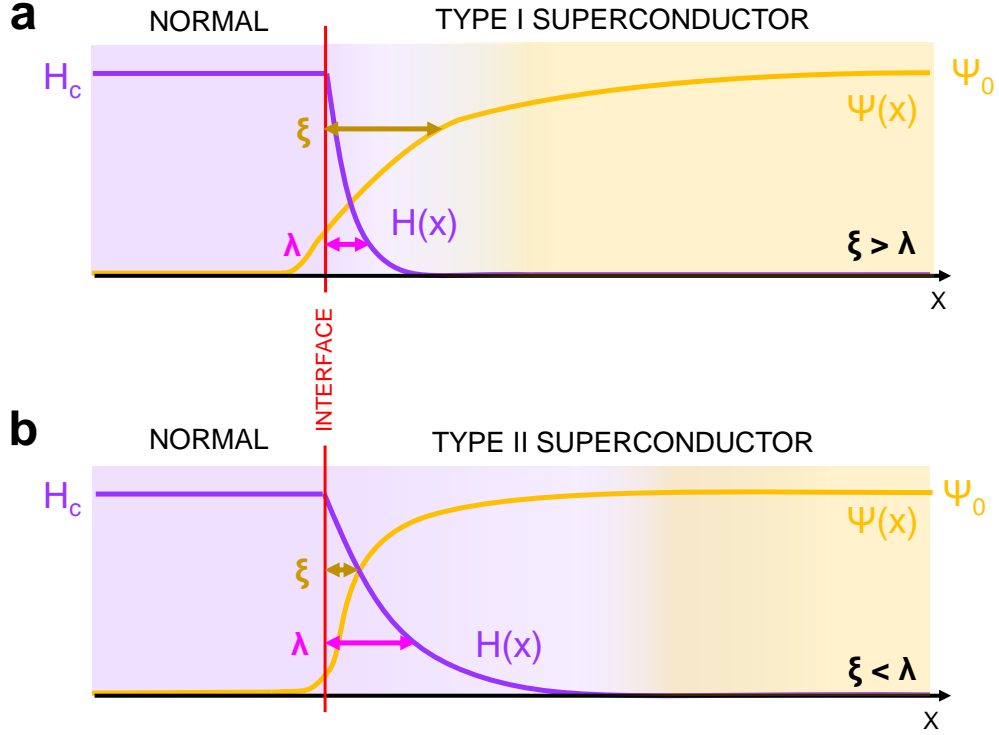


**Figure 1.3:** Schematic diagram of the different behavior of  $\Psi$ ,  $\lambda$  and  $\xi$  in a type I (a) and type II (b) superconductor. We depict the interface between the exterior, where a magnetic field is applied, and the interior of a superconducting sample in the simplest one-dimensional case. In type I superconductors, the magnetic penetration depth is shorter than the superconducting coherence length, and vice versa for type II.

The superconductors studied in this Ph.D. are type II, which have  $\xi < \lambda$  (Fig. 1.3) and allow for the penetration of the magnetic field in the form of flux tubes called vortices (Fig. 1.4). Each carries exactly one flux quantum  $\Phi_0 = h/2e = 2.07 \times 10^{-15} \text{ T}\cdot\text{m}^2$ .

The value of the critical field for type I superconductors in GL theory is:

$$H_c = \frac{\Phi_0}{\sqrt{8\pi\lambda\xi}} \quad (1.8)$$

For type II superconductors, the values for the two critical fields are:

$$H_{c1} = \frac{\Phi_0}{4\pi\lambda^2} \ln \kappa \quad (1.9)$$

$$H_{c2} = \frac{\Phi_0}{2\pi\xi^2} \quad (1.10)$$

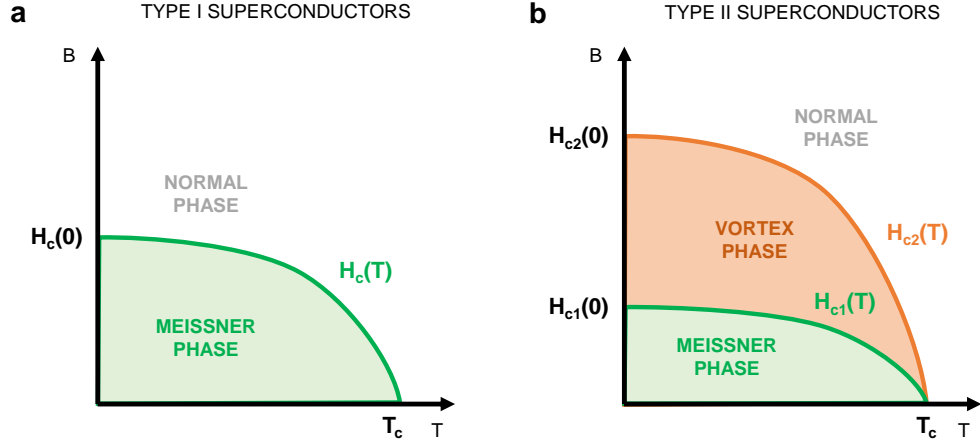


**Figure 1.4:** Temperature-magnetic field phase diagrams of type I (a) and type II (b) superconductors. Both have, below a certain critical field, a Meissner state in which all magnetic field is screened. Above this critical field, type I superconductors transit into the normal state. Type II superconductors however have an intermediate phase between the Meissner and the normal states, called the vortex phase, where magnetic field is able to penetrate the sample through small tubes of quantized flux, called vortices.

### 1.1.3 BCS theory

L. N. Cooper proved [6] that the Fermi sea is unstable to an arbitrarily small attractive potential, which if present would lead to the formation of bound states of electron pairs with opposite spin and momenta, named Cooper pairs. Bardeen, Cooper and Schrieffer then associated this attractive potential to the creation of Cooper pairs through a retarded interaction (Fig. 1.5). Subsequently, it was shown that Cooper pairs can be, in principle, obtained through magnetic interactions and even through purely electronic interactions [7, 8].

In the BCS formalism, the dispersion relation of the excited states  $E_k$  in a superconducting ground state is given by:

$$E_k = \sqrt{\Delta^2 + \varepsilon_k^2} \quad (1.11)$$

where  $\varepsilon_k = (\hbar^2 k^2 / 2m) - E_F$  is the kinetic energy with respect to the Fermi level and  $\Delta$  is a constant named superconducting gap, which is given by:

$$\Delta = \frac{\hbar \omega_c}{\sinh\left(\frac{1}{N_F V}\right)} \approx 2 \hbar \omega_c e^{-\frac{1}{N_F V}} \quad (1.12)$$

with  $\omega$  the electron frequency,  $N_F$  the density of states at the Fermi level and  $V$  the electron-phonon interaction. The gap in BCS is related to the critical temperature  $T_c$  in K through:

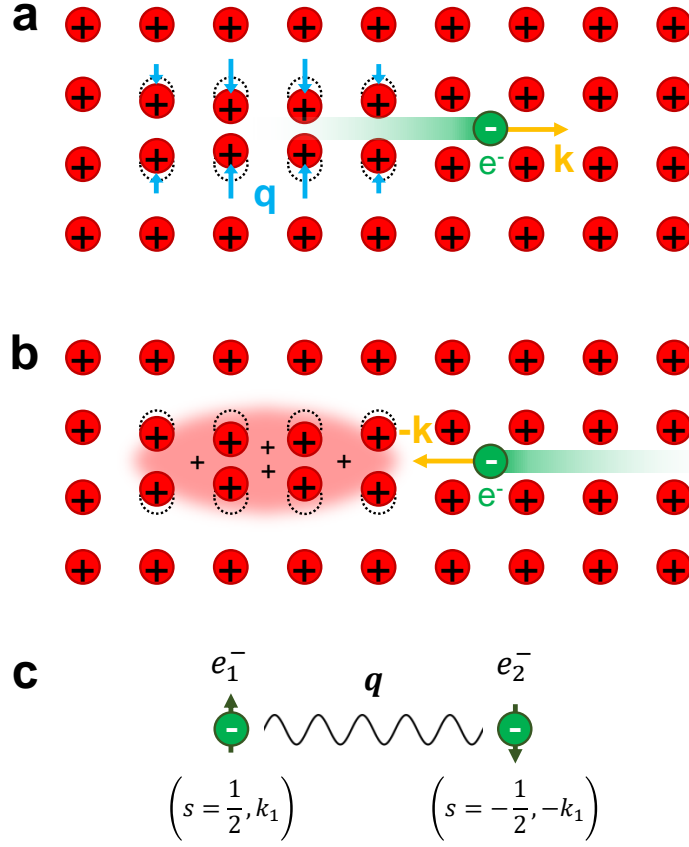


**Figure 1.5:** Retarded phonon-mediated attractive interaction between electrons in the BCS theory. (a) An electron with a certain moment  $k$  will attract the lattice ions towards it and deform the lattice (i.e. excite a phonon) as it travels through it. (b) Another electron with opposite momentum and spin is attracted due to the local accumulation of positive charge. (c) Schematic representation of the electron-phonon interaction, between pairs of electrons with  $k_1 \approx k_F$  and phonons of wavevector  $q$ .

$$\frac{\Delta}{k_B T_c} = \frac{\pi}{e^{\gamma_E}} \approx 1.76 \quad (1.13)$$

with  $\gamma_E \approx 0.577$  the Euler constant. As a rule of thumb,  $\Delta \approx 0.152 T_c$  when  $T_c$  is expressed in K and  $\Delta$  in meV. From the dispersion relation in Equation 1.11 we obtain the BCS density of states (DOS):

$$\frac{N_s(E)}{N_0} = \begin{cases} 0 & \text{if } |E| < \Delta \\ \frac{E}{\sqrt{E^2 - \Delta^2}} & \text{if } |E| > \Delta \end{cases} \quad (1.14)$$

where  $N_s$  is the superconducting density of states and  $N_0$  the density of states of the normal state at the Fermi level. The superconducting gap is maximum at zero temperature and decreases in value with temperature, until it completely disappears at the critical temperature. The behaviour of  $\Delta$  is summarized in Fig. 1.6.

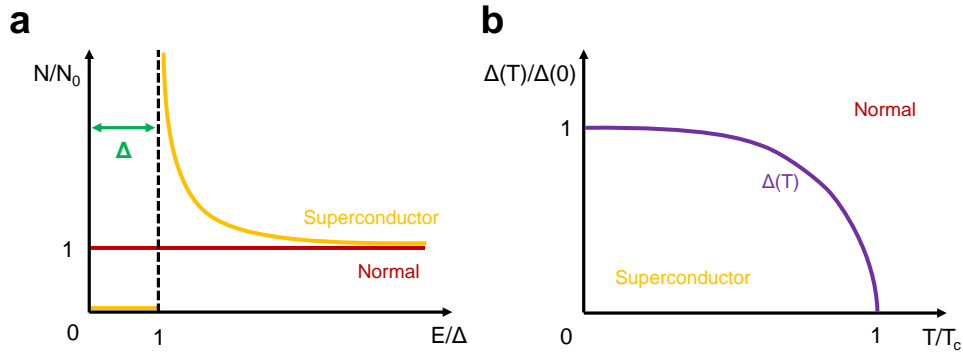


**Figure 1.6:** (a) Schematic representation of the superconducting density of states (orange). The normal density of states is shown as a red line. The superconducting gap  $\Delta$  is highlighted by the green arrow. (b) Temperature dependence of the superconducting gap.

### 1.1.4 Multiband and anisotropic superconductivity

BCS theory starts in its simplest version with a fully isotropic, single band Fermi surface with a parabolic dispersion relation. Of course, single crystals of most elements and compounds have more complex band structures. BCS theory can be equally applied in those cases, with a gap which opens at the Fermi level and a density of states which is similar to the BCS expression.

As shown by Suhl, systems with two bands crossing the Fermi level can eventually present different sizes for the superconducting gap in each band [9]. A simplified approach using two gaps describes well many different compounds. It is assumed that the electron-phonon coupling is different in different portions of the Fermi surface. The differences are often well taken into account assuming that there are two effective gap values, appearing as two peaks in the density of states [10, 11]. There is of course just one critical temperature. When electronic interactions between different portions of the Fermi surface are weak, the two peak structure is better developed in the density of states. When interactions are strong, only a single smeared peak is measured in the density of states [12].

A simple method to take into account complex superconducting band structures is to assume a continuous distribution of values of the superconducting gap as:

$$DOS(E) \propto \sum_i \alpha_i \text{Re} \left( \frac{E}{\sqrt{E^2 - \Delta_i^2}} \right) \quad (1.15)$$

where  $\alpha_i$  are the relative weights of each gap  $\Delta_i$ , obtained from each transfer matrix element [13, 14, 15].

One particular case of superconducting gap changes is often discussed in literature in terms of gap nodes. We can schematically show the value of the gap in reciprocal space as in Fig. 1.7(a) for a single band  $s$ -wave superconductor and a spherical Fermi surface. In presence of some anisotropy, the gap may change along one or

more directions, sometimes almost vanishing (Fig. 1.7(b)). When the gap becomes exactly zero along such directions, through a change in the phase of the Cooper pair wavefunctions (Fig. 1.7(c)), we speak about symmetry-imposed nodes in the superconducting gap. The example shown in Fig. 1.7(c) corresponds to *d*-wave superconductivity.

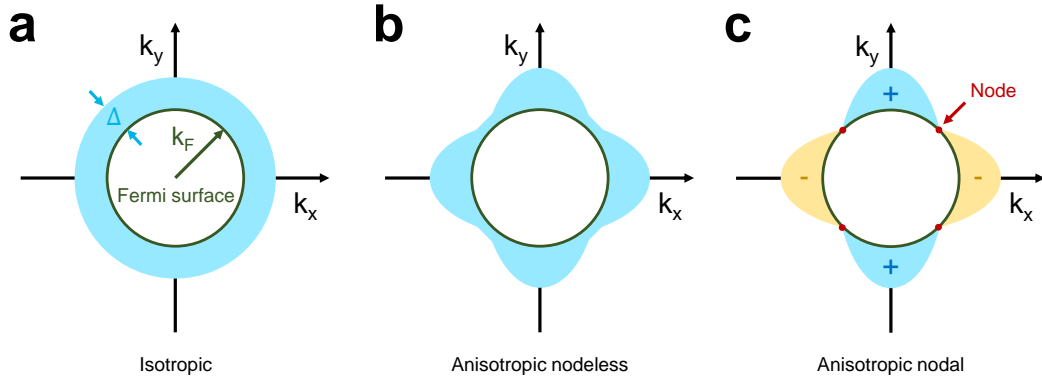


**Figure 1.7:** We show as a blue surface the size of the superconducting gap in a single band superconductor in reciprocal space. In (a) we represent an isotropic, *s*-wave superconducting gap. In (b) we represent a nodeless anisotropic *s*-wave superconducting gap. In (c) we represent a *d*-wave superconducting gap. Note that the phase of the Cooper pair wavefunctions changes sign through a node.

## 1.2 Superconductors and magnetic interactions

### 1.2.1 Orbital interactions: vortices

The interaction between Cooper pairs and the applied magnetic field can be related to the Lorentz force [16]. The rotating Cooper pairs order in a vortex lattice made of flux tubes, which carry supercurrents at a length of order of  $\lambda$ . At the center of each vortex, the Cooper pair wavefunction vanishes on a distance of order of  $\xi$ . We schematically represent the length scales in a vortex in Fig. 1.8(a) and the vortex lattice in Fig. 1.8(b).

The force between two neighbouring vortices at a distance of the order of  $\lambda$  is always repulsive:

$$F = \frac{K_0 a_0}{2\lambda} \left( \frac{\Phi_0}{2\pi\lambda} \right)^2 \quad (1.16)$$

where  $a_0$  is the intervortex distance,  $\lambda$  the penetration depth,  $\Phi_0$  the magnetic flux quantum and  $K_0$  is the Hankel function of order zero. A. Abrikosov predicted in 1957 [17] that vortices would arrange in a lattice, and a triangular lattice with hexagonal symmetry (see Fig. 1.8(b)) was identified in most of the first measurements. More recent research on some very anisotropic tetragonal materials has shown that under

certain conditions, a square lattice might also form [18, 19, 20, 21]. The intervortex distance is a function of the applied magnetic field:

$$a_0^\square(B) = \left(\frac{\Phi_0}{B}\right)^{\frac{1}{2}} \quad (1.17)$$

$$a_0^\Delta(B) = \left(\frac{4}{3}\right)^{\frac{1}{4}} \left(\frac{\Phi_0}{B}\right)^{\frac{1}{2}} \approx 1.075 \left(\frac{\Phi_0}{B}\right)^{\frac{1}{2}} \quad (1.18)$$

with  $a_0^\square$  the intervortex distance for the square lattice and  $a_0^\Delta$  for the hexagonal lattice.

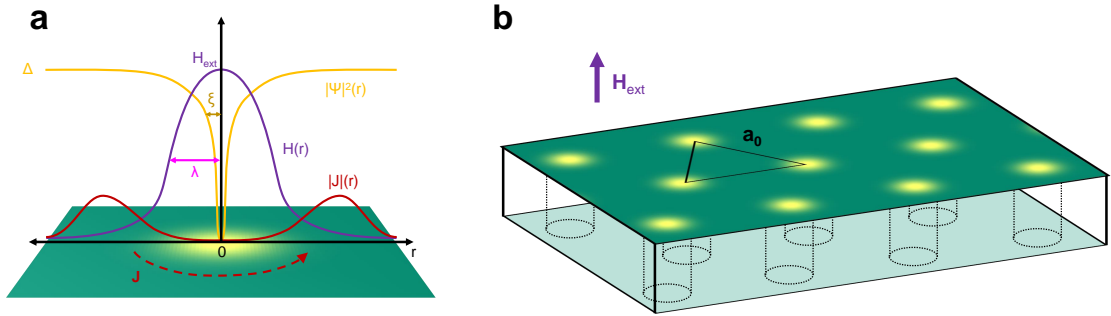


**Figure 1.8:** (a) Schematic representation of the variation of the square of the Cooper pair function (yellow), the magnetic field (purple) and the supercurrents (red) around an isolated vortex core. (b) Under a magnetic field  $H_{c1} < H_{ext} < H_{c2}$ , a type II superconductor will let individual magnetic flux quanta penetrate its volume as tubes of normal state surrounded by supercurrents, called vortices. The vortices on the sample will appear as disks and will most likely arrange in a triangular lattice, called Abrikosov lattice, due to the repulsive interactions between neighboring vortices.

The first observation of the vortex lattice was obtained in 1967 by Essmann and Träuble [22] in a superconducting Pb sample, through a technique known as Bitter magnetic decoration. Small magnetic particles were spread over the sample and a low magnetic field was applied perpendicular to the surface. The particles concentrated then at the points where the field value was highest, i.e. over the vortex cores, revealing its spatial distribution [23]. As the magnetic penetration depth is large, vortices need to be very far apart to obtain images of isolated vortices using this technique. Thus, often, magnetic decoration is limited to low magnetic fields. Neutron scattering is also used to observe the magnetic pattern of the vortex lattice at all magnetic fields.

Using a STM, as we will show below, we can measure the spatial variation of the superconducting density of states. This is related to the much smaller coherence length  $\xi$ . Thus, we can use STM to view the vortex lattice at high magnetic fields [24].

## 1.2.2 CdGM states in vortex cores

Caroli, de Gennes and Matricon predicted in 1964 [25] that the spatially varying pair potential inside a vortex core can lead to the formation of localized Andreev bound states, which became known as Caroli-de Gennes-Matricon states, or CdGM states for short. The energy levels of CdGM states are quantized, with a level spacing of  $\delta \approx \Delta^2/E_F$ , with  $\Delta$  the superconducting gap and  $E_F$  the Fermi energy. Hess *et al.* found a peak in the density of states at the vortex cores of 2H-NbSe<sub>2</sub> [24, 26, 27], which he ascribed as due to many CdGM states at low energies. Subsequent theoretical work [28, 29] showed that CdGM states can indeed produce a peak in the density of states at the Fermi level. Detailed calculations [30, 29] showed that some features observed by Hess, such as the splitting of the peak and its spatial anisotropy, could be associated to the anisotropy of the superconducting properties of 2H-NbSe<sub>2</sub>. A comparison between results in 2H-NbS<sub>2</sub> and 2H-NbSe<sub>2</sub> showed that these anisotropic properties are related to the charge density wave of 2H-NbSe<sub>2</sub>, which is absent in 2H-NbS<sub>2</sub> [14].

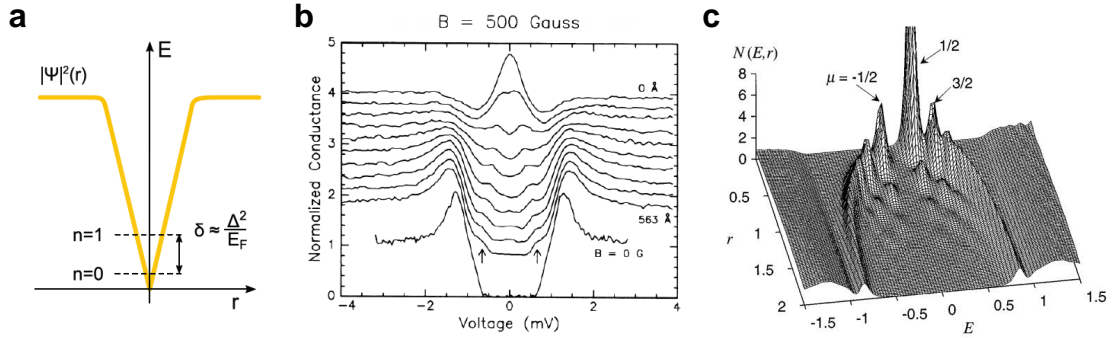


**Figure 1.9:** (a) Adapted from Ref. [31]. Schematic representation of the variation of the pair potential (yellow) and the energy level spacing of the CdGM states inside the core. (b) Extracted from Ref. [26]. Conductance curves from the center of the a vortex core (top) to the outside (bottom) in a 2H-NbSe<sub>2</sub> sample. (c) Extracted from Ref. [29]. Density of states as a function of the energy and the radius with respect to the center of a vortex core. Notice that the strong asymmetry of the density of states is not observed in the experiments. The calculations are made in the so-called quantum limit, where  $\delta \gg k_B T$ , which does not apply for 2H-NbSe<sub>2</sub>. In 2H-NbSe<sub>2</sub> instead, the accumulation of low energy CdGM states leads to the peak observed in (b) [32].

## 1.2.3 Vortex core size

The shape of the superconducting density of states around a vortex core depends on several aspects, such as the shape of the superconducting gap in reciprocal space, the normal state density of states and the distance to neighboring vortices. The latter very strongly changes with magnetic field. It was shown by Kogan and Zhelezina [33] that the shape of the superconducting density of states should considerably change

with the magnetic field. In particular, the slope of the Cooper pair wavefunction should decrease when decreasing the magnetic field. The slope of the Cooper pair wavefunction has been taken as a measure of the vortex core size. Thus, the vortex core size increases with decreasing magnetic field. According to Kogan and Zhelezina, this occurs as  $1/\sqrt{H}$  in clean superconductors up to the critical field  $H_{c2}$  (see Equation 1.19). Superconductors with a small mean free path (i.e. in the dirty limit) have a smeared density of states whose spatial shape is magnetic field independent [33].

$$\xi(H) = \sqrt{\frac{\Phi_0}{2\pi H}} \quad (1.19)$$

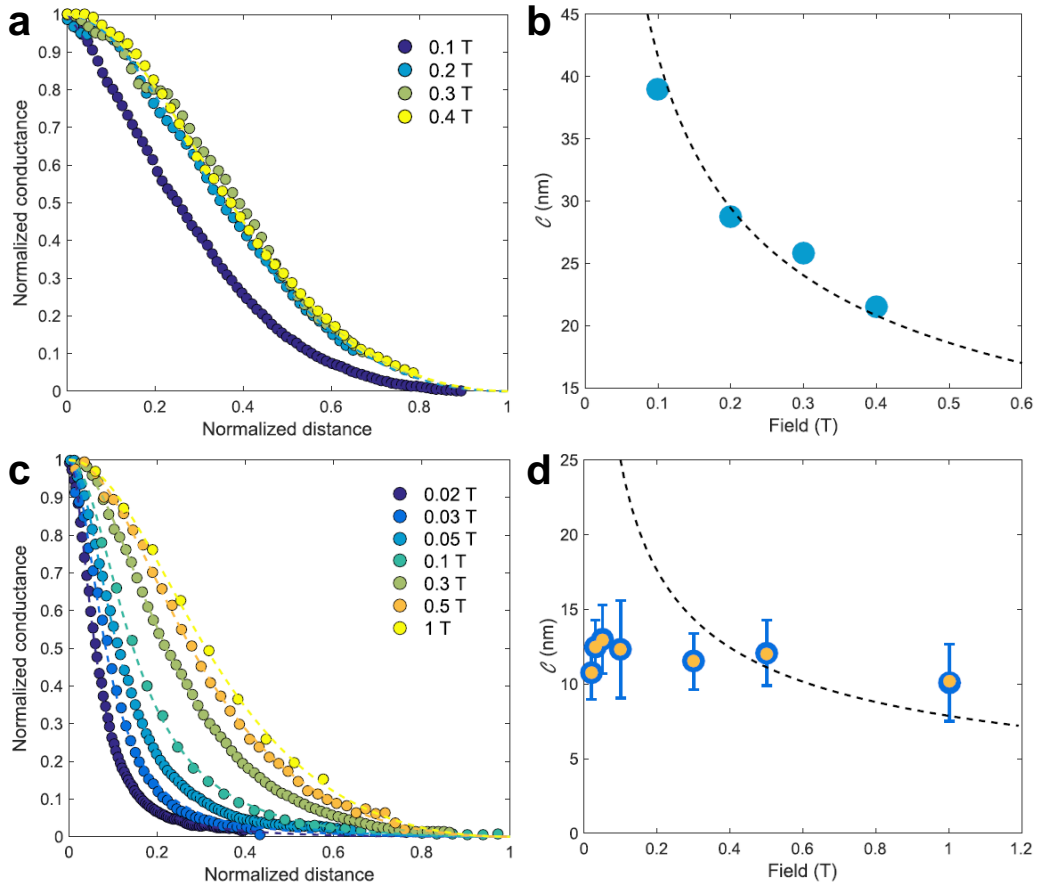


**Figure 1.10:** Adapted from Refs. [31, 34]. (a) Experimental data and model fit for the conductance in the vortex cores of  $\beta\text{-Bi}_2\text{Pd}$ . (b) Core size extracted from the fit as a function of the magnetic field. (c) and (d) present the experimental data, model fit (c) and core sizes (d) for the conductance in the vortex cores of  $2\text{H-NbSe}_{1.8}\text{S}_{0.2}$ . The dashed line in (b) and (d) is the expected  $1/\sqrt{H}$  dependence in the clean limit. We can see such a decrease in  $\beta\text{-Bi}_2\text{Pd}$  (b) but not in  $2\text{H-NbSe}_{1.8}\text{S}_{0.2}$ .

The model by Kogan is very useful to analyze images of the vortex lattice taken with the STM. The model is based on the de Gennes formula for the relation between

the density of states and the size of the superconducting gap:

$$\frac{N(r)}{N_0} = 1 - \frac{|\Delta(r)|^2}{\Delta_0^2} \quad (1.20)$$

where  $N_0$  is the normal state DOS and  $\Delta_0$  the maximum value of the superconducting gap at zero temperature. Regarding the spatial variation of the gap, the model follows the dependence described in Refs. [35] and [36]. According to it, the variation of the normalized conductance  $\sigma$  in a vortex core is:

$$\sigma(\rho, \eta) = 1 - \frac{\rho^2(1 + \eta^2)}{\rho^2 + \eta^2} \exp\left[\frac{\eta^2(1 - \rho^2)}{1 + \eta^2}\right] \quad (1.21)$$

where  $\rho = r/a$  is the normalized vortex radial distance and  $\eta = C/a$  is the normalized core size, with  $0 < (\rho, \eta) < 1$ . The normalization distance  $a$  is the vortex radius, defined as a circular approximation to the hexagonal Wigner-Seitz unit cell of the hexagonal vortex lattice such that

$$a = \sqrt{\frac{\Phi_0}{\pi H}} \approx 0.525 a_0^\Delta \quad (1.22)$$

This model has been extensively tested in different samples [34, 37, 38]. Fig. 1.10 (a,b) shows the application of this model to vortex cores in the clean limit in  $\beta$ -Bi<sub>2</sub>Pd and Fig. 1.10 (c,d) shows the dirty limit in 2H-NbSe<sub>1.8</sub>S<sub>0.2</sub>.

## 1.2.4 Exchange interaction

Matthias *et al.* [39, 40, 41] discovered that the  $T_c$  of a La sample dropped significantly when small amounts of magnetic Gd impurities were added. Beyond 1% Gd, superconductivity was completely suppressed and a ferromagnetic transition rised. As shown in Fig. 1.11(a), they associated the observed decrease in  $T_c$  to the exchange interaction between the magnetic Gd ions and the superconducting La. Abrikosov and Gor'kov studied the influence of magnetic impurities (and other pair breaking sources) in the superconducting density of states of disordered superconductors [42]. They found that the energy range with a zero density of states decreases with increasing pair breaking strength. They also found that there is a small parameter range in the pair breaking strength where the superconducting density of states becomes completely gapless [43, 44]. This small parameter range occurs very close to the full destruction of superconductivity by magnetic pair breaking.

Measurements in thin films of Pb and In show indeed that there is a range with a non-zero density of states at the Fermi level [42].

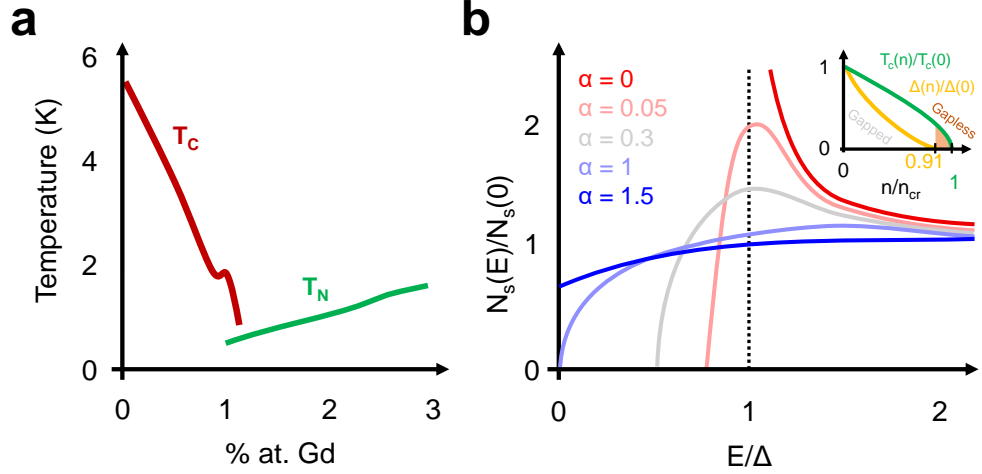


**Figure 1.11:** (a) Adapted from Ref. [41]. Superconducting (red) and ferromagnetic (green) transition temperatures in a La sample doped with magnetic impurities of Gd. Above 1% content in Gd, superconductivity in the alloy vanishes. (b) Adapted from Ref. [45]. Following Abrikosov and Gor’kov (AG) theory, we plot the density of states when increasing the pair breaking parameter  $\alpha$ . Note that the superconducting gap smears when increasing  $\alpha$  and disappears above  $\alpha=1$ . We show in the inset, also adapted from Ref. [45], the dependence of  $T_c$  and the superconducting gap  $\Delta$  with the impurity concentration  $n$ . We observe that beyond a certain value  $n_0 < n_{cr}$ , the superconducting gap vanishes yet  $T_c$  is nonzero, hence the mentioned gapless superconducting regime, here shadowed in orange.

### 1.2.5 YSR bound states

A few years after the works of Matthias [39, 40, 41], Yu, Shiba and Rusinov showed that an isolated magnetic impurity in a superconductor produces states, often inside the superconducting gap, in the vicinity of the impurity [46, 47, 48], namely the Yu-Shiba-Rusinov states, or YSR for short. This means that the exchange interaction between magnetic moments and Cooper pairs modifies considerably the superconducting state [49]. In the most simple treatment we consider a single parabolic band and  $s$ -wave superconductivity. We can write the energy at which the localized states appear inside the superconducting gap as:

$$\varepsilon = \Delta \cos(\delta^+ - \delta^-) \quad (1.23)$$

where  $\tan \delta^\pm = K\rho_0 \pm JS/2\rho_0$ , with  $\rho_0$  being the DOS at the Fermi level in the normal state [48],  $S$  the spin,  $J$  the exchange interaction and  $K$  the Coulomb potential. The peak in the density of states is often observed at positive and negative energies. The wavefunction has an oscillatory decay as a function of the position, given in 2D by:

$$\psi_\pm(r) = \frac{1}{\sqrt{N\pi k_F r}} \sin\left(k_F r - \frac{\pi}{4} + \delta^\pm\right) e^{-\Delta \frac{\sin(\delta^+ - \delta^-) r}{\hbar v_F}} \quad (1.24)$$

where  $\psi_{\pm}$  are respectively the electron and hole components of the YSR wave function  $\psi$ ,  $N$  is a normalization factor,  $k_F$  is the Fermi wave vector and  $v_F$  the Fermi velocity. This YSR wavefunction results in a peak in the in-gap superconducting density of states, whose size oscillates with position, as shown for example in Fig. 1.12 (c,d).

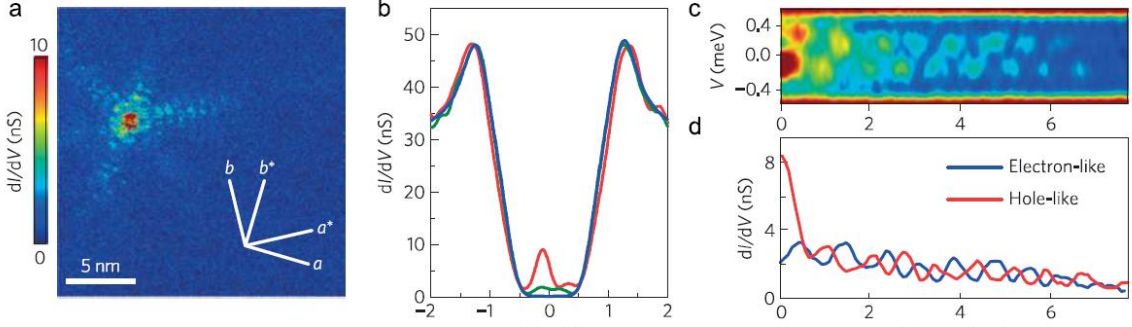


**Figure 1.12:** Adapted from Ref. [50]. Experimental results of spectroscopic measurements on 2H-NbSe<sub>2</sub> with Fe impurities (a). Magnetic impurities produce in-gap states (b) that oscillate between positive and negative energies (c,d) as expected from theory.

### 1.3 Iron based superconductors

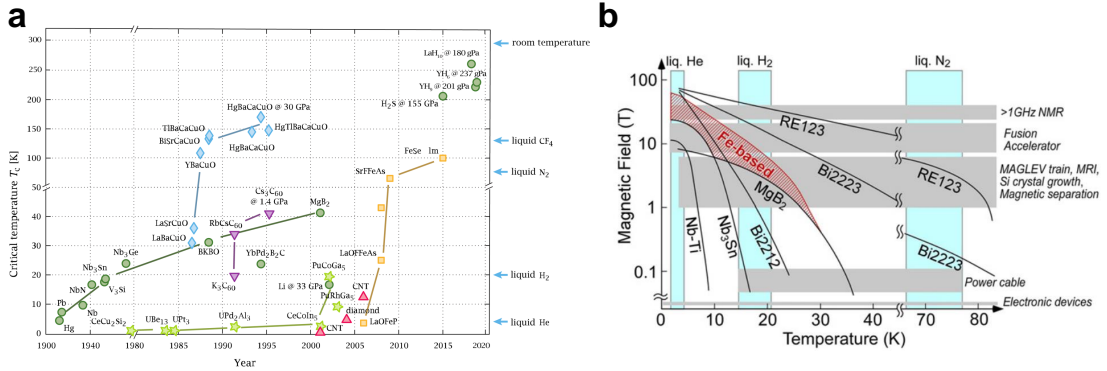


**Figure 1.13:** (a) Adapted from Ref. [51]. We show the highest critical temperature for each family of superconductors through the years. Conventional BCS superconductors are represented by green circles, heavy-fermions by green stars, carbon allotropes by red triangles, buckminster fullerenes by purple triangles, Fe-based pnictogens by orange squares and cuprates by blue diamonds. (b) Extrsacted from Ref. [52]. Upper critical field versus temperature for some industrially-used families of materials. The temperature range for different cryogenic liquids is marked with blue rectangles and some use cases for magnetic fields of different intensities are shadowed in gray. As we can see, iron based superconductors attain critical fields of tens of Tesla at temperatures below 20 K, while being remarkably more malleable and ductile than other cuprate alternatives.

After the discovery of cuprates in 1986 [53], which realised superconductivity above liquid nitrogen temperatures, a relevant breakthrough was the discovery of the iron pnictide superconductors in 2008 by Kamihara *et al.* [54].

Before the discovery of superconductivity at  $T_c=26$  K in  $\text{LaFeAsO}_{1-x}\text{F}_x$  (see Fig. 1.13(a)), Kamihara’s group had been focusing in iron based superconductors the previous years, finding superconductivity at 6 K in  $\text{LaFePO}$  in 2006 [55] and at 2.4 K in  $\text{LaNiAsO}$  in 2007 [56]. Interestingly, superconductivity appeared with a high  $T_c$  in systems containing iron, which was thought to be detrimental to superconductivity due to its magnetic properties. Iron based materials belong to the family of unconventional superconductors, in which it is thought that Cooper pairing is not due to the exchange of phonons, but due to magnetic or electronic interactions. From a more industrial point of view, iron based superconductors have extremely high critical fields and are malleable metals, much better suited for wire and coil fabrication than brittle ceramic cuprates.

In the following years, many different families of iron based superconductors were discovered. They are usually referred to with the subscripts in their chemical formula: 11 ( $\text{FeSe}$ ), 111 ( $\text{LiFeAs}$ ), 1111 ( $\text{LaFeAsO}$ ), 122 ( $\text{SrFe}_2\text{As}_2$ ), 1144 ( $\text{CaKFe}_4\text{As}_4$ ), etc. and they all share common structural features like a tetragonal unit cell and checkerboard Fe-Pn layers, where Pn is a light pnictogen element (N, P, As) or, less commonly, a chalcogen (S, Se, Te). We depict the main structural characteristics of iron based superconductors in Fig. 1.14. In this Ph.D. thesis, we will mainly focus on the 122-type, as the P-doped  $\text{BaFe}_2\text{As}_2$  has this structure. I have been also actively working on the new 1144 family [57, 58, 37, 13], participating in experiments and growing samples of that system.

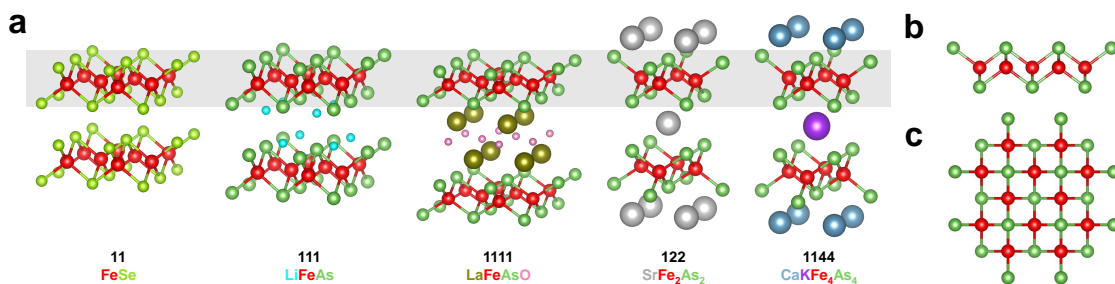


**Figure 1.14:** Inspired by Ref. [59]. In (a) we show some examples of the most representative families of iron based superconductors. Note that they all share common features like a Fe and pnictogen layer, highlighted here in grey. We also show a lateral (b) and top view (c) of this tetragonal checkerboard layer for better visualization.

### 1.3.1 General electronic properties of iron based superconductors

The generic phase diagram of an iron based superconductor is depicted in Fig. 1.15(a). A non-superconducting parent compound has a transition (usually magnetic, structural, nematic or any combination of them) at low temperatures into an ordered phase. This transition is suppressed by means of a non-thermal

control parameter like magnetic field, pressure or most commonly, doping. Then a superconducting dome develops and reaches maximum  $T_c$  close to the point where this ordered phase goes to zero, suggesting a competing character and a possible superconductivity enhancement thanks to the low temperature fluctuations of the ordered phase. The microscopic coexistence of phases is non-trivial and depends on the precise details of the chemical system, and exotic behavior like non-Fermi liquid properties can arise close to maximum  $T_c$ . We will expand this further in subsection 1.3.2.

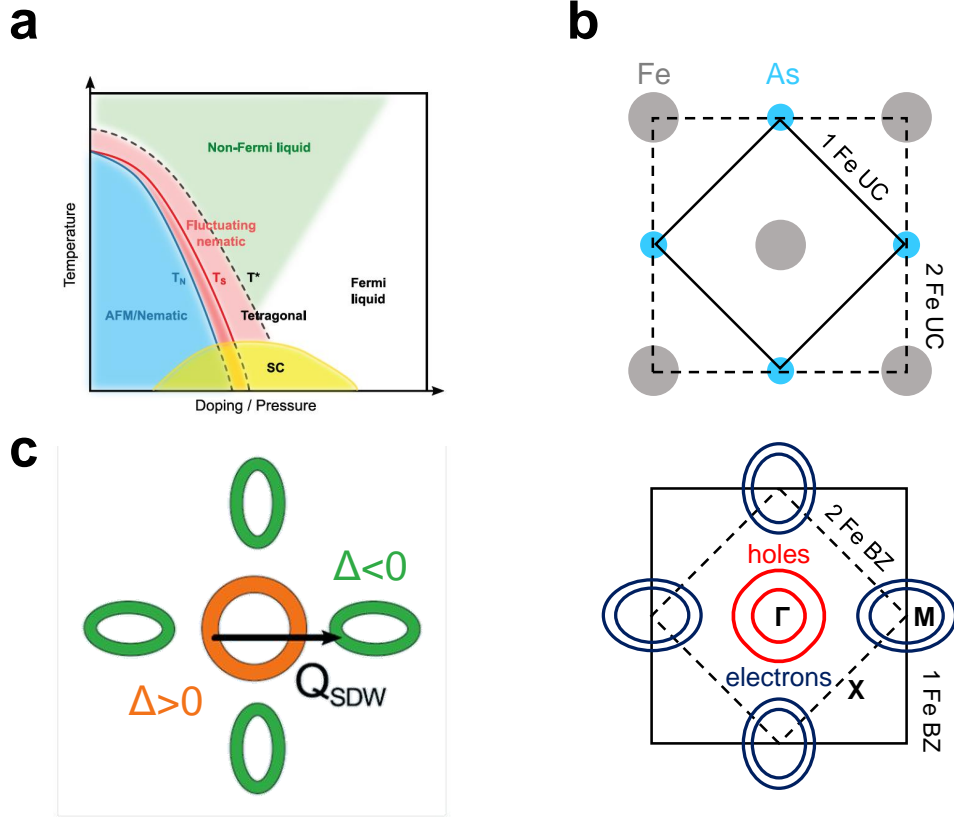


**Figure 1.15:** (a) Extracted from Ref. [31]. Generic temperature vs. doping/pressure phase diagram for most iron based superconductors. The non-thermal parameter suppresses the magnetic/structural transition and a superconducting dome develops with maximum  $T_c$  close to the extrapolation of the ordered transition to zero. Usually non-Fermi liquid behavior is found around the maximum  $T_c$ . (b) Generic unit cells in the FeAs layer (top panel), with the typical Fermi surface for most iron based superconductors (bottom panel): 2-3 cylindrical hole bands around  $\Gamma$  and 1-2 electron bands around M. Note that the dashed square indicates the 2 Fe atom unit cell, which translates into the reduced (also known as magnetic) Brillouin zone, also highlighted with a dashed square. (c) Adapted from Ref. [60].  $s^{\pm}$  pairing mechanism, in which the gap changes sign between the hole and electron pockets by means of a magnetic fluctuation vector, here named  $Q_{SDW}$ .

On the other hand, most iron based superconductors also share very common features in their Fermi surfaces. The generic Fermi surface of an iron based

superconductor is depicted in Fig. 1.15(b). Usually there are two or three cylindrical hole bands at the center of the Brillouin zone, and one or two cylindrical electron bands at the corners. The 2D character varies widely between compounds and dopings but most of the time the Fermi surfaces can be considered effectively bidimensional. While the conduction electrons in cuprates can be restricted to a single  $3d$  orbital at the Cu site, iron based superconductors have six electrons occupying the nearly degenerate  $3d$  Fe orbitals, indicating that the system is intrinsically multiorbital and therefore that the interorbital Coulomb interaction plays an essential role [61]. The superconducting gap can (and usually does) have different values in different pockets and parts of the Fermi surface (Fig. 1.15(c)), and sometimes it even has point or line nodes where its amplitude is zero, giving rise to exotic anisotropies and nodal superconductivity.

Regarding the pairing interaction and symmetry, iron based superconductors are out of the electron-phonon framework and thus are considered unconventional superconductors. In this lack of electron-phonon coupling, in order to satisfy the self consistent gap equation with a repulsive potential, the order parameter (the superconducting gap) must change sign between different parts of the Fermi surface. Several gap symmetries and pairings have been proposed in order to account for this change in sign, yet the most convincing and accepted today is the  $s^\pm$  [62], in which the gap changes sign between the electron and hole pockets and superconductivity is mediated through a magnetic fluctuation vector connecting electron and hole pockets (see Fig. 1.15(c)).

### 1.3.2 Quantum criticality in iron based superconductors

A quantum critical phase transition takes place at absolute zero temperature between an ordered and a disordered state. It is not driven by thermal fluctuations like regular thermodynamic phase transitions but by quantum fluctuations associated with Heisenberg's uncertainty principle. Such transitions can be triggered by the variation of a number of non-thermal parameters like pressure, applied magnetic field or chemical doping [63, 64]. As a quantum phase transition only occurs at zero temperature, it is usually depicted as a quantum critical point at ( $f = f_c, T = 0$ ) in a  $T$  vs  $f$  phase diagram, being  $f$  the non-thermal control parameter (see Fig. 1.16(a)). Usually they also involve a characteristic funnel shaped quantum critical region above them where quantum fluctuations extend to a finite temperature and give rise to exotic non-Fermi liquid electronic behavior.

As we have introduced in subsection 1.3.1, most unconventional superconductors (and specifically iron based superconductors) share a common generalized phase diagram in which the parent compound presents a magnetically ordered state, usually coupled to a structural transition, that is suppressed by means of increasing a certain parameter, usually doping, while a superconducting dome develops [60]. This is schematically represented in Fig. 1.16(b) which is a simplification of Fig. 1.15(a). The maximum  $T_c$  is usually attained at the point where the extrapolation of the magnetic transition drops to zero. Whether or not the transition actually drops to a quantum critical point or is instead somehow avoided by the surge of the

superconductivity itself depends on the specific material and can be difficult to prove, but it is certainly a promising setup to probe the fundamental causes behind high  $T_c$  superconductivity.

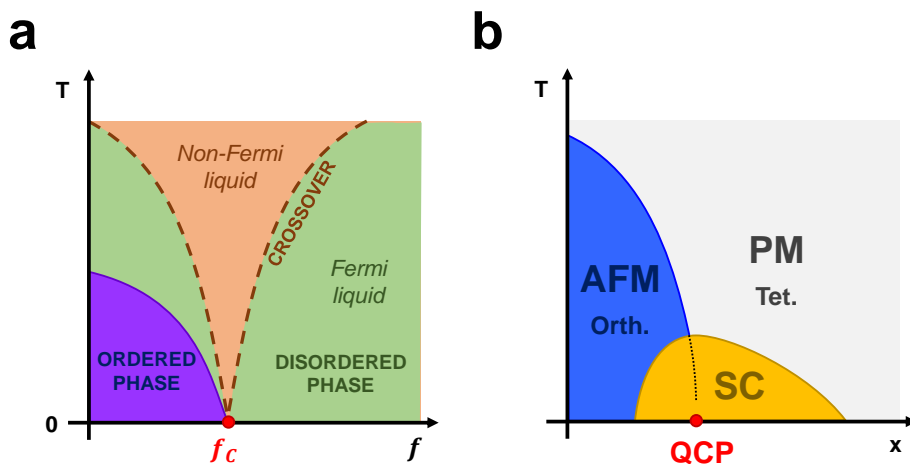


**Figure 1.16:** (a) General phase diagram around a quantum critical point. An ordered phase is suppressed by means of a non-thermal parameter  $f$  into a disordered phase that behaves as a Fermi liquid. At zero temperature, this phase transition can still occur due to quantum fluctuations at a certain critical point  $f_c$ , which is known as a quantum critical point. Above it, at finite temperatures we usually find a funnel shaped region with non-Fermi liquid properties. (b) Generalized phase diagram of iron based superconductors. A magnetic phase can be suppressed by a control parameter, in this case doping  $x$ , giving rise to a superconducting dome. A quantum critical point can develop at the point where the magnetic transition goes to zero, where also usually the maximum  $T_c$  is attained.

## 1.4 The Josephson effect

### 1.4.1 The Josephson equations

The Josephson effect, as we will see later on, can be accessed and measured using a STM. However, it is much less studied than the electronic density of states. As I will show in this Ph.D. thesis, we have uncovered a completely new regime for the Josephson behavior, which should be very useful to study unconventional superconductors using the STM. It is thus good at this point to remember a few basic aspects of the physics of Josephson junctions.

In 1962, B. D. Josephson predicted the existence of tunnel currents carried by Cooper pairs between two superconducting electrodes separated by a thin insulating barrier due to the overlapping of the macroscopic wave functions in the barrier region [65]. Such a configuration became known as "weak links" or simply Josephson

junctions. The two basic equations that describe the Josephson junctions are:

$$I_J = I_c \sin(\varphi) \quad (1.25)$$

$$\frac{d\varphi}{dt} = \frac{2e}{\hbar} V = \frac{2\pi}{\Phi_0} V \quad (1.26)$$

where  $\varphi = \varphi_1 - \varphi_2$  is the wave function phase difference between the superconductors,  $e$  is the electron charge,  $\hbar$  is the reduced Planck constant,  $\Phi_0$  is the magnetic flux quantum and  $I_c$  is the maximum critical current, which in general depends on the magnetic field or the temperature. We can see from the equations that there exists a finite current  $I_J$  at  $V = 0$  whose value depends on the phase difference between the electrodes. We can see a characteristic I-V curve of a tunnel Josephson junction in [Fig. 1.17](#), similar to those we obtain in our experiments.

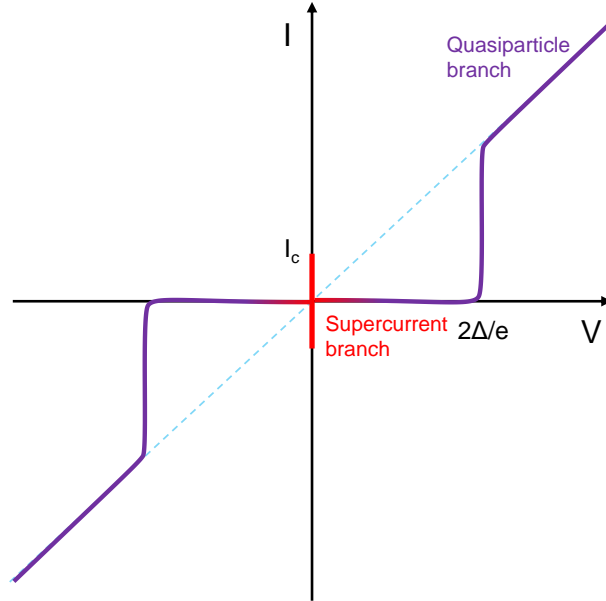


**Figure 1.17:** Typical shape of the I-V curves in the conditions of our experiment.

If we apply a finite voltage  $V \neq 0$  to the junction, then from [Equation 1.26](#) we obtain that the phase difference varies in time and therefore the Josephson current  $I_J$  oscillates in time following:

$$I_J(t) = I_c \sin(\varphi_0 + \omega_0 V t) \quad (1.27)$$

with  $\omega_0 = \frac{2\pi}{\Phi_0}$  the Josephson plasma frequency, which is of the order of GHz to THz when the voltage ranges between  $\mu\text{V}$  and  $\text{mV}$ .

## 1.4.2 The RCSJ model

Although the above mentioned microscopic formalism is useful to describe the simplest tunnel cases [66, 67], it fails to account for the interaction of the quantum phase with the immediate electromagnetic environment. To this end we will consider the resistively and capacitively shunted junction (RCSJ) model, first introduced by McCumber and Stewart in 1968 [68, 69]. They study the behavior of the Josephson junction as the combination of simple linear circuit elements, in this case a resistor and a capacitance shunting a tunnel junction. The equivalent circuit would then be described by the following equation.

$$I_J = \frac{\Phi_0}{2\pi} C \frac{\partial^2 \varphi}{\partial t^2} + \frac{\Phi_0}{2\pi} \frac{1}{R} \frac{\partial \varphi}{\partial t} + I_c \sin(\varphi) \quad (1.28)$$

Equation 1.28 might look familiar since it is a ubiquitous differential equation of motion equivalent of that of a damped and driven pendulum. In this case, the capacitance term acts as the inertial moment term, the resistor term acts as the drag term, the voltage is equivalent to the angular velocity and the applied current acts as the driving force. A common way to visualize it is as a particle moving through a tilted washboard potential, which is schematically represented in Fig. 1.18

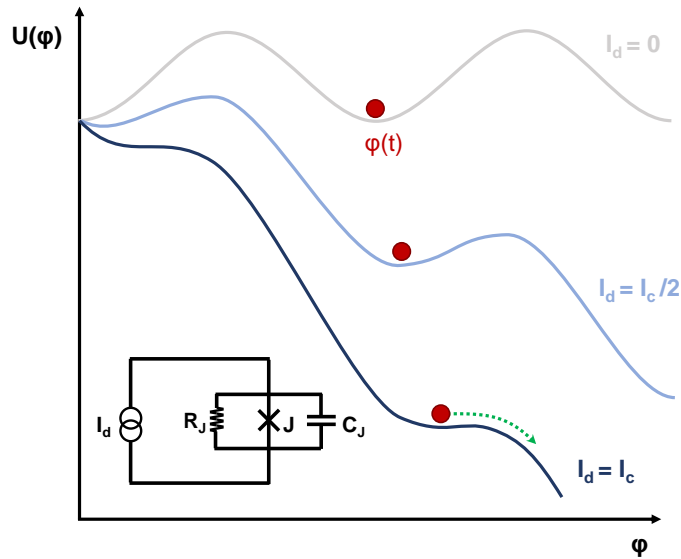


**Figure 1.18:** Adapted from Ref. [70]. Washboard potential of an ideal tunnel Josephson junction at zero temperature. Note that it is  $2\pi$  periodic as any additional  $2\pi$  phase difference must be physically identical. When  $I_d < I_c$ , the phase particle is trapped in one of the wells. As the drive current increases, the barrier height decreases until at the critical current is achieved. At this point, the phase runs since the potential no longer has minima and and the resistive state is recovered (quasiparticle branch in Fig. 1.17)

By using the dimensionless reduced time  $\tau = \omega_0 t$ , we can rewrite Equation 1.28

as:

$$i = \frac{\partial^2 \varphi}{\partial \tau^2} + \beta \frac{\partial \varphi}{\partial \tau} + \sin(\varphi) \quad (1.29)$$

with  $i = \frac{I_d}{I_c}$  the reduced bias current,  $I_d$  the driving current,  $I_c$  the critical current and  $\beta = \frac{2\pi}{\Phi_0} I_c R^2 C$  the Stewart-McCumber parameter. By introducing the new variables  $x_1 = \varphi$  and  $x_2 = \frac{\partial \varphi}{\partial t} \propto V$ , we obtain the following differential equation that summarizes the behavior of the junction:

$$\frac{dx_2}{d\tau} = -\frac{1}{\beta} [\sin(x_1) + x_2 + i] \quad (1.30)$$

Note that when the voltage is zero, i.e.  $x_2 = 0$ , we recover the first Josephson equation for the DC Josephson effect  $i = \sin(x_1)$ . The reduced current  $i$  is always below 1, as the current is always below the critical current  $I_c$ . Above the critical current we find though a finite time dependent voltage ( $x_2 \neq 0$ ) with oscillations at a time constant given by  $\tau$ .

## 1.5 Transition metal dichalcogenides

The transition metal dichalcogenides are probably one of the most thoroughly studied families of materials using STM. Studying superconductivity in these compounds, we have uncovered a number of interesting features of magnetic impurities in superconductors. To address this problem, it is useful to make a brief introduction to the specific aspects of the physics of transition metal dichalcogenides. These compounds of the form  $MX_2$ , where  $M$  is a transition metal and  $X$  is a chalcogen element (S, Se, Te), are relatively easy to grow with high chemical purity in large single crystals and to exfoliate in thin atomically flat flakes. They display a very wide and interesting set of optical, structural, mechanical and electronic properties [71], arising from their mostly bidimensional and highly anisotropic Fermi surfaces. In this Ph.D. thesis we have mainly focused in one of the most well studied representatives of the transition metal dichalcogenides, 2H-NbSe<sub>2</sub>, and the doping series arising from S substitution in the Se atomic place.

### 1.5.1 The 2H-NbSe<sub>2-x</sub>S<sub>x</sub> system

The parent compound 2H-NbSe<sub>2</sub> is a superconductor below 7.2 K and presents a characteristic charge density wave (CDW) ordering below 33.5 K [72, 73], where every three atoms the local density of states (from now on, LDOS) is enhanced along the crystalline directions (Fig. 1.19(a)). It has very pressure-sensitive electronic and superconducting properties [74, 75] and it's the first compound in which Hess *et al.* observed the Abrikosov vortex lattice with STM in 1989 [24]. Further spectroscopic images confirmed a strong in-plane sixfold anisotropy in the electronic properties [26, 29, 76] that causes vortices to have a characteristic sixfold star shape (Fig. 1.19(b)).

At the other end of the doping series,  $2\text{H-NbS}_2$  is also a superconductor below 6 K [77, 78]. However, the CDW transition seems to be absent and the in-plane electronic properties are much more isotropic, with perfectly round vortices [14] (Fig. 1.19(c,d)).

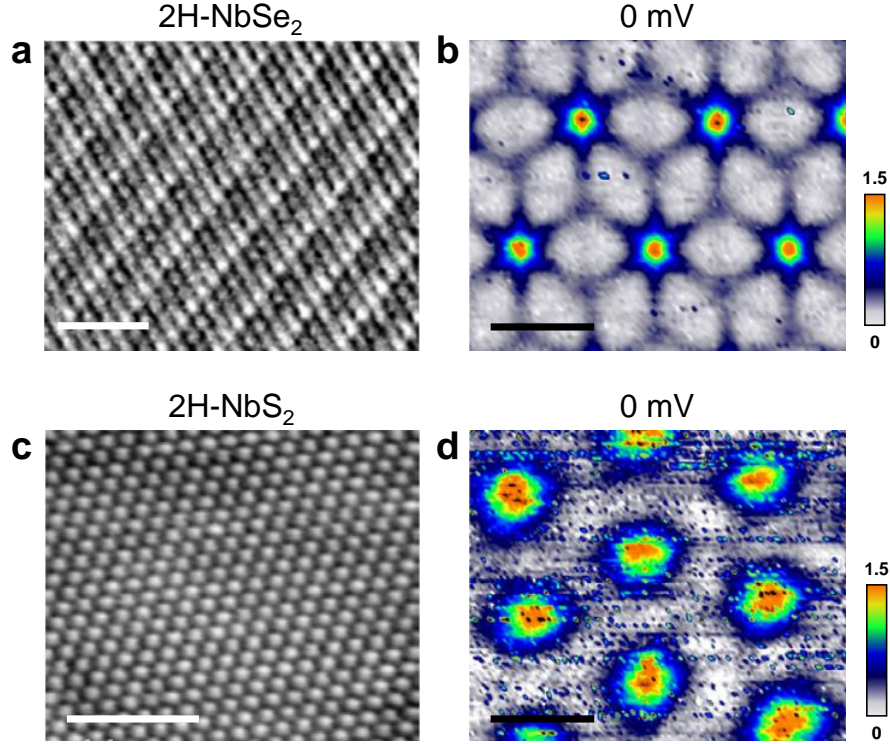


**Figure 1.19:** (a) STM topography at 0.1 K and zero field of a  $2\text{H-NbSe}_2$  sample, where we can appreciate the enhancement in brightness of one every three atoms due to the charge density wave. In (b) we show the zero bias conductance map at 0.15 T of a large flat surface in  $2\text{H-NbSe}_2$ , where we can observe the characteristic sixfold star shaped vortices. (c) STM topography of a  $2\text{H-NbS}_2$  sample taken in similar conditions as in (a). We observe the lack of long range ordering whatsoever. In (d) we show again the zero bias conductance map in similar conditions to (b), and we can appreciate that vortex cores are now completely round. White scale bars are 2 nm long, and black scale bars are 100 nm long. All images are adapted from Refs. [14, 79].

Both  $2\text{H-NbSe}_2$  and  $2\text{H-NbS}_2$  share the same crystal structure  $P6_3/mmc$  (space group 194), depicted in Fig. 1.20. It consists of a hexagonal arrangement of Nb atoms sandwiched between two hexagonal layers of Se/S atoms covalently bonded. These slabs then are stacked via weak Van der Waals forces in a variety of arrangements. The measurements shown in this Ph.D. thesis were done in  $2\text{H-NbSe}_2$  and  $2\text{H-NbSe}_{1.8}\text{S}_{0.2}$  samples with 2H-type stacking, in which every Nb atom falls on top of each other.

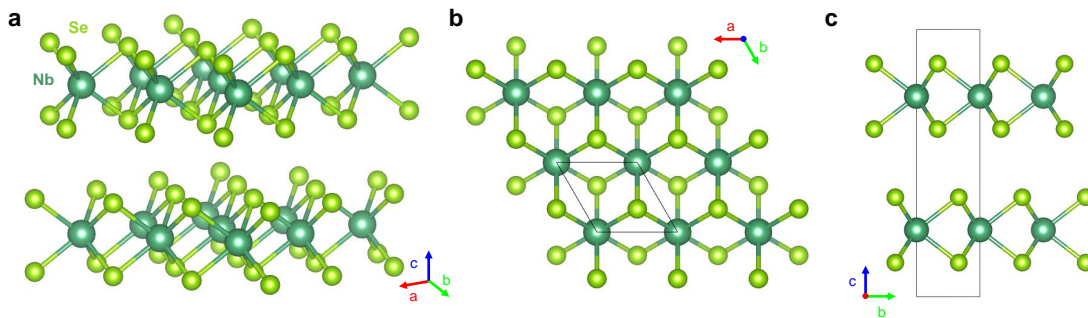


**Figure 1.20:** Crystal structure of 2H-NbSe<sub>2</sub> and of 2H-NbS<sub>2</sub> (a) and its top view (b) and side view (c). The unit cell is marked with a solid black line. Nb atoms are shown as dark green spheres and Se or S atoms as light green spheres.

## 1.6 Scope of this work

Competing or antagonistic phenomena are generally a fruitful ground for new discoveries. Advances in the development of microscopes allow directly visualizing the phenomena as a function of the position in real space. This contrasts usual techniques where the system is viewed as a whole. Using a microscope we can now address if the antagonism produces droplets of phases separated from each other, in which each phenomenon is more or less unaffected, or a homogeneous state of anomalous electronic properties. In both cases, microscopy allows to visualize the radically new behavior of antagonistic phenomena in a particularly enlightening way.

Superconductivity and magnetism are considered as antagonistic phenomena since the establishment of the deleterious role of the magnetic field on a superconductor by Heike Kamerlingh Onnes in the start of the 20th century. Modern superconducting compounds, like iron pnictide or cuprate materials, are capable of holding magnetic fields and critical currents many orders of magnitude larger than the initial simple systems composed of a single element as Hg, Pb or Al. In the modern compounds, superconductivity appears in close proximity to magnetic phases. Furthermore, we can introduce and study isolated magnetic impurities in a concentration which does not affect macroscopic behavior. This new situation, combined with advanced microscopes that allow studying directly the superconducting properties with atomic precision, is the starting point of this Ph.D. thesis.

Superconducting materials can undergo transitions as a function of several control parameters, apart from that of superconductivity with temperature. Pressure, strain, impurity doping, elemental substitution or applied magnetic field can trigger new ordered phases that either coexist or compete with superconductivity. These continuous transitions can happen even at zero temperature: the driving mechanism is not the thermal fluctuations but the quantum fluctuations in the system. We chose to study an iron pnictide system, BaFe<sub>2</sub>As<sub>2</sub>, where such quantum criticality is attained by the isovalent doping of As by P. As the doping increases, the magnetic order vanishes and superconductivity enhances. At a certain P concentration of 0.3, the system reaches its maximum  $T_c$  precisely where the magnetic order seems to

vanish at zero temperature. A close look at the microscopic electronic properties at very low temperatures in close vicinity to the quantum critical point sheds some relevant clues about the role of quantum fluctuations in the consolidation of superconductivity.

The ability to visualize the electronic properties at the atomic scale gives access to a far wider variety of localized phenomena that would simply be averaged out in the bulk measurements. Crystalline defects, impurity atoms or superconducting vortices have a natural length scale of around few to few hundred nanometers and usually cause a local disruption in the superconducting properties of the material. The study of the interplay of such features with the surrounding electronic environment is a key aspect to understand the microscopic properties of the superconducting state and to progress in the nanofabrication of complex materials. To this end, we decided to focus on a well-known layered 2D chalcogenide like 2H-NbSe<sub>2</sub> and its S-doped counterpart 2H-NbSe<sub>1.8</sub>S<sub>0.2</sub> with dilute Fe magnetic impurities, studying the interplay between localized states at vortex cores and magnetic impurities as well as the effect that the impurities had on the overall electronic properties.

Recent results in new ordered superconducting states [80] and superconducting gap visualization [81] show that there is still a pressing need for the development and implementation of new or more precise STM-based techniques. For instance, Scanning Josephson Spectroscopy provides information about the Cooper pair density and the gap sign, yet its application is still very limited and there are ill-understood features. In this work we report the discovery of a new AC Josephson coupling between the junction and the measurement circuit that enhances the Josephson signal far beyond the critical current and provides the ground for more precise or time-sensitive future Scanning Josephson Spectroscopy experiments.

# 2 | Experimental Methods

Low temperatures and a high spatial and energy resolution are essential to observe and study the local electronic properties and correlations of a macroscopic quantum state like superconductivity. In the first sections of this chapter I will describe the methods and experimental setup that I have used during my Ph.D. research at LBTUAM, consisting of a dilution refrigerator and a home-built STM, which was manufactured and assembled at SEGAINVEX [82]. After explaining the basic elements and the principle of operation, I will also detail the improvements that I introduced to the setup.

A good experimental setup is, however, incomplete without a high quality sample. Many superconducting materials present some degree of anisotropy that can only be preserved and measured in single crystals. In the second part of the chapter I will explain the crystal growth techniques that I practised during my international research stay at Ames Laboratory (Iowa, USA). That knowledge was then applied to our own crystal growth facilities and led to several recent publications [83, 84, 85].

Lastly, a nice sample quality in a good experimental setup is incomplete without a proper data analysis of the results. I will also comment briefly about the new software developed by members of the team and my contributions to it. This new Matlab based software turned out to be instrumental for our group to be able to handle large files and achieve a sufficient capability to make images that show clearly the underlying physics.

## 2.1 The dilution refrigerator

The wet dilution refrigerator is a cooling device particularly interesting to the low temperature STM community, due to two key features. First, it is able to produce continuously temperatures in the millikelvin range. And second, it is devoid of the vibrations produced by dry cryogenic devices, such as pulse tubes or other cryocoolers.

### 2.1.1 Principle of operation

The principle of operation of the dilution refrigerator is based on the quantum properties of the mixture of  $^3\text{He}$  and  $^4\text{He}$  and it was first proposed by Heinz London in 1951 [86, 87]. As we can see in Fig. 2.1, the binary phase diagram of  $^3\text{He}$  and  $^4\text{He}$  consists of three main regions. At high temperatures the  $\lambda$ -line

separates the normal fluid phase (white, right) from the superfluid phase (blue, left). When the coexistence curve is hit, however, a forbidden region develops (yellow, bottom) in which the mixture is separated in two distinct phases with different  $^3\text{He}$  concentrations: a dilute and a concentrated one. Since the dilute phase is richer in  $^4\text{He}$ , the concentrated phase floats on top of it due to its lower density.

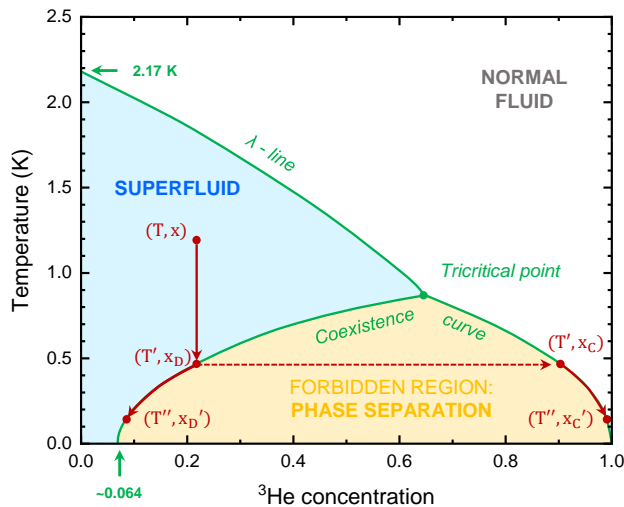


**Figure 2.1:** Phase diagram of  $^3\text{He}$ – $^4\text{He}$  mixture. The  $\lambda$ -line separates the normal fluid from the superfluid. The tricritical point ( $T = 0.86$  K), establishes the temperature where the liquid separates into two immiscible phases, the concentrated phase being almost pure  $^3\text{He}$  (right hand side of the diagram) and the dilute one, rich in  $^4\text{He}$  (left side).

The dilution refrigerator consists of a set of pumps, tubes and chambers that can cause the phase separation of the  $^3\text{He}$ – $^4\text{He}$  mixture and exploit its cooling power in a continuous operation. In Fig. 2.3 we show a comprehensive diagram of the whole cryogenic system, side-to-side with an actual photo of the dilution stage in which the different parts are indicated. The experiment needs to cool down to 4.2 K by means of an outer liquid  $^4\text{He}$  bath before the process starts. The  $^3\text{He}$ – $^4\text{He}$  mixture composition in our case sits at around 15%  $^3\text{He}$ .

Let us consider a point  $(T, x_C)$  in the phase diagram at a certain temperature  $T$  and  $^3\text{He}$  concentration  $x$ . By reducing the temperature at constant composition, one will eventually hit the coexistence line and attain the phase separation at  $T'$ , where the composition will split between the concentrated  $(T', x_C)$  and the dilute  $(T', x_D)$  phases. From this point, further reducing the temperature implies that the concentrated phase gets more concentrated  $(T'', x_C)$  and the dilute phase, even more dilute  $(T'', x_D)$ . Below 0.1 K, the  $^3\text{He}$  concentration is practically 100% in the concentrated phase, and ranges between 7% and 6.4% in the dilute one [88]. The fact that this lowest dilute  $^3\text{He}$  concentration is finite is relevant since it avoids the exponential decay of the cooling power below 300 mK [89] characteristic of other cooling systems like the  $^3\text{He}$  evaporation (see Fig. 2.2).

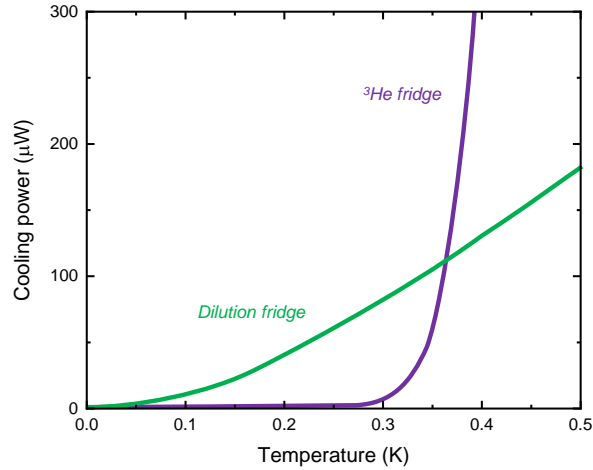


**Figure 2.2:** Cooling power of the dilution refrigerator compared to a classic  $^3\text{He}$  evaporation system. Graph adapted from Ref. [88]

The cooling process consists of a series of steps: first, the mixture is at ambient temperature and gets injected into the condenser, where it slowly cools down to  $\sim 1.5$  K thanks to its thermal contact with the 1K pot, which is cooled by the continuous extraction and evaporation of  $^4\text{He}$  from the bath. Once the mixture is liquid it continues going down through the heat exchangers, where it further cools down below the coexistence line. The phase separation interface occurs inside the mixing chamber, which is the coldest stage in the system at around 10 mK [90]. The mixture is then pumped through the heat exchangers up to the liquid-gas interface at the still, which sits at around 700 mK. Notice that due to the difference in vapor pressures between  $^3\text{He}$  and  $^4\text{He}$  at this temperature, the main part of the evaporated gas is pure  $^3\text{He}$ . Hence, the  $^3\text{He}$  concentration is constantly reduced in the still, generating an osmotic pressure gradient between the still and the mixing chamber that continuously drives  $^3\text{He}$  atoms from the concentrated phase into the dilute phase and up to the still, cooling the downflowing mixture at the heat exchangers on its way up. Finally, the  $^3\text{He}$  gas is pumped up back into the condenser after some purification with activated carbon filters inside a liquid  $\text{N}_2$  trap, and the process starts over. The initial  $^3\text{He}$  concentration and the volume of the mixture must be precisely selected for the phase separation to occur at the mixing chamber and have the liquid-gas interface at the still.

The STM stage is thermally attached to the mixing chamber. The needed wiring is soldered from the connectors through vacuum feedthroughs and thermalised in two intermediate stages. Mechanical vibrations, which could also negatively impact on the quality of the results, are minimized thanks to two key aspects: first, the pumps are physically isolated from the experiment in a different room and the tubes go through a sandbox before getting to the experiment. Second, the cryostat system is suspended with strings from the ceiling to decouple the low-frequency building vibrations from the high-frequency resonances of the stiff STM body. The cryostat is also equipped with a 9 T superconducting coil that lies at the bottom of the  $^4\text{He}$  bath.

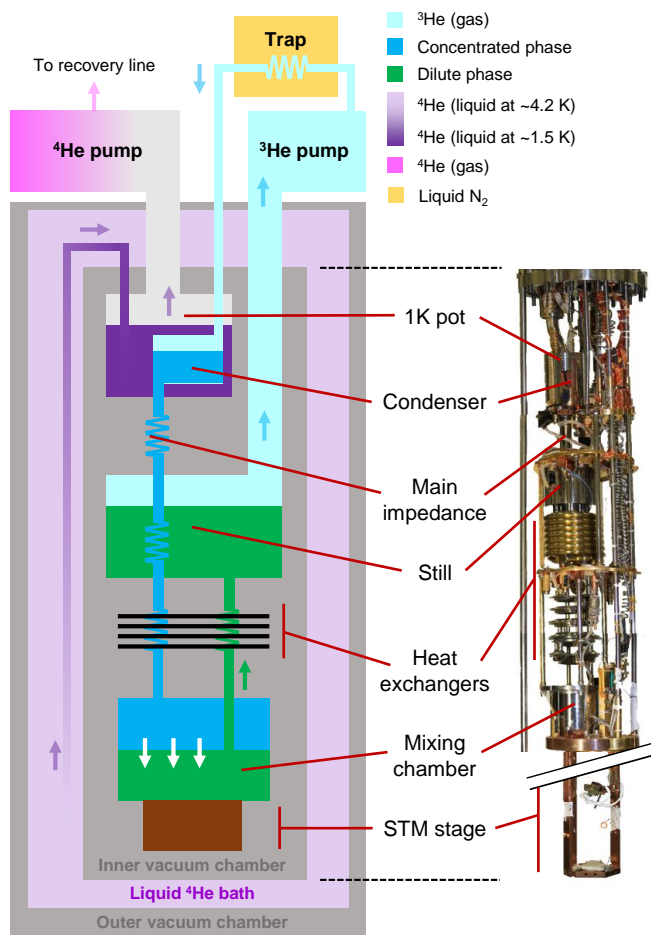


**Figure 2.3:** Diagram of the cooling system (left) and actual photo of the dilution stage, in which the different stages are indicated (right).

### 2.1.2 Improvements to the setup

The setup I used was installed and used before me [91, 34, 37]. However, there were a number of issues that I needed to address to be able to make the measurements shown in this Ph.D. thesis.

The first set of improvements were aimed at reducing the base temperature of the setup, which over the years had been increasing up to 800 mK. This was enough for high  $T_c$  superconductors but definitely not ideal for the purpose of this Ph.D. thesis. The first guess was that our  $^3\text{He}$ - $^4\text{He}$  mixture had been losing  $^3\text{He}$  and now was too poor to attain the phase separation inside the mixing chamber. We installed a  $^3\text{He}$  flow meter through the injection line, but the readings confirmed that the  $^3\text{He}$  flow was correct. Then we considered a leak in the inner vacuum chamber. We polished the indium joint, depicted in Fig. 2.5, to remove any mark or scar and successfully removed the leak, being able to cool down to 150 mK.

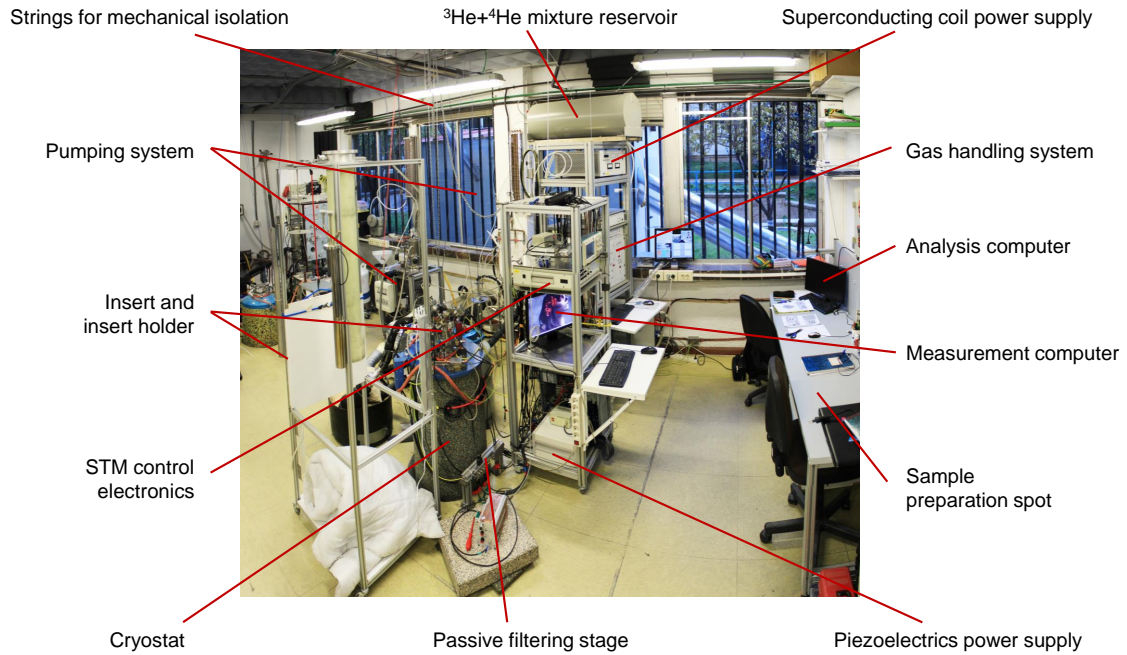


**Figure 2.4:** Photo of the complete experimental setup, including the cryostat and insert, the pumping and cooling systems, the acquisition and control electronics, the sample preparation table and the image analysis computer.

The second main concern to address was the mechanical stability and reliability of the STM, which was good enough for few hours long measurements but was unable to stay over the same spot of the surface for several days or weeks, or in between  $^4\text{He}$  transfer processes. This limited the amount of results and the scope of the experiment. The way to resolve this problem came from different directions: first, the  $^3\text{He}$  pumping line was passed through a home-built sandbox separate from the injection tube and the 1K pot pumping tube. This reduced substantially the mechanical vibrations transmitted to the cryostat through the tube when the dilution was operating. Second, the interstitial space in between the upper heat shields of the insert was filled and wrapped with EVA foam (see Fig. 2.5). This forces the passage of  $^4\text{He}$  gas close to the inner walls of the cryostat. The gas then more efficiently cools the shield in the outer vacuum of the cryostat, reducing the liquid He consumption and increasing the hold time. The third big improvement was the installation of theater curtains in the room around the experiment. Due to their texture, shape and weight they reduce noise and acoustic vibrations. Lastly, derived from the usual cleaving system in this setup [92], I developed a new miniaturized cleaving method for micrometric samples that was better suited for the iron pnictide samples that have been measured in this Ph.D. thesis.

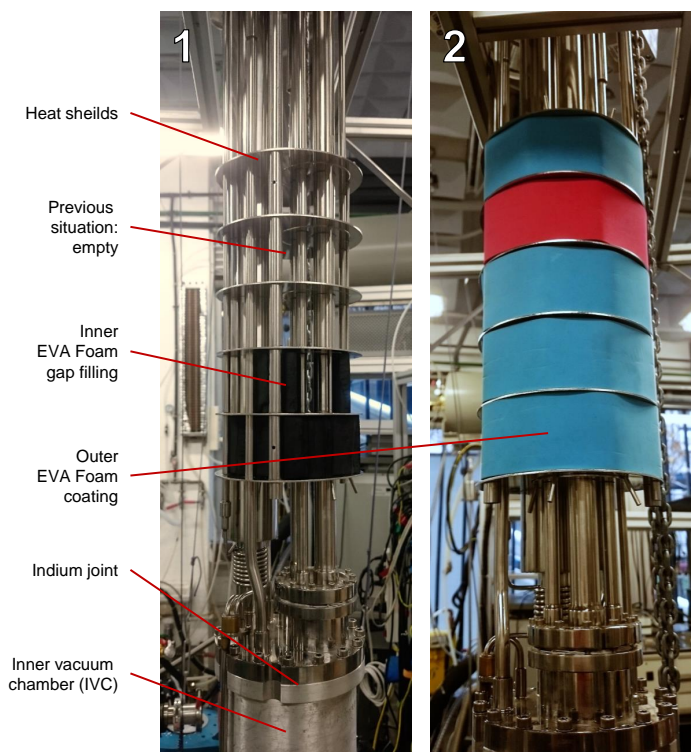


**Figure 2.5:** Detail photo of the EVA foam filling and wrapping process in the upper heat shields of the insert. The picture also depicts the indium joint which was polished to mitigate the leaks.

Another relevant aspect was the operation of the needle valve. Water vapor from the atmosphere leaked into it when pouring liquid  $N_2$  into the cryostat, so the valve clogged most of the times. To avoid this problem, we developed a closed circuit of He gas that cooled when passing through a copper serpentine immersed in liquid  $N_2$  and was injected directly into the cryostat. This allowed for the needle valve to be open to a constant flow of He through the entire cooling process and prevented any outerwater vapor to condense and freeze inside. This new clean and simple cooling method eliminated the need for liquid  $N_2$  into the cryostat [93].

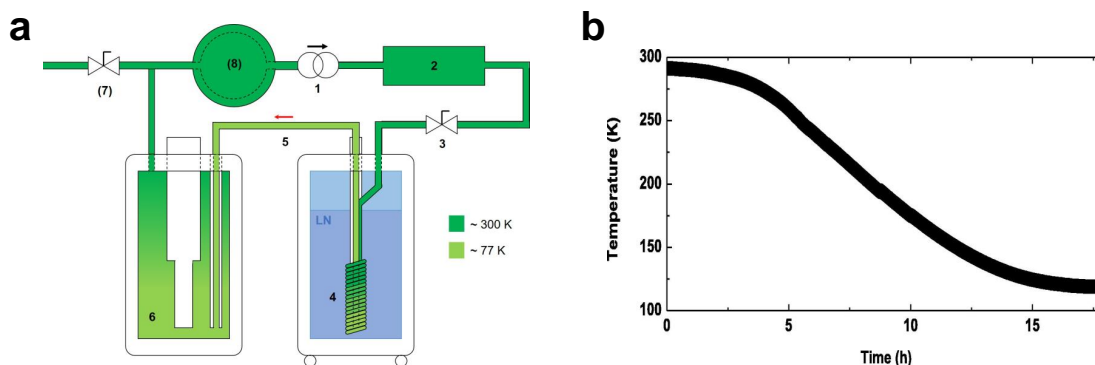


**Figure 2.6:** In (a) we show a diagram of the new liquid nitrogen-less cooling system. In (b) we can observe a typical cooling curve obtained with this method.

## 2.2 STM at low temperatures

STM is an experimental technique that combines the tunnel effect and the piezoelectric effect to achieve extremely high spatial resolution in conductive samples and probe the local electronic properties close to the Fermi energy. It was invented by Rohrer and Binnig at IBM laboratories in Zürich [94, 95, 96, 97]. Thanks to their invention, they were both awarded the Nobel Prize in 1986, only 4 years later, which gives an idea of the revolution it caused. In this section I will review the basic notions to understand its operation and results, as well as the actual implementation in our experimental setup and the improvements carried out in hardware and software.

Two electrodes separated by a nanometric insulating layer can have an electric current pass between them. This phenomenon, known as quantum tunnelling, is made possible thanks to the quantum nature of electrons at short distances. Bardeen proposed in 1961 the tunneling Hamiltonian formalism [98], which only two years after the invention of the STM was adapted by Tersoff and Hamann [99, 100] to explain the experimental phenomena, using typical sizes and energies observed in experiments. They found that the amplitude of the tunnel current is directly proportional to the density of states of the sample and it decays exponentially with the distance between the electrodes.

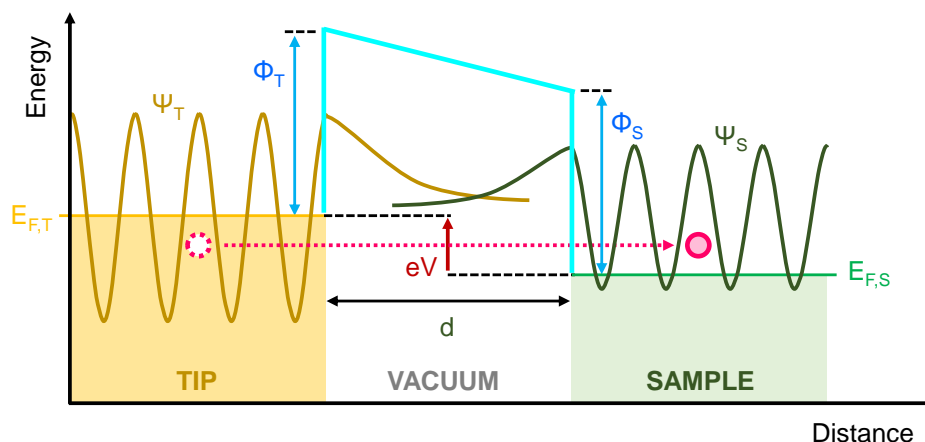


**Figure 2.7:** We represent schematically the tunneling process. The density of states (DOS) is shown as orange (tip's DOS) and green (sample's DOS), vacuum in white. A Bloch wavefunction in the tip is schematically shown by the brown line and by the green line in the sample. The surface potential is shown schematically by the light blue line and the work functions of tip and sample by the blue arrows. The voltage difference between tip and sample is schematically shown by a red arrow. The gap between tip and sample, of size  $d$  is represented by the black arrow. The tunneling current is represented schematically by a white disk (a hole) in the tip and a red disk (an electron) in the sample.

In the STM, the two electrodes are the tip and the sample. Using the Tersoff and Hamman first order approximation of the Bardeen's transfer formalism, we can

obtain the following expression for the tip-sample current:

$$I_{tip-sample}(V) = \frac{4\pi e}{\hbar} \int_{-\infty}^{+\infty} [f(\varepsilon + eV) - f(\varepsilon)] N_{sample}(\varepsilon + eV) N_{tip}(\varepsilon) |M|^2 d\varepsilon \quad (2.1)$$

Where  $f(E)$  is the Fermi distribution,  $N_{sample}$  is the density of states of the sample and  $N_{tip}$  is the density of states of the tip. We will refer to them in subsequent equations as  $N_s$  and  $N_t$  for simplicity. In this approximation, we can assume that the tunnelling matrix element  $M$  [98] is energy independent and constant through the tunnelling process.

Conversely, we should also consider the sample-tip current, which would have a similar expression. We will only consider from now on the total tunnelling current  $I_T$ , which is the sum of both contributions. The process is represented schematically in Fig. 2.7

The tunneling current depends exponentially on the distance  $d$  between both electrodes as:

$$I_T(d) \propto e^{-2\nu d} \quad (2.2)$$

Typical metals used in STM tips like Au or W have their work functions at around  $5 \text{ eV}$ , which leads to decay constants  $\nu$  to be around  $1 \text{ \AA}^{-1}$ , i.e. an increase (decrease) of  $1 \text{ \AA}$  in the tip-sample distance leads to a decrease (increase) of a factor of  $e^2 \approx 10$  in the tunnel current. This is what gives the STM its tremendous spatial resolution: very slight changes in height (or, in essence, electronic wave functions overlap) lead to large changes in tunnel current.

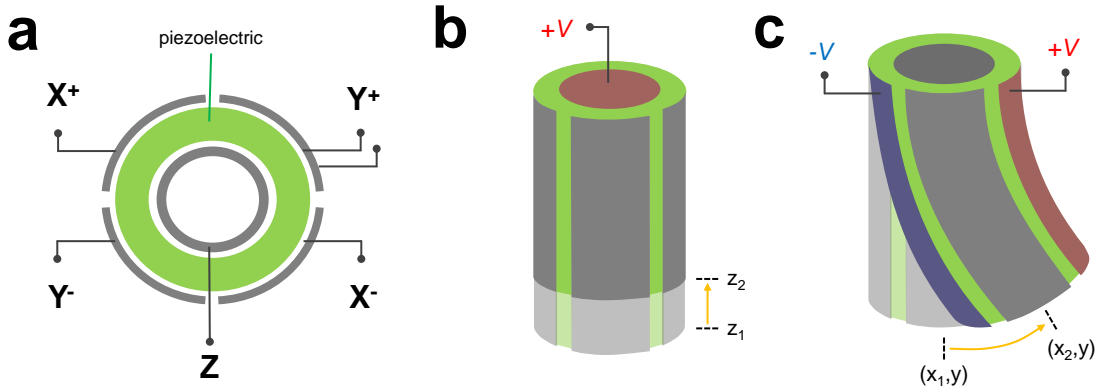


**Figure 2.8:** (a) Vertical cartoon representation of the piezotube. A hollow piezo cylinder is covered with four outer and one inner electrodes, with the tip (not shown) fixed at the bottom. (b) A voltage applied to the inner electrode will cause the piezotube to elongate or contract along its axis, modifying the tip's height. (c) A voltage applied to the outer electrodes will cause it to bend sideways, allowing for a fine XY scan.

The second main principle for the operation of the STM is the piezoelectric effect. If the tunnel effect is the physical phenomenon that allows for sub-nanometric sensitivity, the piezoelectric effect is the key to exploit it and control ultra-precise XYZ displacements of the tip. Piezoelectrics (from now on, piezos) are materials that deform in some way under an applied voltage. This deformation can be volumetric, directional or shear and it is usually written as a tensor.

In the STM used in this Ph.D. thesis we use a piezostack macroscopic tip height positioning system, explained elsewhere in detail [101], and a piezotube to control the fine positioning of the tip. The piezotube is a hollow piezo cylinder with four outer opposing and one inner electrodes ( $X^+$ ,  $X^-$ ,  $Y^+$ ,  $Y^-$  and  $Z$ , see Fig. 2.8). The tip is fixed to its bottom and it can scan a window up to  $2 \times 2 \mu\text{m}^2$  by applying voltages of the order of  $\pm 140$  V.

The rest of the components of the STM are shown in Fig. 2.9. This compact design is well suited for low temperatures and high magnetic fields. The titanium cylindrical central piece has a diameter of 50 mm. The tip cleaning and sharpening method, as well as the in-situ cleaving and macroscopic movement system have been extensively described elsewhere [90, 102, 103] and has been adapted and miniaturized in this Ph.D. thesis for micrometric samples.

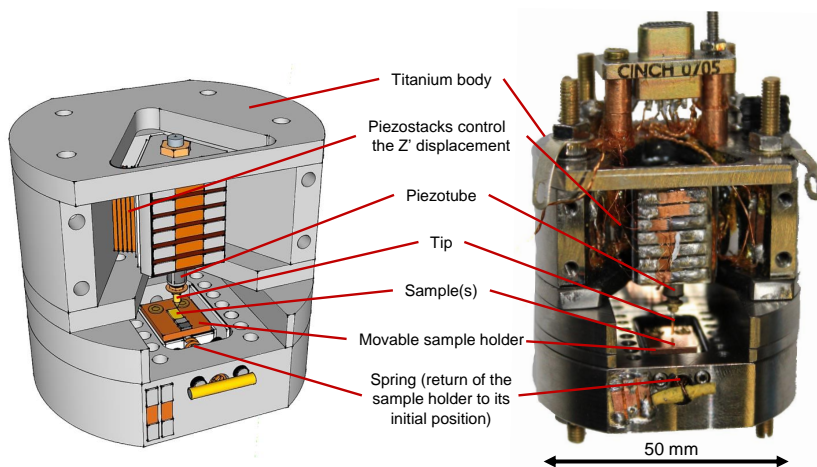


**Figure 2.9:** Schematic cartoon (left) and actual photography (right) of the STM, with its main parts indicated.

### 2.2.1 New micrometric cleaving method

Many single crystalline samples have been cleaved in the host laboratory in the past. Mostly these were however millimeter-sized samples. Some of the samples measured in this this Ph.D. thesis are thin plates of about 200 microns lateral size. This required a redesign of the cleaving method, which is schematized in Fig. 2.10(d-f) and compared to the classic cleaving method in Fig. 2.10(a-c).

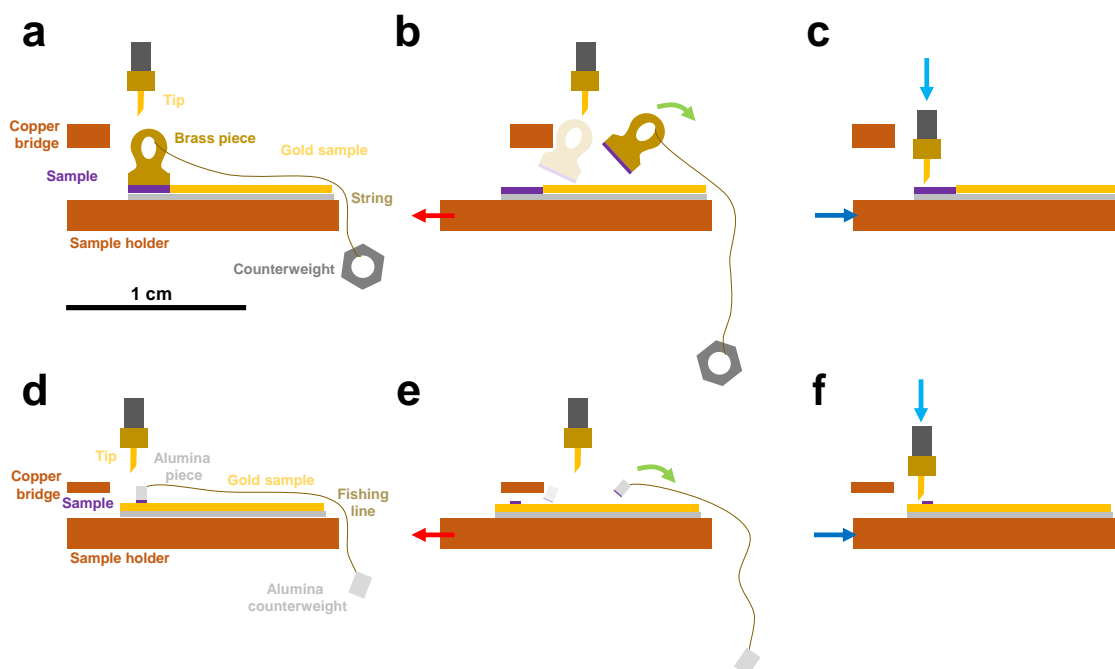


**Figure 2.10:** We compare the classic cleaving method (a-c) with the new micrometric cleaving method (d-f). In (a), the sample is mounted next to the sample and a brass piece is glued on top, which is then tied to a counterweight through a string. (b) When the sample holder is moved, the brass piece hits the copper bridge and the cleaved surface is exposed right below the tip (c) to start measuring. (d) With the new method, the micrometric sample is glued on top of the gold sample and the brass piece and counterweight are substituted by custom carved alumina pieces joined with a fishing wire. The copper bridge is smaller and closer to the sample. (e) When the sample holder moves, the alumina piece hits the copper bridge and cleaves the sample. (f) In this case, during the previous calibration of the tip position, its initial position is made off sample on purpose, just behind it. During the experiment, the sample holder is slowly moved until the tip eventually reaches the sample.

To cleave such small samples we first manually made a prism of alumina that had exactly the same base shape and size as the sample. We managed to do that by enclosing a piece of alumina into Crystalbond-509 and grinding it. We then glued the small alumina prism on the sample (Fig. 2.10(d)). We also made sure that the sample was glued on gold with silver epoxy, having gold on all sides (Fig. 2.10(d)). Finally, we took care to use a light counterweight so that the sample is not cleaved at high temperatures when manipulating the whole cryostat.

### 2.2.2 Image acquisition

The STM can be operated by scanning the tip at a constant height on top of the sample. This provides good images of the topography of the sample. However, it can only be made in surfaces which are very flat. The STM can also be operated

using a feedback loop that maintains the current at a constant value by acting on the  $z$ -position of the tip. Thus, any step or feature that appears during scanning is avoided thanks to the feedback loop (see Fig. 2.11). This is the way we have worked in this Ph.D. thesis.

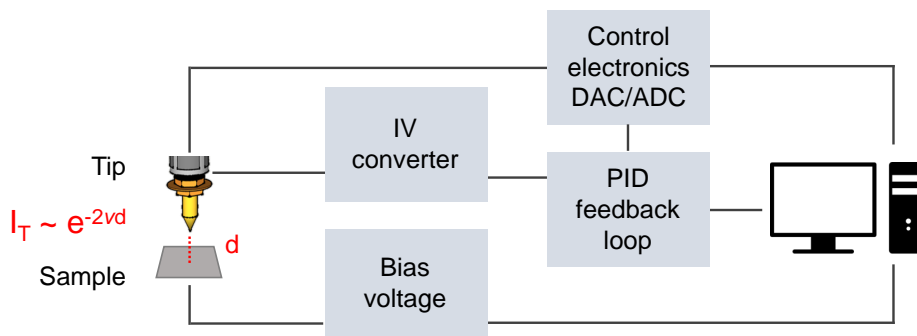


**Figure 2.11:** Schematic representation of the electronics used in the experimental setup to set, control and measure scanning tunnelling images.

The tunneling current at zero temperature for a tip with a featureless density of states can be written as:

$$I_T(V) = \frac{4\pi e}{h} |M|^2 N_t \int_0^{eV} N_s(\varepsilon) d\varepsilon \quad (2.3)$$

From this, we can see that the tunneling current is the integral of the density of states between the Fermi level and the bias voltage. When measuring at a constant current we thus obtain this information through the value of the signal to the feedback. By plotting the value of the feedback as a function of the position during a scan, we thus make an image of the integrated density of states between the Fermi level and the bias voltage. If we take the derivative of the tunneling current (at zero temperature), we obtain the conductance, which is equal to the density of states, following:

$$\sigma_T = \left. \frac{dI_T(V)}{dV} \right|_{T \rightarrow 0} \propto N_s(eV) \quad (2.4)$$

At a finite temperature, the tunneling conductance is given by the temperature convoluted with the density of states. We can schematically describe the behavior using Fig. 2.12. When we have a normal tip and a normal sample, both with a featureless density of states, we obtain a linear I-V curve (Fig. 2.12(a-c)). When measuring a superconductor with a normal tip, we obtain zero current inside the superconducting gap and the derivative is very similar to the density of states (Fig. 2.12(d)). The current at zero bias is zero, and it increases with a finite bias, because the temperature modifies the distribution of occupied and unoccupied states. When increasing the bias, there are overlapping electron and hole states that are empty or full due to thermal excitation (Fig. 2.12(f)). When measuring with tip and sample being both superconductors (Fig. 2.12(g-i)), the same occurs, but

there is an increased current at the bias voltage for which the quasiparticle peaks of tip and current overlap, which is equal to the difference between both gap values (Fig. 2.12(i)).

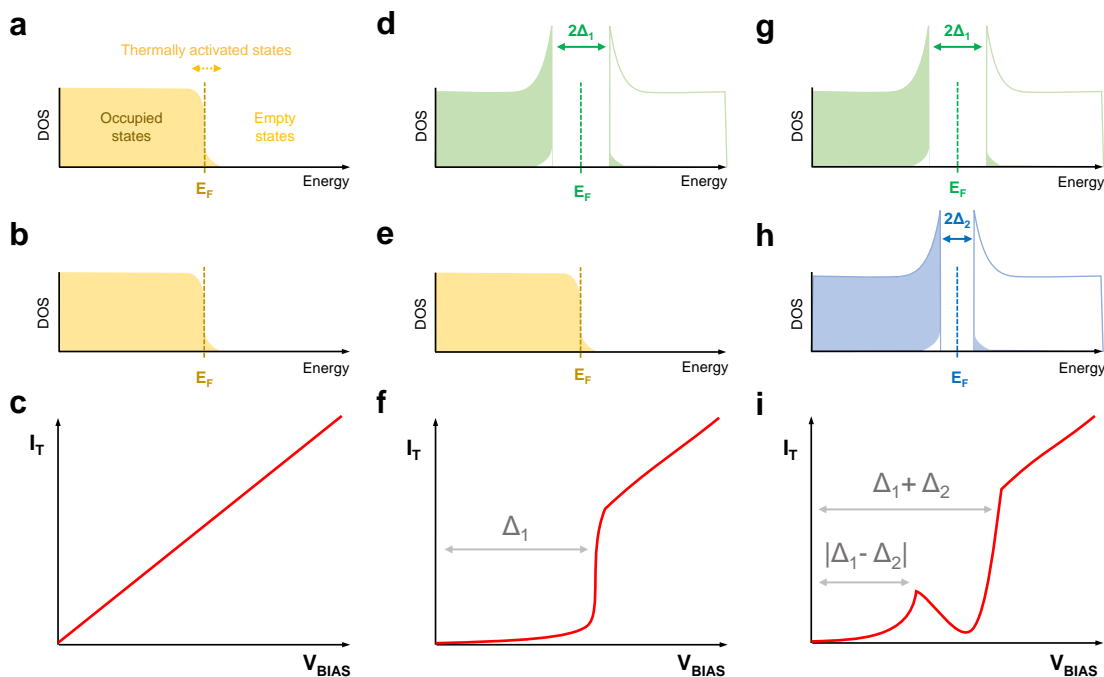


**Figure 2.12:** Density of states of sample (a,d,g) and tip (b,e,h) and typical typical IV curves (c,f,i) obtained in three different scenarios: normal tip and sample (a-c), normal tip and superconducting sample (d-f) and superconducting tip and sample (g-i).

## 2.3 Synthesis of intermetallic single crystals

### 2.3.1 Flux growth of binary intermetallic compounds

An interesting method to obtain single crystals is the flux growth or solution growth method. The method requires a deep knowledge and intuition to find systems that can be grown with high quality. Prof Paul C. Canfield has described the method in detail in several works [104, 105, 106]. An brief summary follows:

1. *Study of the phase diagram.* The solution growth requires precise study of phase diagrams. An example of a binary phase diagram is provided below.
2. *Preparation of the crucibles.* The starting composition is weighed in a precision scale and put inside an alumina crucible that will act as the reaction pot.
3. *Preparation of the ampoule.* The crucible is put inside a silica ampoule previously closed at its bottom. Then an alumina frit filter and another upside down crucible are put on top of it to effectively close the reaction chamber.

Some quartz wool in the top and bottom acts as cushion. The ampoule is then evacuated, filled with a thin inert gas atmosphere and closed with a hydrogen torch.

4. *Thermal cycle in the furnace.* The ampoule is put inside a furnace programmed with the previously calculated thermal cycle. Typical cycle times range from 100 to 300 hours and consist of a rapid heating followed by a very slow cooldown. Most of the starting materials melt and mix at the beginning of the cycle, and then the desired crystal starts precipitating from the liquid upon cooling. The slow cooling rate in a favorable solvent environment allows for the coherent block-building of the single crystals over large sizes.
5. *Centrifugation.* Solution growth is ideal to obtain compositions which occur when melting is incongruent. Then, usually the crystals are obtained by spinning the liquid, as described later on with an example.
6. *Extraction and cleaning of the single crystals.* The ampoule is broken and the crystals extracted from the crucible.

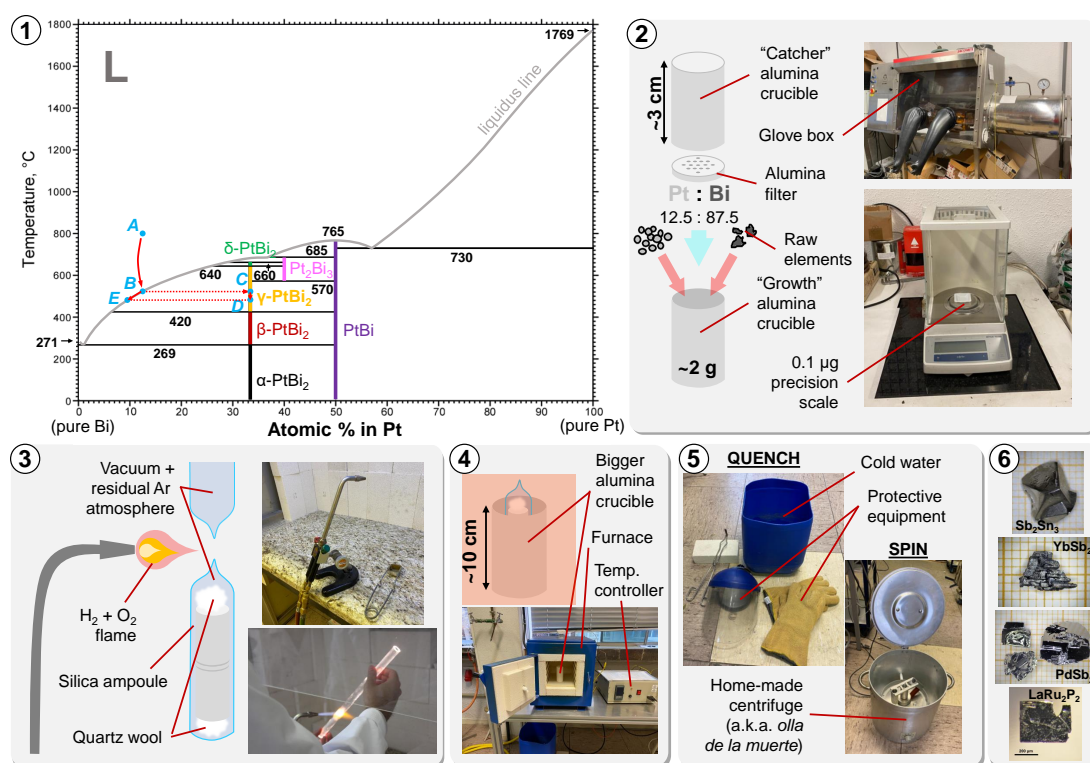


**Figure 2.13:** Solution growth of  $\gamma$ - $\text{Bi}_2\text{Pt}$ , with schematic representations and actual photos of the components. After a thorough study of phase diagram (1) the initial composition is weighed (2), sealed inside the ampoule (3) and put inside of the furnace (4). Then it is rapidly heated above the liquidus line (1A) and then slowly cooled down. The moment it crosses back the liquidus line (1B) the crystal starts forming (1C) as the liquid gets poorer in Pt (1E). When enough crystal has formed (1D), the crystal is quenched (5) and extracted from the crucible (6).

Let us discuss the example of  $\gamma$ -Bi<sub>2</sub>Pt. The binary Bi-Pt phase diagram is shown in Fig. 2.13. We see that the  $\gamma$ -Bi<sub>2</sub>Pt phase can only be obtained by cooling a mixture of liquid and  $\gamma$ -Bi<sub>2</sub>Pt. We may start with a composition and temperature A and cool. When we reach B, crystals start to form (C). When we cool further, part of the crucible has solid crystals of  $\gamma$ -Bi<sub>2</sub>Pt (D) and the other part liquid with a composition (E). We can then spin the ampoule, so that the whole growth is forced to go through a filter. The crystals remain at one side and the liquid is poured to the other side of the filter. We can then recover the crystals.

### 2.3.2 International stay at AmesLab

I participated in the initiative of materials synthesis at the LBTUAM since its beginning. I helped improving many aspects of the materials synthesis lab. The lab has two programmable furnaces, a hydrogen torch in a fireproof hood and a pumping system and valve manifold. The centrifuge is home-made.

I started learning and practising my first crystal growths during my Physics degree in the La-Pb system. I kept improving in my master's degree, focusing on the synthesis of the iron-free pnictide superconductor LaRu<sub>2</sub>P<sub>2</sub>. The results on these crystals were recently published after further magnetoresistance measurements by the group [85]. Due to my high interest in this field, I was offered to do a 4 month international research stay at AmesLab Iowa (USA), home office of Paul Canfield's group. There I found top level crystal growth facilities and I could actively participate in state of the art growth techniques of pure and Ni-doped CaKFe<sub>4</sub>As<sub>4</sub> [107, 57, 58, 37]. I did also research on the Cs-Eu-Fe-As quaternary system as well as other well-known representatives of the pnictide family like CsFe<sub>2</sub>As<sub>2</sub> or KFe<sub>2</sub>As<sub>2</sub>.

After the return to my home institution, thanks to the newly gained knowledge I helped to develop several improvements to the crystal growth facilities. We increased the size of the fireproof hood and added more pumping lines with a new argon filled high pressure line. We got a new bigger 1200°C furnace and we placed it inside of a new aspiration hood. We improved the arc furnace cooling system and designed a new setup for cleaner blasts. We implemented a new temperature controller and developed a new database catalog that accounted for every sample that was ever grown in, or sent to LBTUAM, assigning a unique code to each batch.

One of the most interesting compounds grown at LBTUAM is  $\gamma$ -Bi<sub>2</sub>Pt. It has a layered trigonal structure and presents a very interesting orientational dependence of the magnetoresistance, switching from a saturating behavior with the field parallel to the plane to a nonsaturating behavior up to 20 T when the external field is perpendicular to the *ab* plane. In between at the very specific magic angle of 8.3°, the magnetoresistance is perfectly linear due to the open orbits in the Fermi surface [83]. Fig. 2.14 shows the main results obtained in the  $\gamma$ -Bi<sub>2</sub>Pt system.

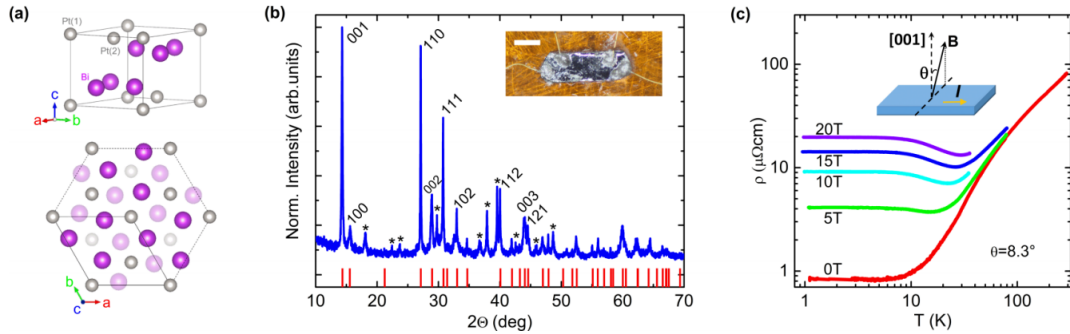


**Figure 2.14:** Extracted from Ref. [83]. (a) Crystal structure of  $\gamma$ -Bi<sub>2</sub>Pt. (b) In blue, we show the x-ray diffraction pattern of  $\gamma$ -Bi<sub>2</sub>Pt powder. Red bars show the positions of the peaks expected to appear in this compound. The asterisks mark the peaks associated with residual Bi and Bi oxides from flux growth. The inset shows a picture of the single crystal with four contacts used for resistivity measurements. The white scale bar is 0.2 mm long. (c) Colored lines show the temperature dependence of the resistivity at different magnetic fields. The field is applied at an angle  $\theta=8.3^\circ$ , which is also the precise angle at which we find nonsaturating linear magnetoresistance. The temperature dependence is very similar for all field orientations. The inset shows a scheme of the direction of the applied current and magnetic field.

### 2.3.3 Growth and characterization of crystals of iron based superconductors: 1144 and Ba122 systems.

One of the main goals of the international stay at Ames was to produce high quality ternary and quaternary iron based superconductors at their specialized facilities, which had special fumehoods and gloveboxes to operate with toxic arsenides. In collaboration with W. R. Meier, we studied and expanded the grounds for the successful growth of pure and doped crystals of CaKFe<sub>4</sub>As<sub>4</sub> [108]. The crystals from those very same batches we obtained at AmesLab back travelled to Spain at my return and were object of intense study by J. Benito-Llorens, with my collaboration [101, 13].

As more elements are introduced in the mixture, the dimension of the phase diagram increases. In the case of a quaternary compound like CaKFe<sub>4</sub>As<sub>4</sub>, the phase diagram is not a bidimensional map with equilibrium lines like the one depicted in Fig. 2.13(a), but a five-dimensional object in which each element is at the corner of a tetrahedron and the temperature sets isovolumes inside. To operate with such a complex object, it is always a good idea to decompose the problem into simpler approximations that let us reduce the degrees of freedom.

This was made by W. R. Meier during his Ph.D. In the case of CaKFe<sub>4</sub>As<sub>4</sub>, the four corners at Ca, K, Fe and As can be intersected by planes which represent simple combinations of them that eventually reduce the problem to a much simpler pseudoternary phase diagram between CaFe<sub>2</sub>As<sub>2</sub>, KFe<sub>2</sub>As<sub>2</sub> and FeAs, as depicted in Fig. 2.15. Then a Marco Polo-type approach was taken to explore the phase

diagram and probe the resulting compounds for each starting composition. The best results were obtained with starting molar ratios inside the ampoule 1.2:0.8:1 of K:Ca:Fe<sub>0.512</sub>As<sub>0.488</sub> and a temperature profile like the following: from room temperature to 650°C in 1h, stay there for 3h, up to 1180°C in 2h, stay there for 5h, cool down to 1050°C in 2h, stay there for 0.5h, finally cool down to 930°C in 30.5h and spin. The process is described in great detail in Ref. [108].

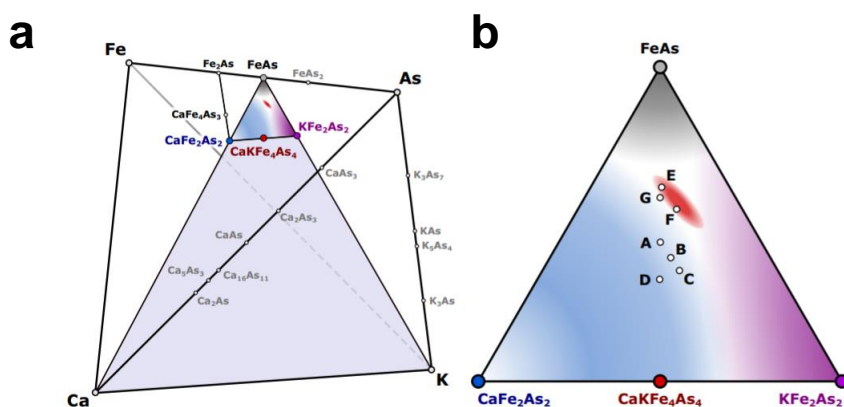


**Figure 2.15:** Extracted from Ref. [108]. (a) The three-dimensional quaternary Ca-K-Fe-As phase diagram. The shaded blue-gray plane represents the compositions with equal iron and arsenic fractions. The red ellipse below FeAs represents the primary solidification region (primary phase field) of CaKFe<sub>4</sub>As<sub>4</sub> (compositions where pure single crystals can be grown) determined through optimization. (b) An enlarged pseudoternary phase diagram of composition near FeAs. The proposed primary solidification regions of each phase are shaded. Blue is CaFe<sub>2</sub>As<sub>2</sub>, gray is FeAs, red is CaKFe<sub>4</sub>As<sub>4</sub>, and purple is KFe<sub>2</sub>As<sub>2</sub>.

The crystal growth of BaFe<sub>2</sub>(As<sub>1-x</sub>P<sub>x</sub>)<sub>2</sub> was tackled starting from a ternary phase diagram. The difficulty is much different, as the starting point is easier to comprehend. This growth was made by the group of I. R. Fisher at Stanford. For most of the desired As/P compositions, micron-sized crystals can be obtained by mixing stoichiometric mixtures of Ba and FeAs/FeP/As/P inside of the ampoule, depending on the target. The most successful temperature cycle involved dwelling at 700 °C for 12 hours before warming up to 1190 °C over 18 hours, then holding at the peak temperature for 12 hours. The cooldown was also key in determining the doping and homogeneity of the crystals [109]. The cooldown procedure was as follows: 1190 °C to 1090 °C in 60 hours, 1090 °C to 995 °C in 60 hours and finally 995 °C to 950 °C in 72 hours [109]. The quality of the crystals could further be improved by annealing for a week at 950 °C. Additional details about the growth are available in the supplementary information of Ref. [109].

It turns out that, alas, I did not include any study made with a crystal I grew into this Ph.D. thesis. The reasons why I did not study the samples I grew with the STM are varied. Either the system had already received attention by my colleagues (CaKFe<sub>4</sub>As<sub>4</sub>), it lead to samples that were too small and scarce to measure using my STM (LaRu<sub>2</sub>P<sub>2</sub>) or it did not cleave well and were too far from the aims of

my PhD ( $\gamma$ -Bi<sub>2</sub>Pt, Ru<sub>2</sub>Sn<sub>3</sub> and the compounds of the La-Pb series). This shows that sample and technique often go together, and STM requires a particular set of single crystalline samples that provide neat surfaces and are available in large quantities to make many cleaves. It is certainly a remaining challenge for my host laboratory to tackle this issue in future. I also must say that I got into unexpected results in very basic problems regarding STM measurements, thanks also to the improvements I made in my equipment. I decided to prioritize understanding such results (Josephson effect and YSR states), simply because I managed to unveil them for the first time.

## 2.4 Interpretation of patterns in images of the density of states

### 2.4.1 Scanning Tunneling Spectroscopy

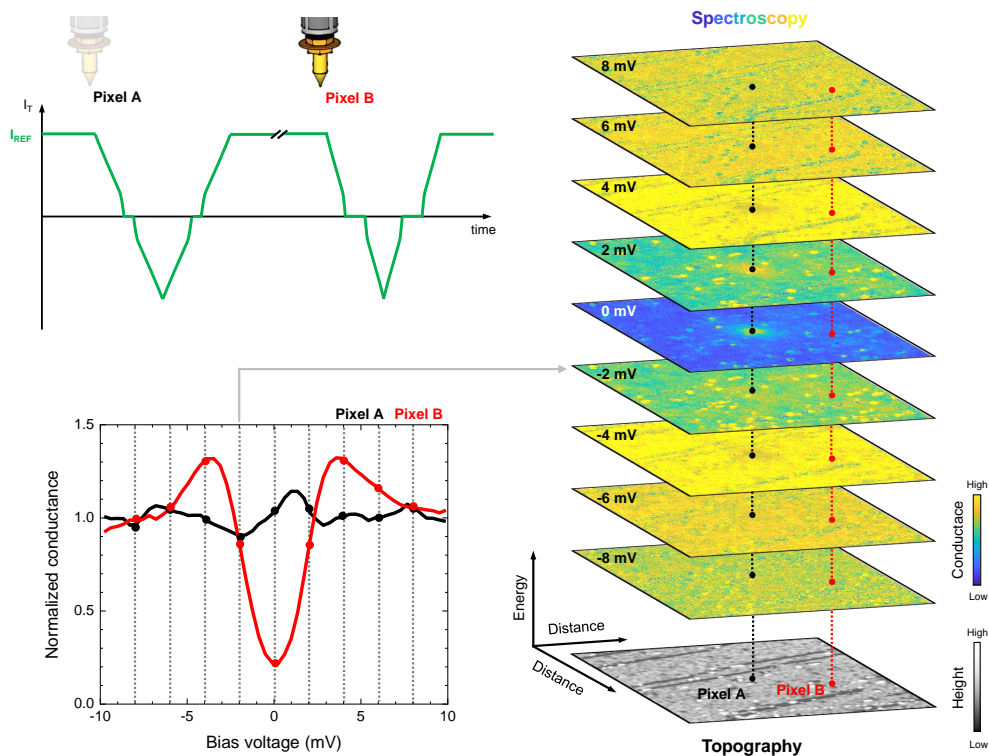


**Figure 2.16:** Typical STS measurement. For every pixel, the computer opens the PID loop and takes two I-V curves at constant height. By taking the derivative of all these I-V curves, one can obtain the conductance map at each bias voltage. In the figure, we show the importance of this technique by selecting and highlighting the I-V and conductance curves of two different pixels A and B, which seem to have a similar value of the height in the topography but behave in a very different way with respect to the bias voltage, as pixel A is inside a vortex core.

Topography images measure the tunnel current value at a fixed bias voltage and thus show the integrated contribution of the LDOS from the Fermi level to the applied bias voltage. However, one could also wonder what the energy dependence of the LDOS looks like (see Equation 2.5). This can be realized with Scanning Tunneling Spectroscopy (STS) measurements, in which the feedback loop is opened, the height is kept constant and two I-V curves (ramp up and ramp down) are taken and recorded for every pixel in the image. This way we can measure the tunnel current not only as a function of the position of the tip, but also as a function of the bias voltage at each point. STS is the key to unveil and study some crucial features in superconductors like vortices, YSR states or pair breaking defects, which usually don't show in topographies and we will thoroughly discuss in this Ph.D. thesis. In Fig. 2.16 we can see a detailed explanation of the acquisition and interpretation process of STS measurements.

## 2.4.2 Quasi-Particle Interference imaging

Apart from vortex imaging, which has been extensively described elsewhere [31], one of the main techniques derived from STS is Quasi-Particle Interference imaging (or QPI, for short). Together with ARPES [110], it is a very powerful tool to determine the band structure in metals and superconductors, with the main advantage over photoemission that it is able to both probe the occupied and unoccupied electronic states [111, 112].

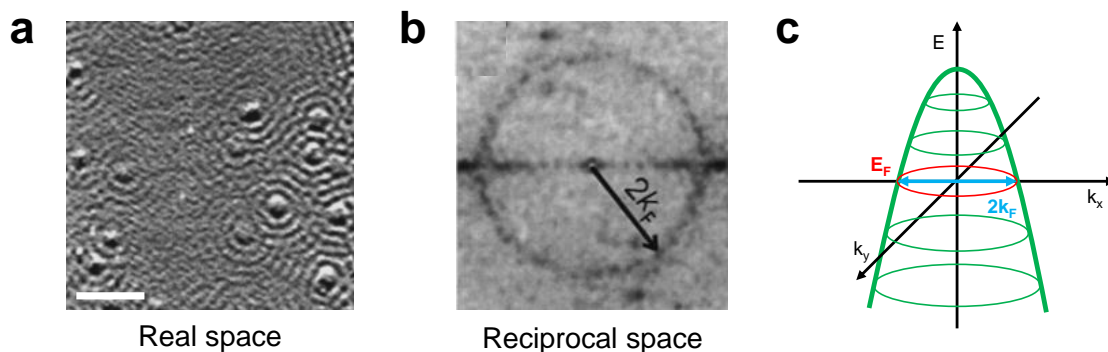


**Figure 2.17:** Basic example of a QPI scattering pattern, adapted from Ref. [113]. In (a) we show a STS image at zero bias and 150 mK of a flat Cu(111) surface. White scale bar is 10 nm long. Instead of a homogeneous LDOS, we can see that some point defects cause conduction electrons to scatter oscillations in all directions. (b) The Fourier transform reveals that in reciprocal space all scattering events have a characteristic momentum  $2k_F$ , which is set by the shape and size of the parabolic conduction band of Cu, here represented as a 2D cartoon in (c).

In an ideal metal, the momentum eigenstates of the LDOS are the Bloch functions  $\Psi(\mathbf{r}_k)$ . From the relation:

$$LDOS(E, \mathbf{r}) \propto \sum_{\mathbf{k}} |\Psi(\mathbf{r}_k)|^2 \delta(E - \varepsilon(\mathbf{k})) \quad (2.5)$$

one can see that introducing Bloch functions does not produce any observable spatial modulation with wave vector  $\mathbf{k}$ . Thus, the LDOS is spatially homogeneous. However, in the presence of defects or impurities, the crystal lattice periodicity is broken and scattered conduction electrons produce oscillating patterns on the surface, which are sometimes named Friedel-like oscillations [114, 115]. These oscillations resemble the waves produced when throwing a stone into a pond in the simplest isotropic parabolic band case depicted in Fig. 2.17, but usually are more complex in most samples, which have an intricate band structure.

To discuss QPI, we can consider only elastic scattering, i.e. events that move electrons between two states with the same energy and wave vectors  $\mathbf{k}_1$  and  $\mathbf{k}_2$ . Thus, scattering patterns are observed at wave vectors  $\mathbf{q} = |\mathbf{k}_1 - \mathbf{k}_2|$  [116]. The intensity of the scattering patterns is proportional to the joint density of states (JDOS), the density of states at  $\mathbf{k}_1$  multiplied by the density of states at  $\mathbf{k}_2$ . The density of states is inversely proportional to the energy derivative of the dispersion relation. Thus, an increased JDOS is observed close to van Hove anomalies or places with a flat dispersion relation. On the other hand, an enhanced JDOS is also found when the band structure has parallel portions on the surface. Finally, one should bear in mind that the electronic oscillations may be modulated by the local potential of the scatterer impurity, which usually depends on the type and shape of the impurity or defect and may affect the QPI signal in some directions, as for instance at a step edge, where only the scattering perpendicular to the edge will be visible [117, 118, 119, 120].

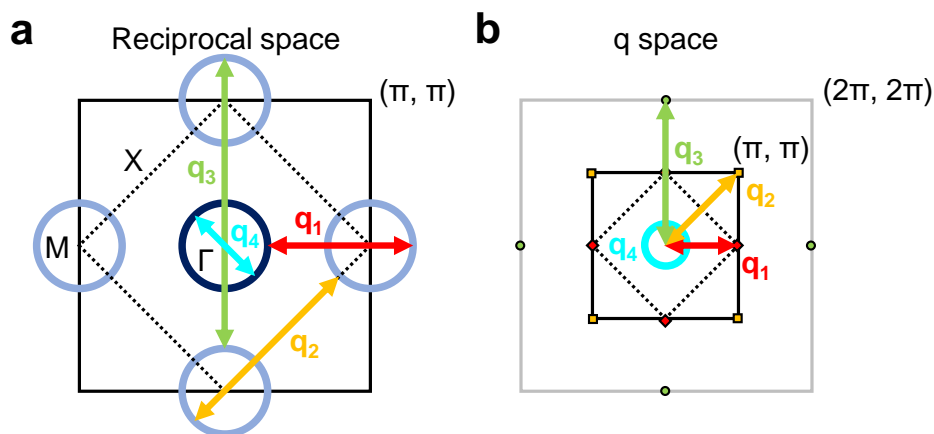


**Figure 2.18:** Adapted from Ref. [121]. We show in (a) schematically a simplified Fermi surface of a square lattice. We assume one central pocket (dark blue circle), whose size is exactly equal to pockets (light blue circles) at the corners of the Brillouin zone (dashed lines). We represent the main scattering vectors (see also text) as arrows. In (b) we show the expected scattering pattern. Notice the change in size of the field of view in reciprocal space. The scattering vectors are represented as arrows, and correspond to points or circles in  $q$  space.

In Fig. 2.18 we discuss with an example the relation between the band structure

(Fig. 2.18(a)) and the scattering pattern (Fig. 2.18(b)). We see that scattering of two spherical Fermi surfaces ( $q_1$ ) leads to four Bragg peaks, provided that the two surfaces are exactly equal. Scattering among the same Fermi surface ( $q_2$  and  $q_3$ ) leads to eight Bragg peaks (yellow and green in Fig. 2.18(b)). Isotropic scattering inside a band ( $q_4$ ) will generate a circular pattern (blue circle in Fig. 2.18(b)). The scattering patterns extend over the size of the first Brillouin zone (Fig. 2.18(a)). In Fig. 2.18(b) the plane axis are doubled.

### 2.4.3 QPI analysis software

In order to analyze the raw data produced by the experiments, we developed at LBTUAM a Matlab based software named *blqAnalysis*. The current version of the software can be downloaded from [here](#) and provides a broad set of tools to analyze topographies and conductance maps, like conductance curves smoothing, Delaunay triangulation with automatic vortex recognition, number and distance to nearest neighbors, vortex core size fitting, multifractal analysis, gap map, removal of bad points and lines, dynamic equalization of the contrast, gaussian filter, temperature deconvolution, mass exporting of the conductance maps and Fourier transforms or conductance averaging of a region [122].

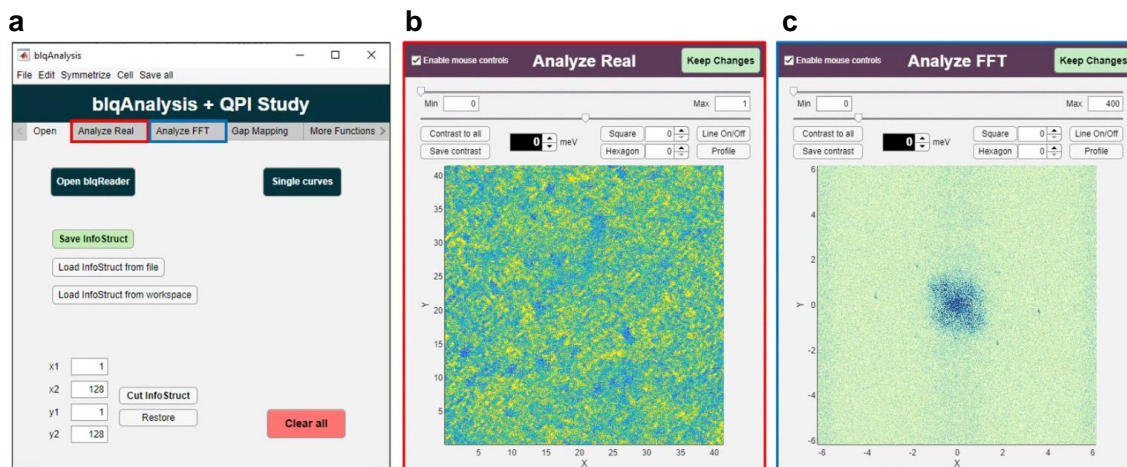


**Figure 2.19:** (a) Main window of the *blqAnalysis* Matlab program. Clicking on the highlighted red and blue tabs will open a new analysis applet for the real (b) and reciprocal space (c). Other buttons, sliders and tabs will as well call different functions or applets to perform other more specific analysis.

My main contributions to it have been the calculation and representation of the Autocorrelation Function of an image (see subsection 2.4.4), the obtention of the differential strain map from the Lawler-Fujita algorithm (see subsection 2.4.5) and many improvements in QPI pattern noise reduction and manipulation, like a symmetrization applet compatible with a wide set of crystalline geometries. We show in Fig. 2.19 a typical screenshot of the QPI analysis applet together with the main app, analyzing data obtained from a  $\text{BaFe}_2(\text{As}_{0.7}\text{P}_{0.3})_2$  sample.

To enhance the signal to noise ratio, we can take advantage of the periodicity of the lattice and make a symmetrization of the scattering pattern following the symmetry of the lattice. For example, in a surface with a hexagonal atomic arrangement, a C6 symmetrization (see Fig. 2.20) produces a clearer visualization of the scattering patterns.

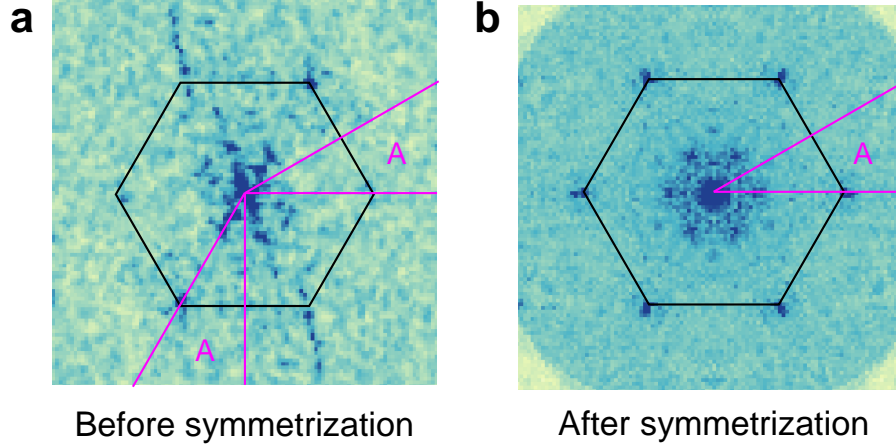


**Figure 2.20:** Fourier transform of the conductance map of a 2H-NbSe<sub>2</sub> sample before (a) and after (b) the symmetrization process. Due to crystalline symmetry arguments, the two sectors A highlighted in (a) are averaged out between them and the rest of the equivalent sectors. After the process, the periodic features are more prominent and the noise has greatly canceled out. Every sector in the symmetrized image (b) is either a reflection or a rotation of sector A.

#### 2.4.4 The autocorrelation function

The statistical autocorrelation function (*ACF*) is an offset independent method that measures the correlation between any two points separated by a distance  $r$ . The spatial autocorrelation function  $ACF(\mathbf{r})$  of an image is given by the correlation of any two pixels  $i$  and  $j$  of the image that are separated by a given vector  $\mathbf{r} = (r, \theta) = \mathbf{r}_i - \mathbf{r}_j$ , where  $\mathbf{r}_i$  and  $\mathbf{r}_j$  are the position of those pixels. We can define it as:

$$ACF(\mathbf{r}) = \frac{1}{N(\mathbf{r})} \sum_{i,j} \frac{(I_i - \langle I \rangle_1)(I_j - \langle I \rangle_2)}{\sigma_1 \sigma_2} \quad (2.6)$$

where

$$N(\mathbf{r}) = \sum_{i,j} \delta_{\mathbf{r},(\mathbf{r}_i - \mathbf{r}_j)} \quad (2.7)$$

$$\langle I \rangle_1 = \frac{1}{N(\mathbf{r})} \sum_{i,j} \delta_{\mathbf{r},(\mathbf{r}_i - \mathbf{r}_j)} I_i \quad (2.8)$$

$$\langle I \rangle_2 = \frac{1}{N(\mathbf{r})} \sum_{i,j} \delta_{\mathbf{r},(\mathbf{r}_i-\mathbf{r}_j)} I_j \quad (2.9)$$

$$\sigma_1^2 = \left( \frac{1}{N(\mathbf{r})} \sum_{i,j} \delta_{\mathbf{r},(\mathbf{r}_i-\mathbf{r}_j)} I_i^2 \right) - (\langle I \rangle_1)^2 \quad (2.10)$$

$$\sigma_2^2 = \left( \frac{1}{N(\mathbf{r})} \sum_{i,j} \delta_{\mathbf{r},(\mathbf{r}_i-\mathbf{r}_j)} I_j^2 \right) - (\langle I \rangle_2)^2 \quad (2.11)$$

This function multiplies the value of every pixel in an image with every other pixel and performs a weighted average between all the couples of pixels that are at the same distance and angle between them. The function builds a matrix in which every element corresponds to a certain  $(r, \theta)$  and its value is the weighed average intensity of all the pixels at that specific distance and angle between them. If that distance or orientation has a particularly high amount of, let's say pixels with high intensity, that *ACF* matrix element will have a high intensity as well. Note that not every combination of  $r$  and  $\theta$  is possible, for instance there are no two adjacent pixels at  $30^\circ$ . Similarly, in a square image of  $N \times N$  pixels, there is only one couple of pixels at  $r = \sqrt{2}N$  and  $\theta = 45^\circ$ : the upper right with the lower left. This uneven pixel couples distribution is taken into account through the normalization by  $N(\mathbf{r})$ . The variance calculation ensures that statistical exceptions like bad points don't dominate the average value for that  $(r, \theta)$ .

The radially averaged autocorrelation function  $ACF(r)$  is the result of averaging the  $ACF(\mathbf{r})$  value for all the vectors with the same magnitude  $r = |\mathbf{r}|$ . It gives an idea of the spatial extension of the correlated regions in the image and the typical distance between these regions, regardless of their orientation. Conversely, the angular averaged autocorrelation function  $ACF(\theta)$  represents the correlation value between any two pixels at a certain angle, regardless of their distance. A white noise image will have a flat and close to zero  $ACF(r)$  for all distances with however a sharp peak at  $r = 0$ , because every pixel is correlated with itself. In real images, peaks in  $ACF(r)$  mean that those are regions where pixel intensities are spatially correlated, within the same region (the peak is centered at zero) or with neighboring regions (the peak is at a finite value). Moreover, after a proper polar to cartesian transformation, one can obtain an actual  $(r, \theta)$  *image* of the  $ACF(\mathbf{r})$  in which one can simultaneously observe the radial and angular dependence of the correlation in real space and study the shape and orientation of the bright (high correlation) and dark (anticorrelation) regions. Fig. 2.21 shows through an example the key advantages of this method: we are able to extract the main relevant features of any pattern present in an image even if it seems absent at first sight. The *ACF* is still able in the most heavily disordered picture to extract the relevant information about the underlying lattice, like the average “atomic” size and shape, as well as the lattice axes and the first neighbor distance through the radial average.

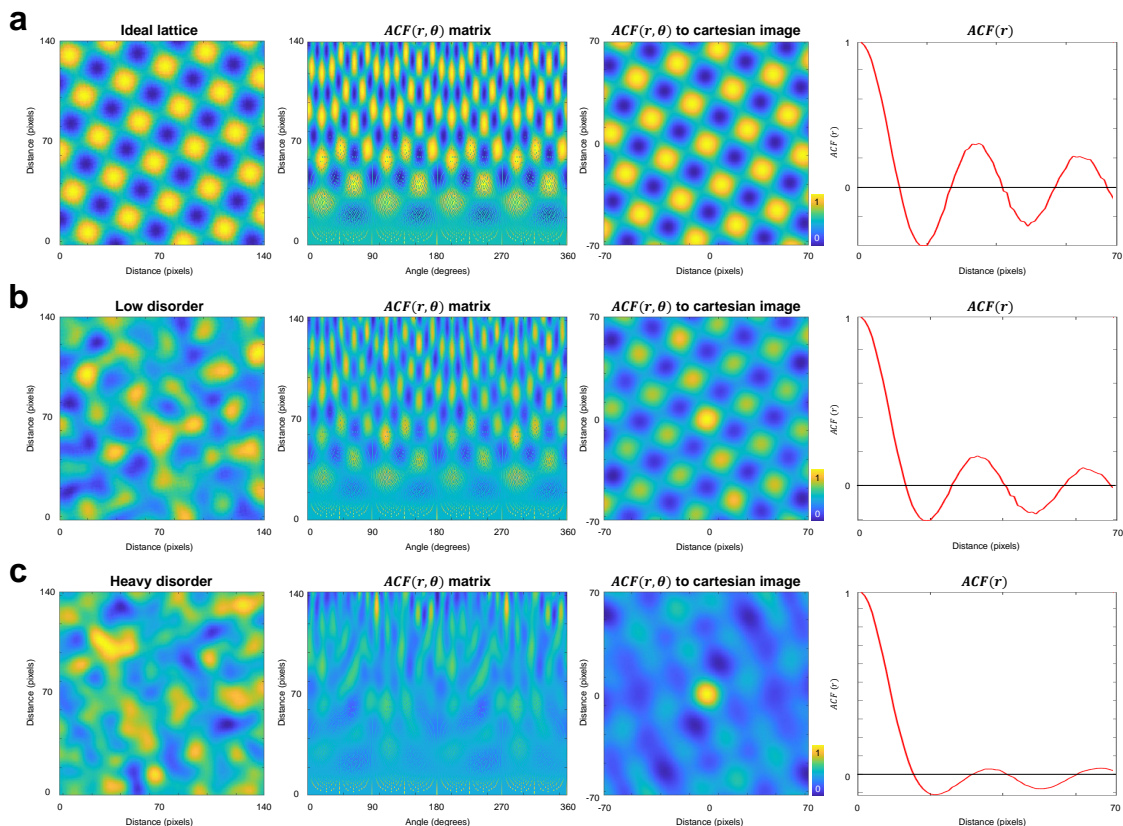


**Figure 2.21:** First panel is a simulated  $140 \times 140$  pixels topography of a square lattice of atoms, second panel is the calculated autocorrelation function matrix where the rows are different distances and the columns are different angles; third panel is the cartesian image reconstructed from the distance and angle information from the  $ACF$  matrix and fourth panel is the radially averaged  $ACF$  in the case of: an ideal lattice (a), low disorder (b) and high disorder (c). The color scale is indicated in the colorbar on the right hand side of the images. As we see, even in the highly disordered case where pattern finding is difficult in the topography image, the  $ACF$  is able to find the main relevant features and length scales of the underlying lattice.

The calculation of the statistical  $ACF(r)$  is an extremely powerful tool to unveil the hidden patterns and symmetries of heavily disordered samples and it has been successfully used to understand the role of Coulomb interactions in TiN, a disordered metal in the vicinity of a superconductor to insulator transition [123], as well as to obtain spatial dependencies related to the opening of the pseudogap in cuprates [124] or to find surface patterns in oxide samples or graphene coatings [125, 126].

### 2.4.5 The Lawler-Fujita algorithm

Strain or pressure are one of the main non-thermal control parameters that can heavily modify the band structure of a material and trigger new phases, in particular in susceptible materials with competing ground states like iron based superconductors or heavy fermions [127, 128, 129, 130, 131]. While experimental

research has fundamentally addressed hydrostatic pressure or bulk strain, there can be some local effects at the atomic level associated to crystalline defects or impurities. Such effects will average out in the bulk measurements, yet they may impact our STM measurements by locally altering the electronic properties of the material over a nanometric sized region.

The method proposed by Lawler and Fujita in 2010 [132], known as the Lawler-Fujita algorithm, provides the bases for a local strain map calculation in STM topography images. The crystalline topography is modeled as the combination of several modulations: the atomic modulation  $\mathbf{Q}_x$  and  $\mathbf{Q}_y$ , a possible super-lattice modulation due to CDW or similar phenomena  $\mathbf{Q}_{sup}$  and a slowly varying apparent displacement due to long-term and picometer scale piezoelectric drift. We can define the slowly varying displacement vector field  $\bar{u}(\mathbf{r}) = (u_x(\mathbf{r}), u_y(\mathbf{r}))$  such that un-displaced positions  $\mathbf{r} - \bar{u}(\mathbf{r})$  would form a perfect lattice. The topography then takes the form:

$$T(\mathbf{r}) = T_0 [\cos(\mathbf{Q}_x \cdot (\mathbf{r} - \bar{u}(\mathbf{r}))) + \cos(\mathbf{Q}_y \cdot (\mathbf{r} - \bar{u}(\mathbf{r})))] + T_{sup} [\cos(\mathbf{Q}_{sup} \cdot (\mathbf{r} - \bar{u}(\mathbf{r})))] + \varepsilon \quad (2.12)$$

where  $\varepsilon$  are extra contributions due to impurities, etc. The fact that  $\bar{u}(\mathbf{r})$  is slowly varying means nothing more than the local disturbance that causes to the lattice is small compared to the size of the lattice and the pixel resolution, i.e. that the Bragg peaks in the Fourier transform are well defined. Thus we can find a certain scale  $1/\Lambda$  such that  $\Lambda \ll |\mathbf{Q}_{x,y}|, |\mathbf{Q}_{sup}|$  over which  $\bar{u}(\mathbf{r})$  is roughly constant. From this, we can define:

$$T_{x,y}(\mathbf{r}) = \sum_{\mathbf{r}'} T(\mathbf{r}') e^{-i\mathbf{Q}_{x,y} \cdot \mathbf{r}'} \left( \frac{\Lambda}{2\pi} e^{-\frac{\Lambda^2 |\mathbf{r} - \mathbf{r}'|}{2}} \right) \approx \frac{1}{2} T_0 e^{-i\mathbf{Q}_{x,y} \cdot \bar{u}(\mathbf{r})} \quad (2.13)$$

where we made use of the fact that  $\bar{u}(\mathbf{r}) \approx \bar{u}(\mathbf{r}')$  within inside of  $\Lambda$ . From these expressions we can directly extract the displacement field  $\bar{u}(\mathbf{r})$ . Then, the strain tensor  $\sigma$  can be calculated from the displacement vector field as follows:

$$\sigma = \begin{pmatrix} \sigma_{xx} & \sigma_{xy} \\ \sigma_{yx} & \sigma_{yy} \end{pmatrix} = \begin{pmatrix} \frac{\partial u_x(\mathbf{r})}{\partial x} & \frac{\partial u_y(\mathbf{r})}{\partial x} \\ \frac{\partial u_x(\mathbf{r})}{\partial y} & \frac{\partial u_y(\mathbf{r})}{\partial y} \end{pmatrix} \quad (2.14)$$

In our images, we are usually concerned about the biaxial strain component  $\sigma_b = \frac{1}{2}(\sigma_{xx} + \sigma_{yy})$ , i.e. an overall increase (positive) or decrease (negative) in the unit cell surface, which is the bidimensional equivalent to hydrostatic pressure. We show in Fig. 2.22(a,b) the measured topography and corresponding calculated strain map that I calculated with this algorithm in a URu<sub>2</sub>Si<sub>2</sub> sample, included in Ref. [133].

The partial derivatives get rid of any linear offset in the displacement field that might come from a steady drift and thus not be related to any intrinsic atomic displacement. However, these drifts may computationally manifest as  $\pm 2\pi$  phase slips when the accumulated displacement from the original point exceeds one unit cell. Also, this method is completely unaware of the vertical dimension of the image,

as it only considers in-plane displacements. We show this in Fig. 2.22(c,d), where we compare the obtained strain map in a vertically modulated topography and an in-plane modulated topography.

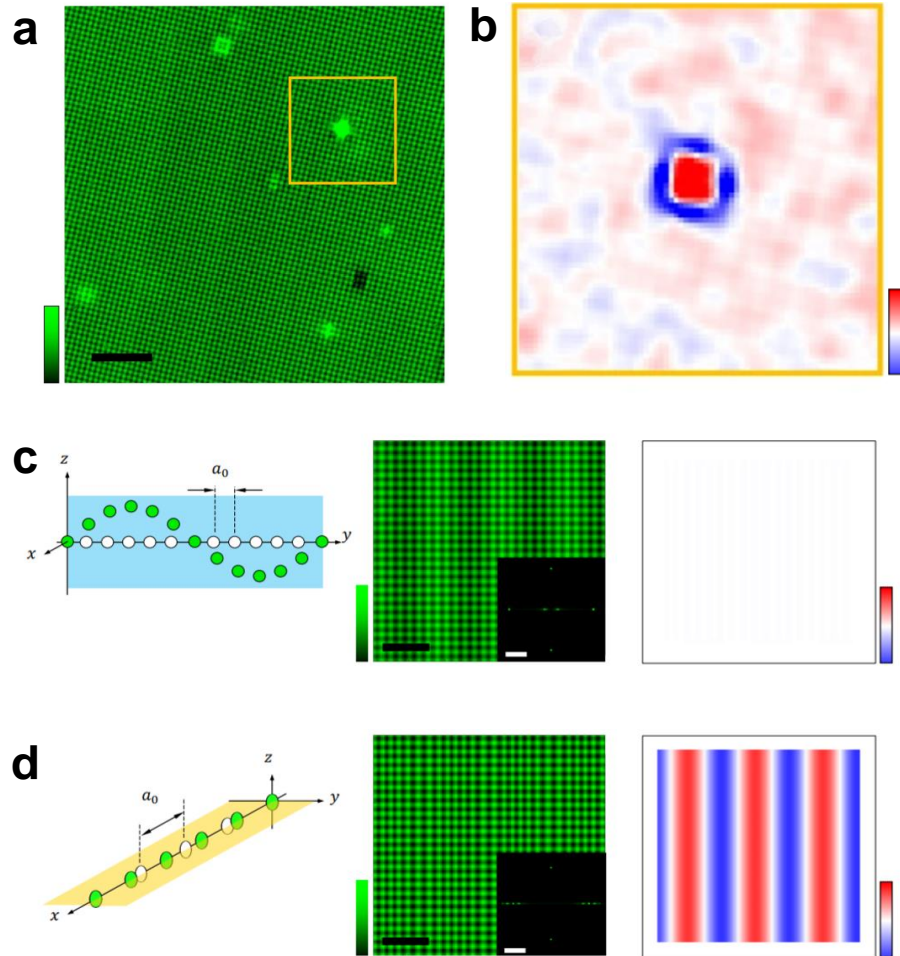


**Figure 2.22:** Adapted from Ref. [133]. (a) Topographic image of a U surface in  $\text{URu}_2\text{Si}_2$ . (b) In-plane strain map of the orange square marked in (a), calculated through the Lawler-Fujita algorithm. The color scale of the topography is shown in the bottom left part of (a) and ranges from 0 pm (black) to 20 pm (green). The strain scale is shown in the bottom right part of (b) and ranges  $\pm 5\%$  of the unit cell. Note how the defect locally induces a strong strain around it, even though there is no net overall strain. In (c,d) we show the schematic representation of a real space modulation for atomic displacements in a square atomic lattice. White circles show atomic positions without perturbation and green circles with a sinusoidal perturbation. In (c) the perturbation is along the  $c$  axis, out of plane, and in (d) we show a longitudinal modulation along the  $X$  axis. In each case we show the topography, its Fourier transform and its associated strain map, obtained as discussed in the text. Black scale bars are five times the lattice constant long. The color scale goes from zero (black) to one (green) in the topographies and from  $\pm 10\%$  the lattice constant.

# 3 | Superconductivity and quantum criticality: the $\text{BaFe}_2(\text{As}_{1-x}\text{P}_x)_2$ system

## 3.1 The $\text{BaFe}_2(\text{As}_{1-x}\text{P}_x)_2$ system

$\text{BaFe}_2\text{As}_2$  is considered the canonical representative of the 122 iron pnictide family with the  $I4/mmm$   $\text{ThCr}_2\text{Si}_2$ -type structure. It is not a superconductor and presents an antiferromagnetic and structural transition at  $T_N = 136$  K [134]. Like we show in Fig. 3.1, this transition is suppressed and a superconducting dome develops upon chemical doping, which can be either hole doping ( $\text{Ba}_{1-x}\text{K}_x\text{Fe}_2\text{As}_2$ ) [135, 136], electron doping ( $\text{Ba}(\text{Fe}_{1-x}\text{Co}_x)_2\text{As}_2$ ) [137] or even isovalent substitution ( $\text{BaFe}_2(\text{As}_{1-x}\text{P}_x)_2$ ) [138]. The latter has been extensively studied.

The  $\text{BaFe}_2(\text{As}_{1-x}\text{P}_x)_2$  system is one of the most remarkable examples of quantum criticality in an iron based superconductor. The isovalent substitution of As by P suppresses the stripe-like antiferromagnetic phase and induces superconductivity in a wide doping range from  $x=0.2$  to about  $x=0.7$ , with a maximum  $T_c$  of 30 K at the optimal doping  $x=0.3$  [139], where several experiments show [140] that there is a quantum critical point (QCP). Unlike most other doped systems, this isoelectronic substitution seems to introduce very little disorder to the lattice due to the similar atomic radius of As and P and great quality single crystals can be obtained throughout the entire doping series, specially in the overdoped regime [138, 141, 109].

Early transport and quantum oscillations measurements showed that the temperature dependence of the resistivity is linear in the normal state close to and above the optimal doping, which is a hallmark of a non-Fermi liquid [138, 141]. Moreover, specific heat and penetration depth measurements showed a diverging quasiparticle effective mass with largely enhanced electronic correlations [140, 142] which did not scale with the measured critical field [143], providing additional evidence for the existence of a QCP at optimal doping [144, 145]. Furthermore, there is recent evidence for strong nematic fluctuations at optimal doping, which are decoupled from the structural and magnetic transition, as confirmed by SQUID [146] and torque magnetometry [147], ultrafast optical measurements [148], ARPES [149], NMR [150] and Raman scattering [151].

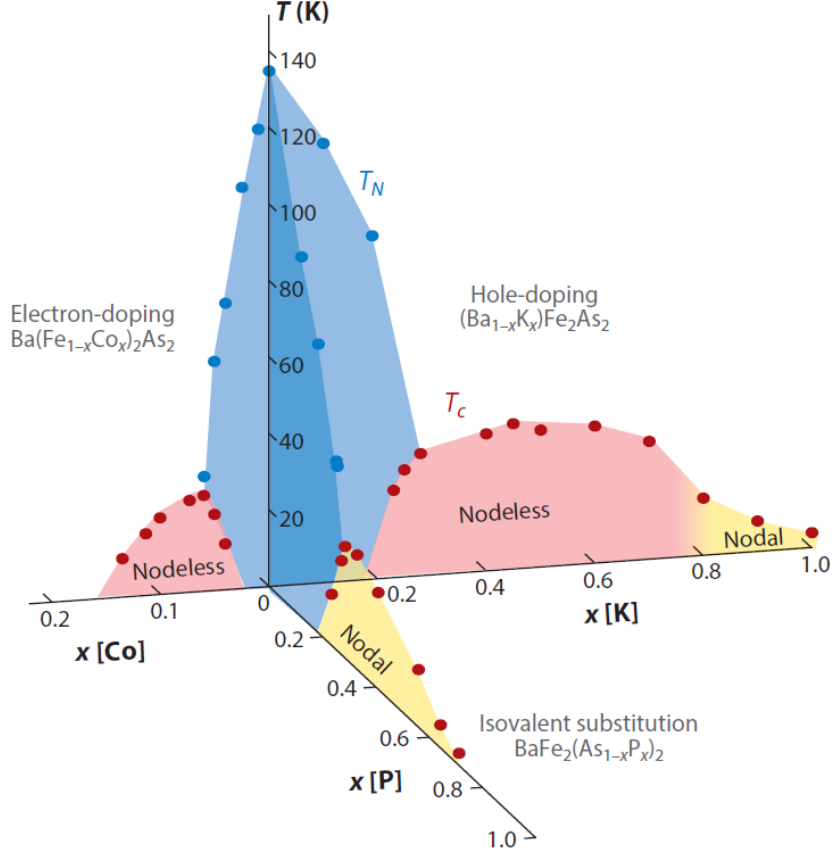


**Figure 3.1:** Extracted from Ref. [64]. Composite phase diagram of the  $\text{BaFe}_2\text{As}_2$  parent compound into the hole doped  $(\text{Ba}_{1-x}\text{K}_x)\text{Fe}_2\text{As}_2$ , the electron doped  $\text{Ba}(\text{Fe}_{1-x}\text{Co}_x)_2\text{As}_2$  and the isovalently substituted  $\text{BaFe}_2(\text{As}_{1-x}\text{P}_x)_2$ . Note that they all share common features like the suppression of the orthorhombic and magnetic phase (blue points) and the appearance of superconductivity (red points). The isovalently substituted  $\text{BaFe}_2(\text{As}_{1-x}\text{P}_x)_2$  reaches a maximum  $T_c$  of 30 K at around  $x = 0.3$

Substantial research in the last decade has orbited around determining the nature of the Fermi surface and the symmetry of the superconducting gap on entering the superconducting dome. The presence of line nodes is confirmed through thermal conductivity [152, 153] and ARPES measurements [154, 155, 156], however their precise shape and location is not agreed upon. The Fermi surface resembles that of most iron based superconductors: three cylindrical hole bands at the center of the Brillouin zone and two cylindrical electron bands at the corners. This is represented in detail in Fig. 3.3. However, it is not yet clear the exact role that the quantum criticality nor the Fermi surface and gap symmetry play in the enhancement of the superconductivity in this system.

Lastly, there are several works that address the vortex matter in  $\text{BaFe}_2(\text{As}_{1-x}\text{P}_x)_2$ . Bulk microwave cavity [152] and transport measurements [143] under field reveal an enhancement in the normal state energy at low temperatures. Some works have

visualized the vortex lattice through magnetic decoration techniques [157, 158, 159], but there are no studies of the vortex lattice at high magnetic fields whatsoever. In this Ph.D. thesis we used the extreme spatial and energy resolution of the STM at cryogenic temperatures to study  $\text{BaFe}_2(\text{As}_{1-x}\text{P}_x)_2$ .

Single crystals of  $\text{BaFe}_2(\text{As}_{1-x}\text{P}_x)_2$  were obtained by P. Walmsley and I. R. Fisher at Stanford University through a solution growth method described in subsection 2.3.3, which is explained in detail in Ref. [109].

### 3.2 STM in $\text{BaFe}_2(\text{As}_{0.7}\text{P}_{0.3})_2$ and $\text{BaFe}_2(\text{As}_{0.56}\text{P}_{0.44})_2$

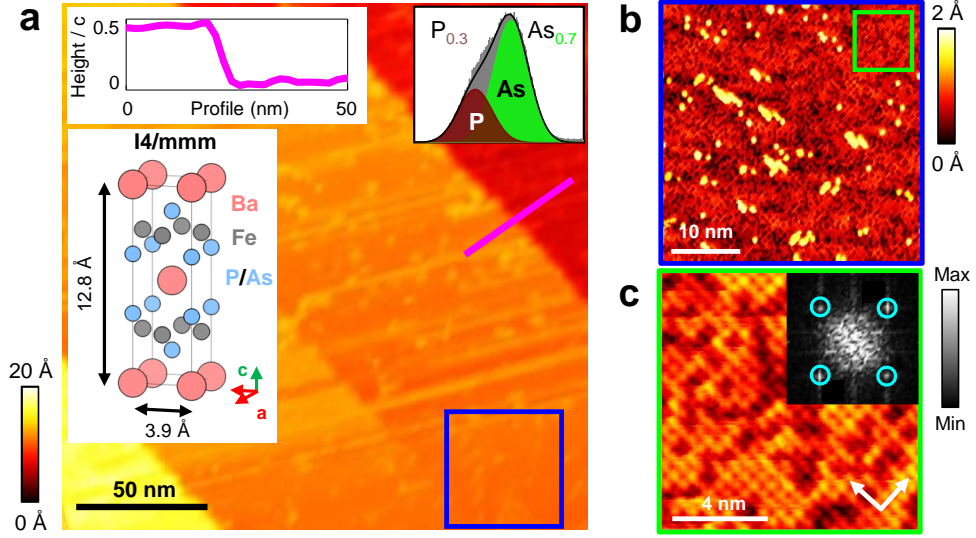


**Figure 3.2:** In (a) we show a large stepped region taken at 800 mK and zero field in the  $\text{BaFe}_2(\text{As}_{0.7}\text{P}_{0.3})_2$  sample. In the lower left inset, we plot the unit cell with its size and symmetry. In the upper left inset we show the height profile of the magnet line, showing that the steps of the large image on the left correspond to half a unit cell. When zooming in a flat area (b) marked by a blue square, we observe a square lattice of light and dark atoms (blue and green squares) decorated with very bright blobs. The interatomic distances match the expected unit cell size at 0.39 nm. In the upper right inset of (a), we plot the light/dark intensity histogram of the image in (b), which matches a 0.7/0.3 ratio and thus indicates that this is a As/P surface. In (c) we show a further zoom into the green area of (b). White arrows indicate the atomic directions. The inset shows the Fourier transform, with blue circles highlighting the atomic lattice Bragg peaks made by the As/P square lattice.

We see a topography image obtained in  $\text{BaFe}_2(\text{As}_{0.7}\text{P}_{0.3})_2$  in Fig. 3.2. We can see that there are large and flat areas, with terraces separated by steps that are half the  $c$ -axis unit cell height. Inside each terrace, we find clearly a square lattice, interspersed with bright blobs. The lattice consists of atomic size features whose

intensity varies. In particular, when we make a zoom inside the flat areas, we find the periodicity of the As/P lattice. By making a color histogram, we see that the number of dark spots is of about 30% and the number of bright spots about 70% of the overall histogram. From this, we can conclude that dark spots are P atoms and bright spots As atoms. We observed also clean atomically flat surfaces of Ba both in  $\text{BaFe}_2(\text{As}_{0.7}\text{P}_{0.3})_2$  and  $\text{BaFe}_2(\text{As}_{0.56}\text{P}_{0.44})_2$ .

### 3.2.1 Fermi surface

The Fermi surface in the  $\text{BaFe}_2(\text{As}_{1-x}\text{P}_x)_2$  system is similar to that of most iron pnictides. Quantum oscillations [109, 141] and ARPES [155] measurements, as well as DFT calculations [160] have confirmed that it is composed of three cylindrical hole bands centered around the  $\Gamma$  point and two more cylindrical electron bands centered around the M point. Similarly to previous works [154, 153, 155, 160], we will use the folded Brillouin zone of the 2 Fe unit cell in our representations for simplicity. In all the results we will show in this Ph.D. thesis, the Ba and As/P atomic lattices lay in the  $\Gamma\text{M}$  direction, while the Fe lattice follows the  $\Gamma\text{X}$  direction.

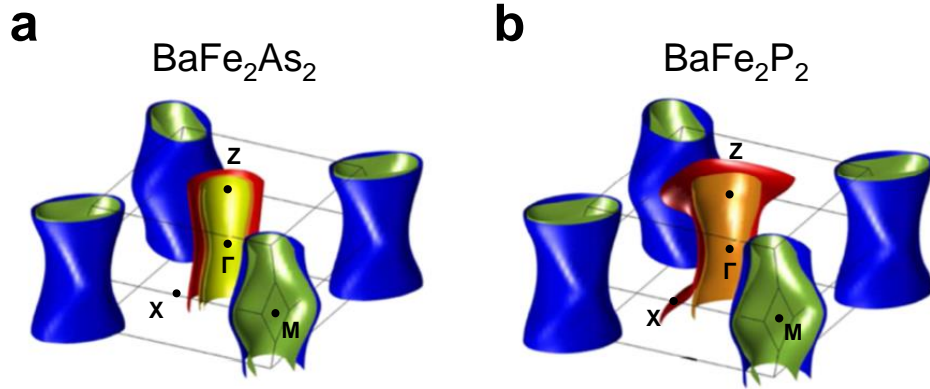


**Figure 3.3:** Adapted from Ref. [154]. We show the 3D representation of the Fermi surface of the two ends of the doping series,  $\text{BaFe}_2\text{As}_2$  (a) and  $\text{BaFe}_2\text{P}_2$  (b). Note that upon P doping, the inner hole band disappears and the outer hole band heavily warps around Z. We also marked here the high symmetry points for reference.

As we show in Fig. 3.3(a) and (b), increasing the P content from the parent compound  $\text{BaFe}_2\text{As}_2$  all the way to  $\text{BaFe}_2\text{P}_2$  has practically no effect on the electron sheets, while it causes the inner hole band to disappear and the outer hole band to warp and acquire a stronger 3D character. We can thus expect the Fermi surface of  $\text{BaFe}_2(\text{As}_{0.7}\text{P}_{0.3})_2$  and  $\text{BaFe}_2(\text{As}_{0.56}\text{P}_{0.44})_2$  to lay somewhere in between. The divergence of the effective mass in the normal state and the non-Fermi liquid behavior close to the QCP can't be predicted from the bare DFT calculated band structure, indicating a strong influence of enhanced electronic correlations.

### 3.2.2 Nodal superconducting gap

In Fig. 3.4 we show the tunneling conductance obtained on the  $\text{BaFe}_2(\text{As}_{0.7}\text{P}_{0.3})_2$  (red) and  $\text{BaFe}_2(\text{As}_{0.56}\text{P}_{0.44})_2$  (blue) samples we have measured. We see that the tunneling density of states is quite similar, and has strongly depressed quasiparticle peaks (as compared to an  $s$ -wave BCS conventional superconductor, see Fig. 1.6(a)) and a tunneling conductance that is quite large for voltages below the quasiparticle peak positions.

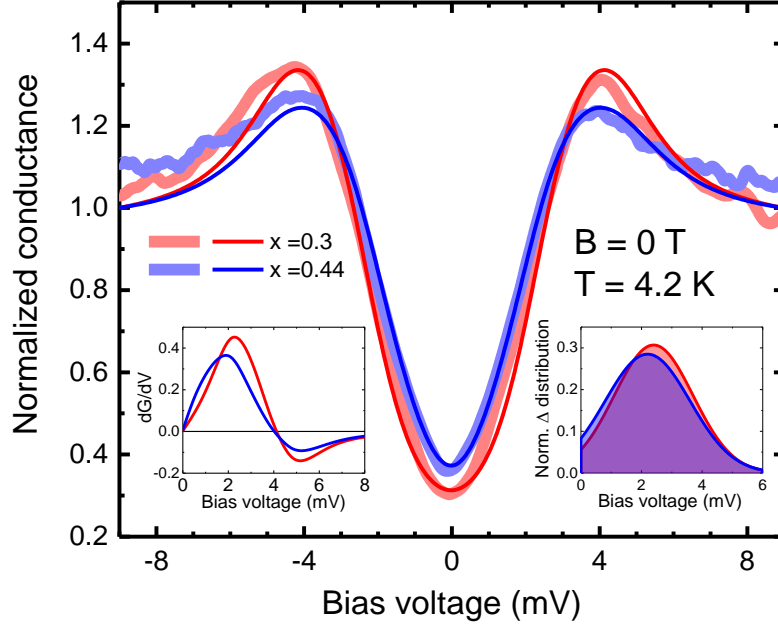


**Figure 3.4:** We show the superconducting gap structure at 4.2 K and zero field of  $\text{BaFe}_2(\text{As}_{0.7}\text{P}_{0.3})_2$  (light red) and  $\text{BaFe}_2(\text{As}_{0.56}\text{P}_{0.44})_2$  (light blue). For each curve, we have fitted the observed DOS to a distribution of BCS gaps, and plot the results in a darker tone of red ( $\text{BaFe}_2(\text{As}_{0.7}\text{P}_{0.3})_2$ ) and blue ( $\text{BaFe}_2(\text{As}_{0.56}\text{P}_{0.44})_2$ ). This distribution of gaps is shown in the right inset, where we observe that the  $\text{BaFe}_2(\text{As}_{0.56}\text{P}_{0.44})_2$  curve has a stronger contribution of smaller gaps, consistent with its lower  $T_c$ . The left inset shows the derivative of the fitted gap curves, confirming that although the quasiparticle peak (i.e. the zeros in the derivative) practically coincide, the inflection point of the  $\text{BaFe}_2(\text{As}_{0.56}\text{P}_{0.44})_2$  curve (i.e. the maximum of the derivative) is shifted to lower bias voltages.

We see in particular that the superconducting density of states is quite large at zero bias, indicating the presence of many low energy excitations. To understand these curves, we use the expression described in Equation 1.15. The tunneling conductance is compared to a certain distribution of values of the superconducting gap. The obtained distribution is shown as a the lower right inset in Fig. 3.4. We see that the distribution has one clear peak. The peak provides an average value of the superconducting gap. For  $\text{BaFe}_2(\text{As}_{0.7}\text{P}_{0.3})_2$  we find 2.5 mV, which taking Equation 1.13 corresponds to  $T_c=30$  K, and for  $\text{BaFe}_2(\text{As}_{0.56}\text{P}_{0.44})_2$  we find 2 mV,

which corresponds to  $T_c=23$  K. Furthermore, we also observe that the zero bias tunneling conductance is smaller in  $\text{BaFe}_2(\text{As}_{0.7}\text{P}_{0.3})_2$  than in  $\text{BaFe}_2(\text{As}_{0.56}\text{P}_{0.44})_2$ .

Such a smeared superconducting density of states, with many states inside the superconducting gap, is in agreement with measurements of the superconducting gap anisotropy using macroscopic probes [152]. There is a generic agreement that there are accidental line nodes in the Fermi surface. Their location and shape is however controverted. These nodes stem from the crossing of elliptical bands with different signs in the Cooper pair wavefunction. As we show in Fig. 3.5, ARPES finds that the nodes are at the intersection between the outer hole band and the top and bottom of the Brillouin zone [153]. Other ARPES measurements locate the nodes around the bellies of the inner electron sheets [155]. Finally, thermal conductivity proposes instead a complex 3D pattern for the crossing of the bands which leads to loop nodes in the flattest parts of the outer electron shells as schematically shown in Fig. 3.5(c) [154].

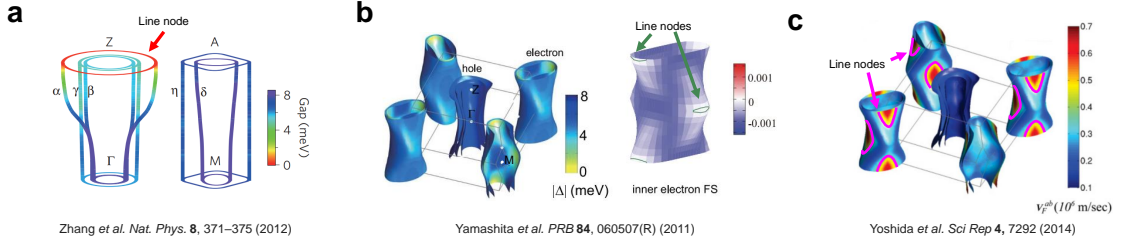


**Figure 3.5:** (a) Adapted from Ref. [153]. Line nodes are at the intersection of the Z plane and the outer hole bands. (b) Adapted from Ref. [155]. Nodal loops are around the sharpest parts of the inner electron bands. (c) Adapted from Ref. [154]. Nodal loops are around the flattest parts of the outer electron bands. Note that all these works consider the optimal doping  $\text{BaFe}_2(\text{As}_{0.7}\text{P}_{0.3})_2$ .

Our tunneling density of states measurements are compatible with all these proposals. A more detailed angular dependent study can be made by taking a careful look on the vortices and on the band structure.

### 3.2.3 Vortex lattice

We measured the vortex lattice below 4.2 K in both samples for several magnetic fields up to 7 T. Even at the highest fields, we were relatively far from the critical field. In the optimally doped sample,  $H_{c2} \approx 50$  T so 7 T is around 15% of  $H_{c2}$ . In the overdoped sample the critical field is  $H_{c2} \approx 20$  T. In this case, 7 T is around 30% of  $H_{c2}$ . We show in Fig. 3.6 some relevant vortex lattice images obtained over large atomically flat surfaces in the optimally doped sample (Fig. 3.6(a)) and the overdoped sample (Fig. 3.6(b)). The vortex center was found using a custom software [122] based in Delaunay triangulation, and is indicated with a black dot.

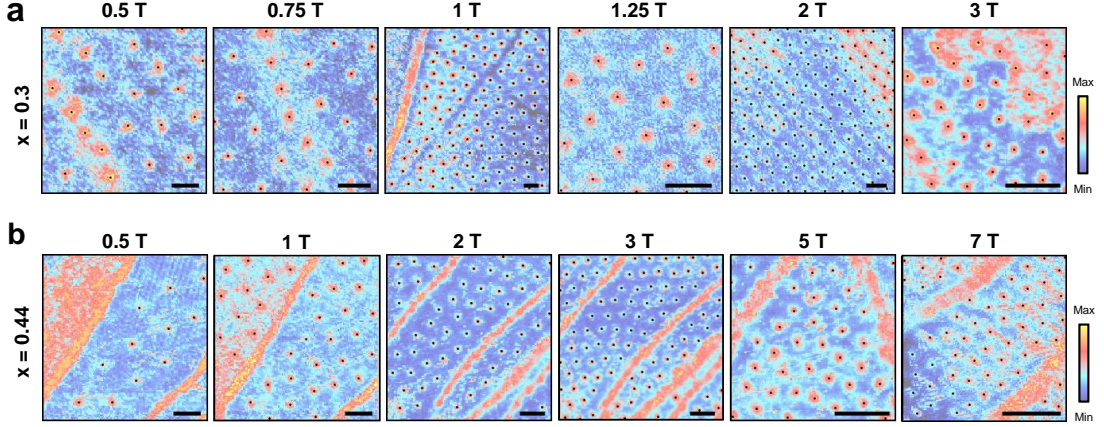


**Figure 3.6:** Zero bias conductance maps at different applied magnetic fields in the  $\text{BaFe}_2(\text{As}_{0.7}\text{P}_{0.3})_2$  (a) and  $\text{BaFe}_2(\text{As}_{0.56}\text{P}_{0.44})_2$  (b) samples. The center of each vortex is indicated with a black dot. Black scale bars are 50 nm long. The relation between the color scale and the tunneling conductance is adjusted in each image to provide for maximum clarity in the observation of the vortex lattice.

The density of vortices with magnetic field is shown in Fig. 3.7 and matches the expectation for the Abrikosov hexagonal lattice (green line), although the expected intervortex distances for a square vortex lattice are also within the error bars.

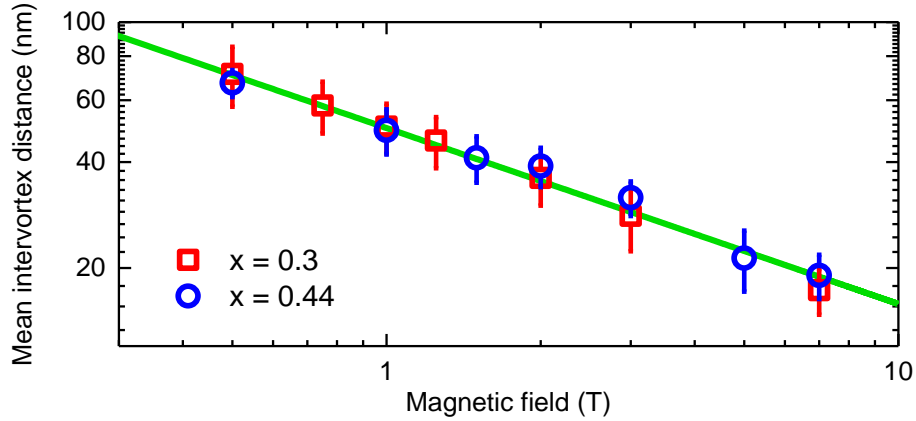


**Figure 3.7:** Average intervortex distance, calculated from the triangulated vortex positions in  $\text{BaFe}_2(\text{As}_{0.7}\text{P}_{0.3})_2$  (red squares) and  $\text{BaFe}_2(\text{As}_{0.56}\text{P}_{0.44})_2$  (blue circles). The expected intervortex distance for the hexagonal Abrikosov lattice is shown as a green line.

The most remarkable result of these images is that the vortex lattice is highly ordered, in particular when compared to similar compounds as  $\text{Ba}_{0.6}\text{K}_{0.4}\text{Fe}_2\text{As}_2$  [161],  $\text{Ca}(\text{Fe}_{0.97}\text{Co}_{0.03})_2\text{As}_2$  [162] or  $\text{CaKFe}_4\text{As}_4$  [37]. We can make a Fourier analysis of the triangulated vortex positions (Fig. 3.8). From the Fourier analysis, we identify a clear tendency to form a square vortex lattice in  $\text{BaFe}_2(\text{As}_{0.7}\text{P}_{0.3})_2$  locked to the

crystal lattice. In  $\text{BaFe}_2(\text{As}_{0.56}\text{P}_{0.44})_2$ , we rather observe a hexagonal lattice with one axis also aligned to the atomic lattice.

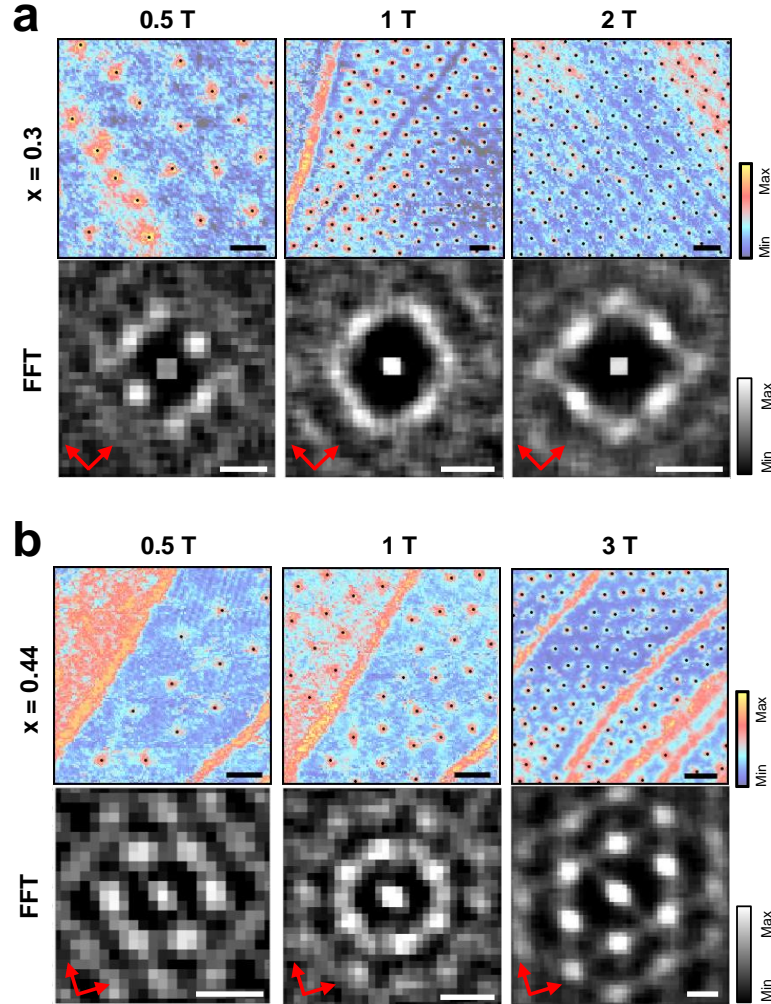


**Figure 3.8:** Zero bias conductance maps (upper panels) and FFTs of the triangulated vortex positions (lower panels) at different applied magnetic fields in the  $\text{BaFe}_2(\text{As}_{0.7}\text{P}_{0.3})_2$  (a) and  $\text{BaFe}_2(\text{As}_{0.56}\text{P}_{0.44})_2$  (b) samples. The center of each vortex is indicated with a black dot. Black scale bars are 50 nm long. White scale bars are 0.02 nm<sup>-1</sup> long. The contrast is adjusted in each image to maximize the vortices and features. The atomic directions are marked with red arrows.

This tendency is visible over a wide range of magnetic fields, suggesting that the square vortex lattice is related to the quantum critical properties of  $\text{BaFe}_2(\text{As}_{0.7}\text{P}_{0.3})_2$ . We can further explore this finding by calculating the mean angle between the two closest vortex lattice Bragg peaks at each magnetic field. We show the result in Fig. 3.9, where we find a very strong indication for a square lattice in  $\text{BaFe}_2(\text{As}_{0.7}\text{P}_{0.3})_2$ .

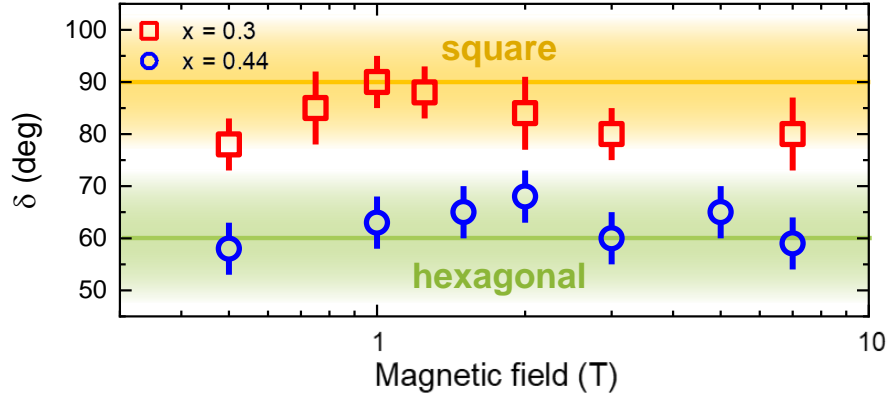


**Figure 3.9:** We plot the angle  $\delta$  between the two brightest consecutive spots in the FFT of the triangulated vortex positions, showing that vortices tend to arrange forming a square lattice in  $\text{BaFe}_2(\text{As}_{0.7}\text{P}_{0.3})_2$  (yellow line and shadow) while in  $\text{BaFe}_2(\text{As}_{0.56}\text{P}_{0.44})_2$  the lattice is hexagonal (green line and shadow).

### 3.2.4 Vortex cores at the quantum critical point

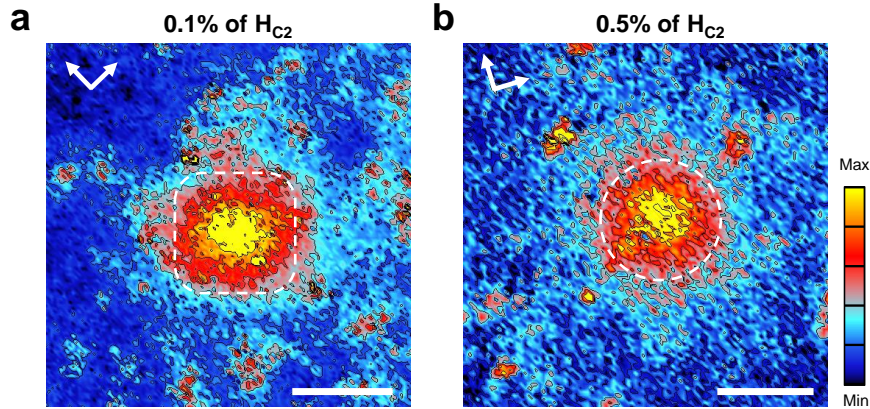


**Figure 3.10:** We show as a color scale the tunneling conductance vs position at 0.05 T (0.1% of  $H_{c2}$ ) in  $\text{BaFe}_2(\text{As}_{0.7}\text{P}_{0.3})_2$  (a) and at 0.2 T (0.5% of  $H_{c2}$ ) in  $\text{BaFe}_2(\text{As}_{0.56}\text{P}_{0.44})_2$  (b). Arrows mark the atomic in-plane atomic lattice. White dashed lines are added as a guide to the eye. White scale bars are 10 nm long.

A square vortex lattice can be an indicator of some tetragonal anisotropy in the Fermi surface, which might affect the vortex core shape too [19, 163, 164, 165, 20]. We show in Fig. 3.10 a high resolution comparison of a typical vortex core at low fields in  $\text{BaFe}_2(\text{As}_{0.7}\text{P}_{0.3})_2$  (Fig. 3.10(a)) and  $\text{BaFe}_2(\text{As}_{0.56}\text{P}_{0.44})_2$  (Fig. 3.10(b)). We highlight the vortex core with a white dashed line. We do observe a certain square component in the optimally doped sample, which tends to align the corners of the square with the atomic lattice, marked with white arrows. In contrast, the vortex core in the overdoped sample is round.

## 3.2.5 Vortex core size vs magnetic field

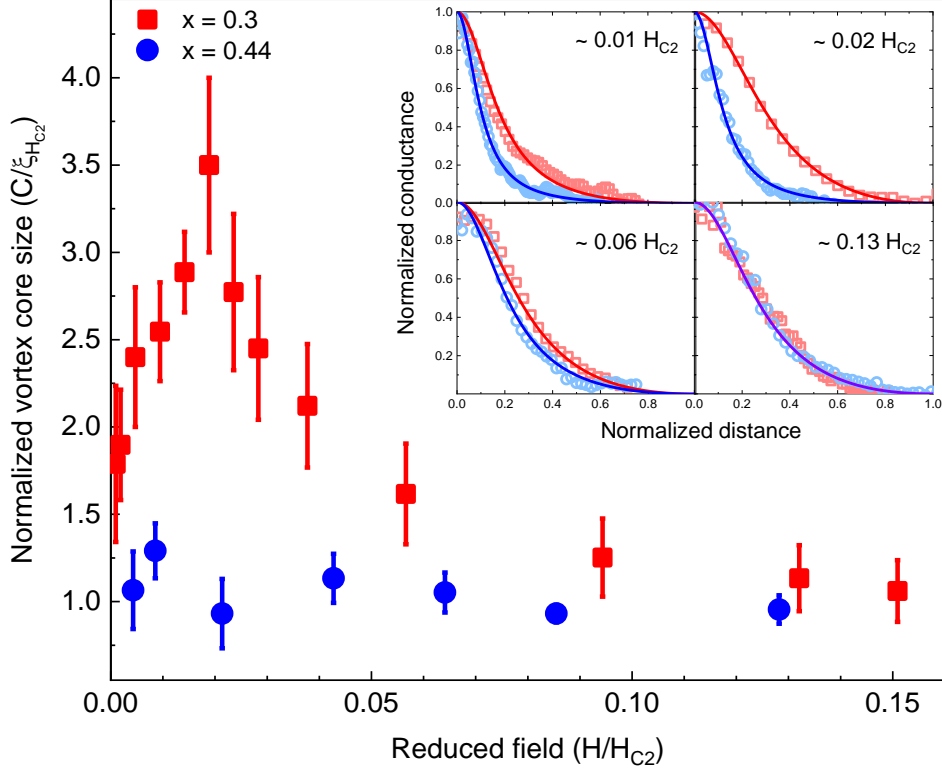


**Figure 3.11:** We show as red squares ( $\text{BaFe}_2(\text{As}_{0.7}\text{P}_{0.3})_2$ ) and blue dots ( $\text{BaFe}_2(\text{As}_{0.56}\text{P}_{0.44})_2$ ) the normalized vortex core size as a function of the normalized magnetic field. Estimated error bars are also provided. The field is normalized to the upper critical field in each compound. Using the value of  $H_{c2}$ , we obtain  $\xi_{H_{c2}}$ . The vortex core size is normalized to  $\xi_{H_{c2}}$  in each compound. In the inset we show as red squares ( $\text{BaFe}_2(\text{As}_{0.7}\text{P}_{0.3})_2$ ) and blue circles ( $\text{BaFe}_2(\text{As}_{0.56}\text{P}_{0.44})_2$ ) the normalized conductance as a function of the radius with respect to the center of the vortex for different values of the magnetic field. The radius is normalized to the intervortex distance, following Equation 1.19. The data are fitted to Equation 1.21 from which we can extract the core size values  $C$  that are depicted in the bigger graph.

We now analyze the spatial dependence of the density of states from the center of a vortex core outwards. We see already from Fig. 3.10 that the tunneling conductance has a weaker dependence as a function of the distance in  $\text{BaFe}_2(\text{As}_{0.7}\text{P}_{0.3})_2$  than in  $\text{BaFe}_2(\text{As}_{0.56}\text{P}_{0.44})_2$ . In particular, the yellow colored part close to the vortex center is larger in  $\text{BaFe}_2(\text{As}_{0.7}\text{P}_{0.3})_2$ . To analyze this further, we have taken images of isolated vortices at several magnetic fields in each compound. Following Equation 1.21, we have plotted the tunneling conductance normalized to its value at the center of the vortex and in between vortices for different magnetic fields. From the radial dependence of the tunneling conductance we extract the vortex core size  $C$ . To compare results in both compounds, we normalize the magnetic field to the respective critical fields and  $C$  to the superconducting coherence length (obtained

from Equation 1.19 and the critical field values of Ref. [143]).

We observe that  $C$  is independent of the magnetic field in  $\text{BaFe}_2(\text{As}_{0.56}\text{P}_{0.44})_2$ , very similarly to what was observed in  $2\text{H-NbSe}_{1.8}\text{S}_{0.2}$  (see Fig. 1.10(d) and Ref. [34]). However, in  $\text{BaFe}_2(\text{As}_{0.7}\text{P}_{0.3})_2$  we observe a completely different field dependence. We see that the vortex core size first considerably increases with the magnetic field, reaches a peak at approximately 2% of  $H_{c2}$  and then decreases again. This anomalous dependence of the vortex core size should be related to the quantum critical properties of  $\text{BaFe}_2(\text{As}_{0.7}\text{P}_{0.3})_2$ .

### 3.2.6 Vortex cores in the quantum limit

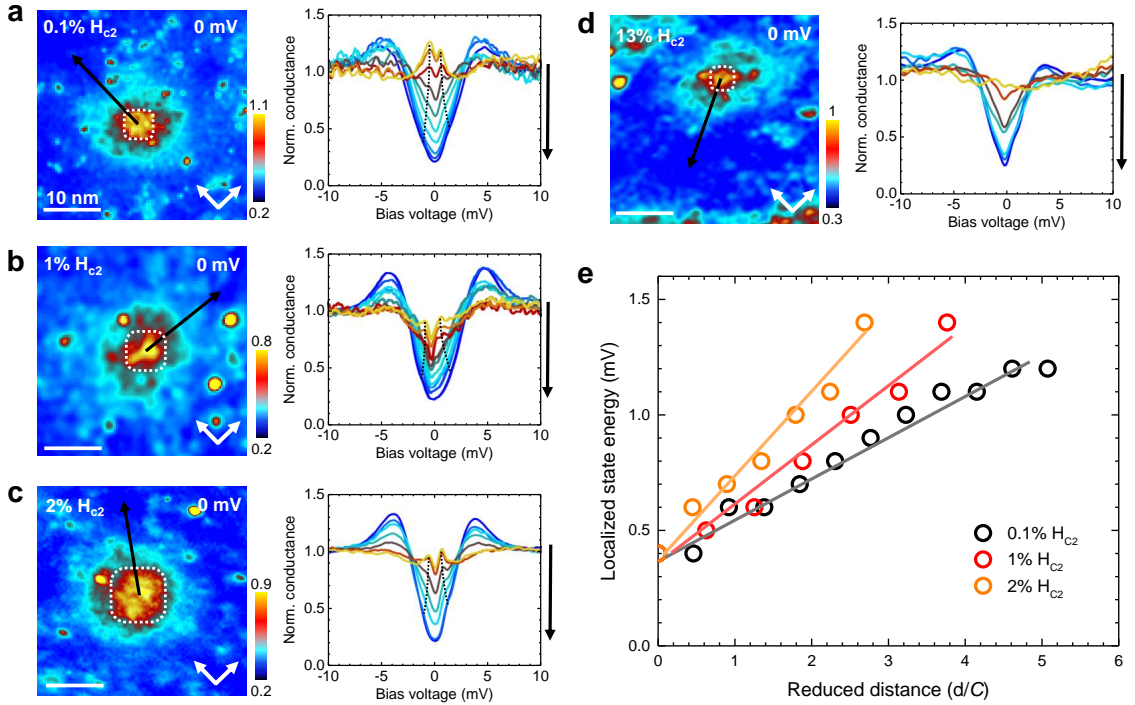


**Figure 3.12:** In the left panels of (a-d) we plot the zero bias conductance as a function of the position in  $\text{BaFe}_2(\text{As}_{0.7}\text{P}_{0.3})_2$  at different magnetic fields, indicated in the upper left corner. Black arrows provide the path which we follow to trace the full tunneling conductance curves vs bias voltage shown in the right panels. We provide the vortex core size as a white dashed line and the atomic lattice directions with white arrows for reference. The white scale bar is 10 nm long. The color scale of the curves provides the approximate position of each curve (comparing to the color scale of the left panels). We mark in the right panels with black dashed lines the position dependence of the peak in the tunneling conductance observed close to the vortex center. In (e) we plot the energy of this peak vs position. In the quantum limit, we expect a peak at an energy which is independent of the position.

We now focus on the vortex core states in  $\text{BaFe}_2(\text{As}_{0.7}\text{P}_{0.3})_2$ . We observe two low bias peaks with small zero bias gap in all the vortices at low fields. This feature is

present up to 2% of  $H_{c2}$ , where the vortex core states are less visible in the tunneling conductance, probably due to overlap with other vortices. In Fig. 3.12(a-c) we show the zero bias conductance maps of vortices at low fields with an energy profile from the center outwards, where we see this prominent feature in the center of each core. At higher fields we no longer see clear core states (Fig. 3.12(d)).

In vortices of most superconductors, usually a single zero bias peak is measured at its center, which is the result of the contribution of many states [26]. The so-called quantum limit is obtained for temperatures  $T/T_c \leq 1/k_F\xi_0$  [29, 32]. Taking  $\xi_0$  of 2.6 nm (obtained from  $H_{c2}$ , see Ref. [143]), and  $k_F \approx 4 \text{ nm}^{-1}$ , which is approximately half of the Brillouin zone, as shown below, we find  $T/T_c \approx 0.13$ , or  $T \approx 4 \text{ K}$ . It also provides a lowest lying state of 0.4 meV, which is above the thermal smearing at 4 K. In the quantum limit, we expect a peak in the density of states at the lowest lying state energy which should not to vary as a function of the position [29, 167]. Out of the quantum limit, there is instead a zero bias peak which splits and moves to higher energies when leaving the vortex center [26, 14]. We indeed observe that the peak in the density of states has a weak dependence with position at the lowest magnetic fields. This suggests that the vortices in  $\text{BaFe}_2(\text{As}_{0.7}\text{P}_{0.3})_2$  are in the quantum limit at very low magnetic fields and that the quantum limit is lost due to vortex overlap when increasing the magnetic field.

The model of Kogan and Zhelezina [33] is not valid in the quantum limit, because it assumes that there is a straightforward relationship between the zero bias density of states and the gap magnitude, which is lost in the quantum limit. Thus, we can understand the apparent increase in the vortex core size (see Fig. 3.11) as a consequence of approaching, at low magnetic fields, the quantum limit.

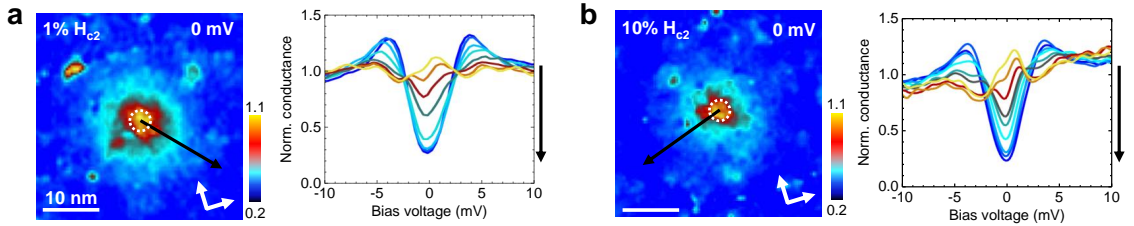


**Figure 3.13:** In the left panels of (a) and (b) we plot the zero bias conductance as a function of the position in  $\text{BaFe}_2(\text{As}_{0.56}\text{P}_{0.44})_2$  at different magnetic fields, indicated in the upper left corner. Black arrows provide the path which we follow to trace the full tunneling conductance curves vs bias voltage shown in the right panels. We provide the vortex core size as a white dashed line and the atomic lattice directions with white arrows for reference. The white scale bar is 10 nm long. The color scale of the curves provides the approximate position of each curve (comparing to the color scale of the left panels).

In  $\text{BaFe}_2(\text{As}_{0.56}\text{P}_{0.44})_2$  we observe a much more conventional behavior of the vortex core states, similar to  $2\text{H-NbSe}_2$  [26]. We observe a single central peak at the vortex center which splits and moves in energy together with the position, when leaving the vortex center. Two representative results are shown in Fig. 3.13.

## 3.3 Quasiparticle interference measurements

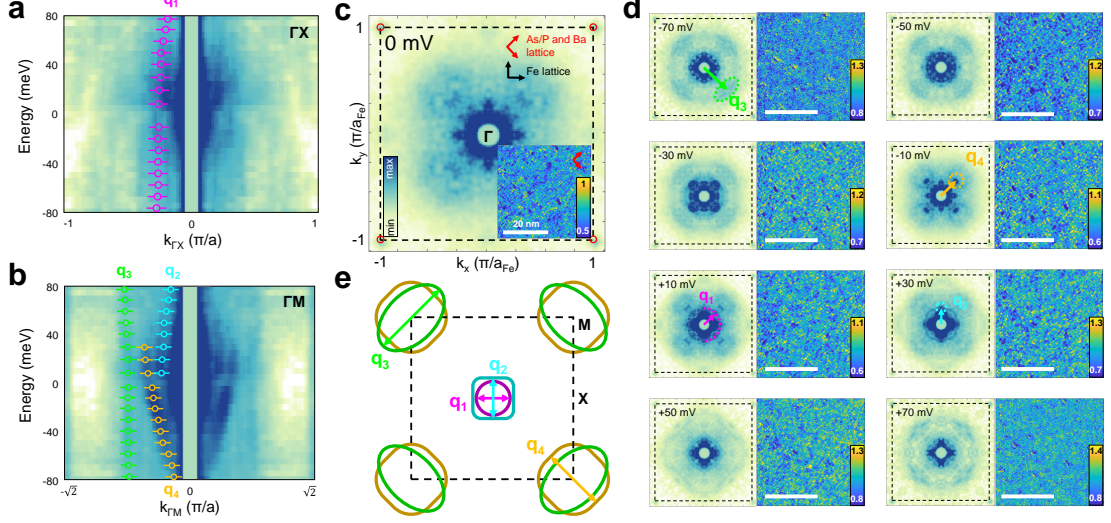


**Figure 3.14:** In (a) we show the Fourier transform of the intensity along the  $\Gamma X$  direction and in (b) along the  $\Gamma M$  direction as a function of the energy, obtained at zero magnetic field. Band dispersion relations are highlighted by dots, with error bars discussed in the text. The relevant  $q$ -vectors are labelled from  $q_1$  to  $q_4$ . In (c) we show the Fourier transform of the tunneling conductance within the first Brillouin zone of the Fe atomic lattice, marked by black dashed lines, at zero energy. The Bragg peaks of the As/P lattice are marked with red circles. The lattice directions are marked by colored arrows. In (e) we show schematically the band structure of  $\text{BaFe}_2(\text{As}_{0.7}\text{P}_{0.3})_2$ . Bands are shown by colored lines, with the first Brillouin zone of the Fe lattice marked by black dashed lines. Arrows mark the scattering vectors we identify in our experiment. These are shown in (d), where we plot the Fourier transform (left panels) and the real space conductance maps (right panels). Note that the first Brillouin zone of the Fe lattice is also marked by black dashed lines in the FFTs. White scale bars are 20 nm long. We highlight by arrows the main scattering vectors.

A more comprehensive understanding of the influence of quantum criticality in the superconducting properties can be obtained when studying in detail the tunneling conductance maps obtained in  $\text{BaFe}_2(\text{As}_{0.7}\text{P}_{0.3})_2$ . We performed spectroscopic measurements at zero field and 800 mK in the atomically flat region shown in the upper right panel of Fig. 3.2. We show the main results in Fig. 3.14. Note that the studied As/P surface is decorated with very bright blobs corresponding to surface impurities or Ba adatoms. These spots dominate the conductance intensity and obscure the underlying surface signal, so we have minimized their effect by neglecting any wave vector smaller than the average interimpurity distance, in reciprocal space.

In Fig. 3.14 we show the result of our experiments. We identify scattering from the hole pockets centered around  $\Gamma$  ( $q_1$  and  $q_2$ ). Both have a slight dispersion with energy, compatible with an effective mass of around  $2 m_e$  for  $q_1$  and  $3 m_e$  for  $q_2$ . This

is in line with previously reported effective masses for the hole bands measured with ARPES (Table I in Ref. [168]). Furthermore, we observe a ring-like scattering for  $q_1$ , which suggests that the underlying band is circular or quasi-circular. For  $q_2$ , we observe scattering at four Bragg spots, suggesting that the band has flat portions. We also identify electron-like scattering in the outer bands. We can see that  $q_3$  joins diagonal sections of the inner electron band, with a dispersion too narrow to calculate an effective mass.  $q_3$  is rather spread out in reciprocal space, although there is a certain directional dependence. This suggests that there are portions of the band structure with different dispersion relations, favoring scattering along certain directions. An interesting scattering vector is  $q_4$ . Here we identify scattering that is electron-like and has four clear Bragg peaks, with an effective mass of around  $9 m_e$ . Previous specific heat and dHvA measurements situated the effective mass of the electron bands at around  $10 m_e$  (Fig.5 in Ref. [142]). We can associate this to scattering between flat portions of the outer electron band, as schematically shown by the orange arrow in Fig. 3.14(e). While there are indications for gap opening in all bands Fig. 3.14(a,b), the most visible difference at energies below the superconducting gap occurs in the  $q_4$  scattering vector.

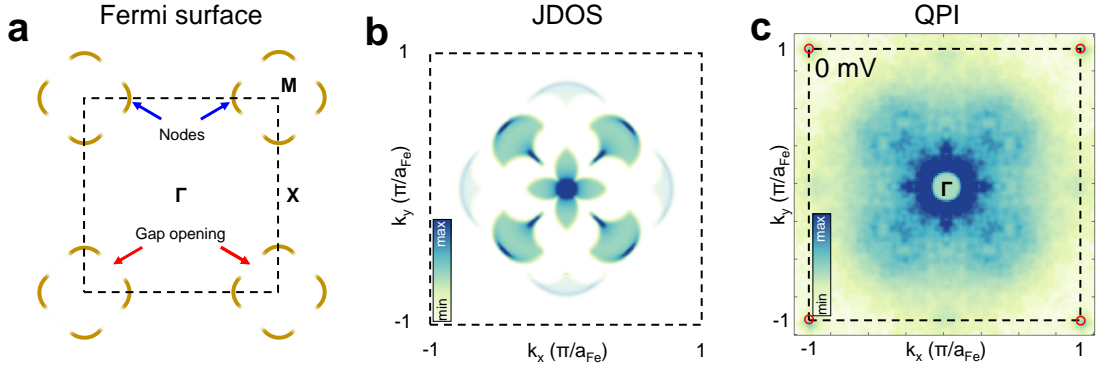


**Figure 3.15:** (a) Sketch of the gapped Fermi surface, only including the outer electron band associated with  $q_4$ . In it, we mark the gap openings as well as the nodal regions. (b) Calculated JDOS of the Fermi surface shown in (a). (c) QPI intensity pattern obtained in the experiment at 0 mV, with the color scale adjusted to highlight the main features. The four petal structure corresponds to intraband scattering. Note that in (a-c) the first Brillouin zone of the Fe lattice is marked by black dashed lines.

We can analyze this in more detail by seeking for Fermi surfaces that can lead to the pattern we observe in the figure Fig. 3.14(c), related to the  $q_4$  wave vector. The result is shown in Fig. 3.15, where we calculate the JDOS of the outer electron bands. We see in particular that in order to produce the pattern observed in the experiment, the round square shaped outer electron band has a gap open along the  $\Gamma\text{M}$  directions, which coincide with the As/P lattice directions. Along the  $\Gamma\text{X}$  directions the gap is closed, suggesting that along the Fe lattice directions there are nodal points.

### 3.4 Conclusion

The  $\text{BaFe}_2(\text{As}_{1-x}\text{P}_x)_2$  system is particularly well suited to study the interplay between unconventional superconductivity and quantum criticality. We performed the first microscopic approach to the problem with STM measurements of the LDOS at low temperatures in two samples,  $\text{BaFe}_2(\text{As}_{0.7}\text{P}_{0.3})_2$  at the QCP and  $\text{BaFe}_2(\text{As}_{0.56}\text{P}_{0.44})_2$  in the overdoped regime far from the antiferromagnetic transition. We found large atomically flat surfaces with similar topographic characteristics to other Ba based 122-type compounds, and a V-shaped superconducting gap which is consistent with nodal superconductivity.

We obtained the first images of the vortex lattice and found that it is well ordered at long ranges, which is uncommon for pnictide superconductors and reinforces the idea that the P substitution introduces very low disorder to the lattice. Moreover, we found a square vortex lattice and square vortex cores in  $\text{BaFe}_2(\text{As}_{0.7}\text{P}_{0.3})_2$ , as opposed to the round vortices and regular hexagonal lattice measured in  $\text{BaFe}_2(\text{As}_{0.56}\text{P}_{0.44})_2$ , indicating that the gap anisotropy and nodal character of the superconducting gap is stronger close to the QCP.

The field dependence of the vortex core size in  $\text{BaFe}_2(\text{As}_{0.56}\text{P}_{0.44})_2$  is that of a single band superconductor in the dirty limit with  $C \approx \xi_{H_{c2}}$  for the whole field range. However, we found a surprising field dependence of the vortex core size in  $\text{BaFe}_2(\text{As}_{0.7}\text{P}_{0.3})_2$ , which first raises from  $2\xi_{H_{c2}}$  to a maximum of  $3.5\xi_{H_{c2}}$  at 2% of  $H_{c2}$  before dropping to  $\xi_{H_{c2}}$  above 15% of  $H_{c2}$ . We associate this to the passage into the quantum limit, when the system is close to the quantum critical point and at very low magnetic fields.

Finally we performed spectroscopic measurements in  $\text{BaFe}_2(\text{As}_{0.7}\text{P}_{0.3})_2$ , and found several dispersive features in the QPI intensity which we could trace to different scattering events between Fermi sheets. From our study of electron scattering, we identify the direction of gap nodes and the size of the effective masses close to the quantum critical point.

# 4 | Feedback driven AC Josephson effect

There is a strong interest in superconductor science to measure not only the density of states of a superconductor but also the coupling between order parameters [169, 170, 171]. The Josephson current is proportional to this coupling and can be probed with atomic precision by using a superconducting tip in a STM setup at low temperatures [172]. This approach is however extremely challenging as the signal strength is largely decreased in the tunnel regime. Moreover, new phenomena might play a significant role under such conditions like the influence of the electromagnetic environment [173] or the spatial dependence of the Cooper pair density [174, 80]. In addition, as I will show below, there are yet some unexplained experimental results like the observed hysteretical behavior of the tunnel Josephson signal [175].

In this chapter I will present results of high resolution measurements of the Josephson current in Pb–Pb, Pb–NbSe<sub>2</sub> and Al–Al junctions made with the STM. I will in particular focus on the Pb–Pb junctions, where my measurements unveil a new oscillatory behavior that sets in above the critical current and is also present in Pb–NbSe<sub>2</sub> and Al–Al. We can understand this new AC Josephson behavior as a connection between the phase dynamics of the Josephson junction and the retarded feedback induced by the electric circuit connected to the junction.

## 4.1 Dynamic Josephson effect observed with STM

### 4.1.1 DC Josephson effect

As previously introduced in [section 1.4](#), the Josephson effect consists of a current flowing at zero bias between two superconducting electrodes. The current is, according to the first Josephson relation ([Equation 1.25](#)), due to the established phase difference between both electrodes. Careful studies of the Josephson effect at atomic scale [176, 177, 178, 174, 80] have shown that the Josephson current is strongly influenced by thermal fluctuations. This reduces the size of the zero bias current and induces a small but finite slope, which implies that thermal excitations produce a fluctuating phase between both electrodes when measured with a STM. As tip and sample separate (see [Fig. 4.1](#)), we observe that the slope and zero bias and the current at the peak both decrease. This shows that the maximum supercurrent flowing between both electrodes becomes smaller. This effect has been studied in

depth in Refs. [179, 177, 173, 180] and is due to thermal fluctuations and the influence of the environment. However, literature also shows that above the current peak, there is a voltage range with a shoulder plateau, as we also see (Fig. 4.1(b)) in our experiments.

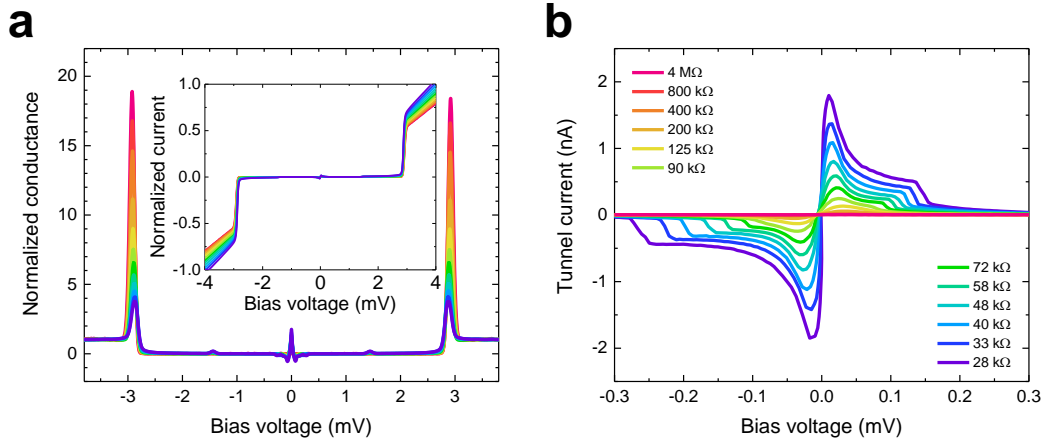


**Figure 4.1:** (a) The tunneling conductance vs bias voltage is plotted as colored lines. The tunneling current is shown in the inset. A zoom into the tunneling current vs bias is shown in (b). The bias voltage is ramped down. The color indicates the tunneling resistance of each curve, following the legend in (b).

This shoulder observed in Fig. 4.1(b) has been observed previously in several experiments [175, 181, 182]. It remained however without explanation. During the experiments I performed in this Ph.D. thesis, I observed a time dependent tunneling current in the bias voltage range where the shoulder appears. Actually, as we show below, the shoulder is the time averaged tunneling current, and is caused by a surprising time-dependent behavior which we have characterized and understood thanks to comparison with theory.

### 4.1.2 Low frequency AC Josephson effect

To understand the time dependent AC signal, we first made a thorough characterization, by following the current as a function of time. For reasons that will become clear later on, we plot the voltage through the junction, which is given by the measured current divided by the resistance of the junction and an added offset.

At zero or low bias voltages (red point in Fig. 4.2(a) and red line in Fig. 4.2(b)), we observe essentially a randomly fluctuating current and voltage. When we reach the maximum Josephson current, we observe a strong time dependence of the current and voltage. At low bias, the time averaged voltage is very close to zero. However, when the voltage bias is increased, we observe peaks that appear in irregular intervals in time (orange point in Fig. 4.2(a) and orange line in Fig. 4.2(b)). When further increasing the bias, the peaks become more numerous (yellow point in Fig. 4.2(a) and yellow line in Fig. 4.2(b) and (c)), until we observe a well established oscillatory behavior (blue point in Fig. 4.2(a) and blue line in Fig. 4.2(b)).

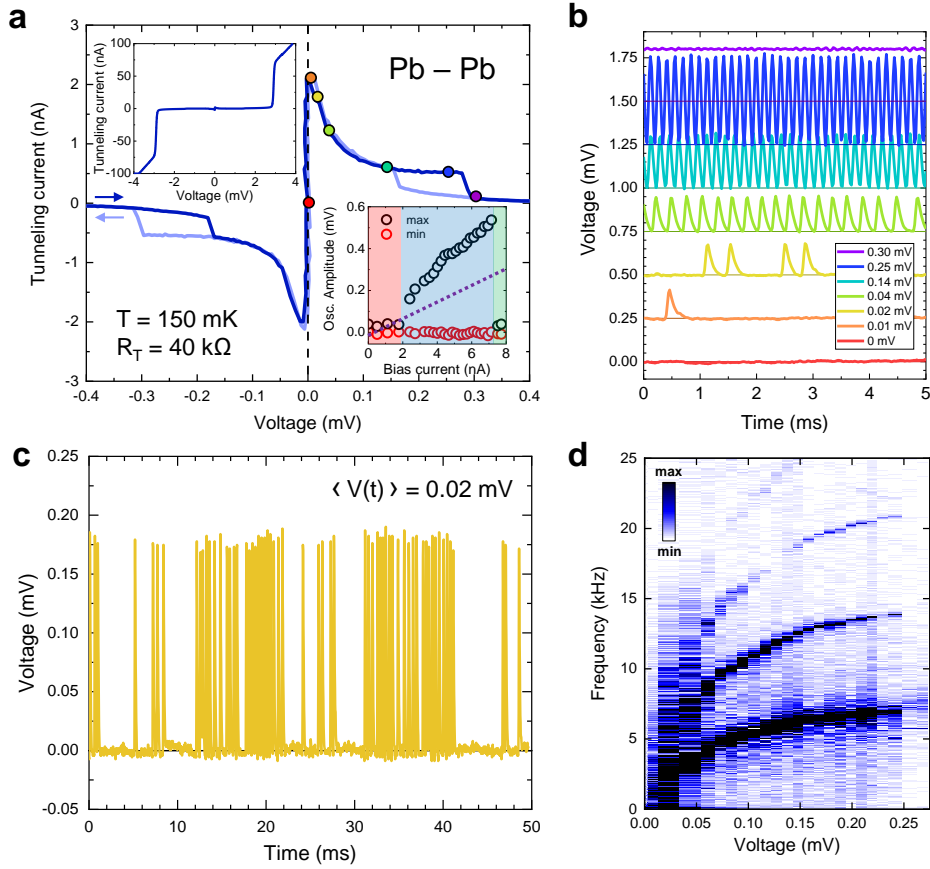


**Figure 4.2:** (a) In the main panel we show the tunneling current vs bias voltage close to zero bias. Data are shown in blue (ramp up) and violet (ramp down). Colored points indicate locations at which we trace the time dependence shown in (b) using the same colors. In the upper left inset we show the complete I-V curve up to the superconducting gap. In the lower right inset, we show as red points the minimum and as black points the maximum value of the oscillation. We plot as a dashed line the resistance of the junction outside of the Josephson regime and highlight with a colored background the three main regions of behaviour: stable (red), bistable (blue) and periodic (green), which we will discuss later in the text. The resistance of the junction is  $\approx 0.3G_0$ , with  $G_0 = \frac{h}{2e^2}$  the quantum of conductance. Curves are taken at zero magnetic field and at a temperature of 150 mK. (b) Voltage vs time at the locations given by the colors in the main panel of (a)). Curves are shifted along the y-axis by 0.25 mV for clarity. The time averaged voltage goes from zero (red) to 0.3 mV (magenta) as indicated in the legend. (c) Voltage vs time over a larger (50 ms) time window. The time averaged bias voltage is of 0.02 mV, as indicated in the legend. (d) We show as a colormap the amplitude of the Fourier transform of every voltage vs time curve taken in this experiment. Note that the ones depicted in (b) are just a mere representative selection and the actual resolution in voltage is much higher. We identify up to three main harmonic branches which convergently start at zero and increase their frequency logarithmically up to the critical voltage where the shoulder plateau disappears, and with it the oscillation.

The Fourier analysis of the time dependent voltage is shown in Fig. 4.2(d). We observe that the oscillatory behavior is well established at a clear frequency of 7.2 kHz. The Fourier transform also shows harmonics of this frequency, indicating that the oscillations are not sinusoidal, but rather have a triangular shape.

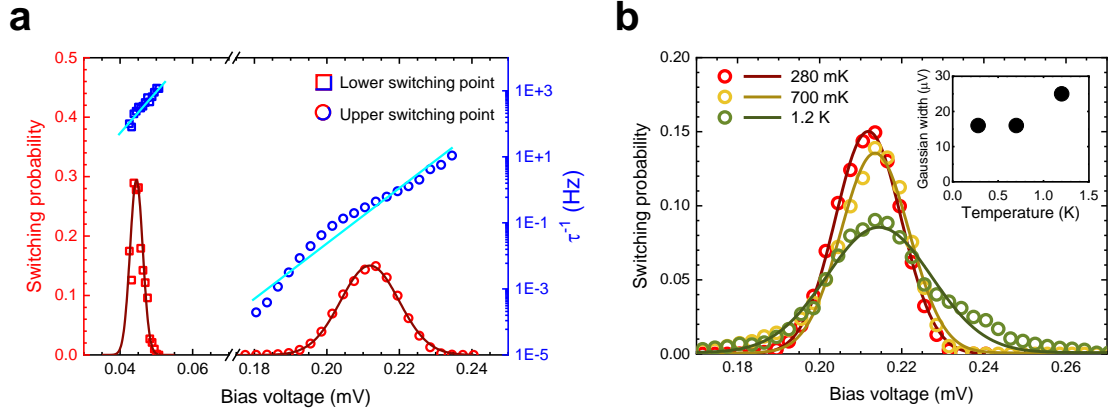


**Figure 4.3:** (a) Average lifetime (blue) and switching probability (red) of the lower (squares) and upper (circles) switching points. We confirm both phenomena to be stochastic as the lifetime decays exponentially with voltage (i.e.  $\tau^{-1}$  increases linearly in a logarithmic scale). In (b) we measure the upper switching point at three temperatures up to 1.2 K, finding that while the switching voltage remains relatively constant, the event dispersion (inset) increases with temperature.

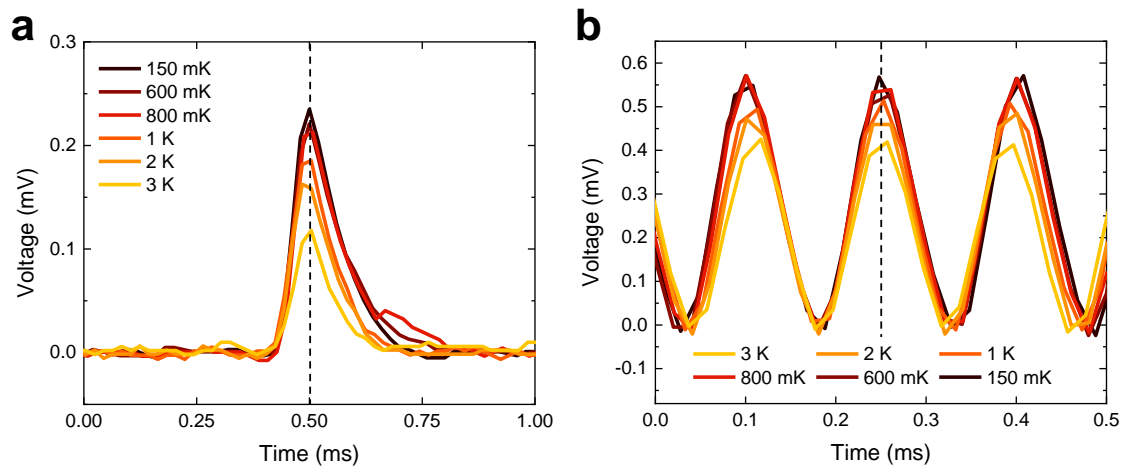


**Figure 4.4:** Dependence of the voltage oscillation with the temperature at 0.02 mV in the low bias stochastic regime (a) and at 0.25 mV in the continuous oscillation regime (b) close to the upper critical voltage when the oscillation disappears. The tunnel resistance for all curves is 40 k $\Omega$ . Increasing temperature only decreases the amplitude of the signal, whereas the main features like the shape asymmetry in (a) and the frequency dependence in (b) are temperature independent.

To better characterize this behavior, we have monitored the onset and disappearance of the oscillations. For the onset, we have counted the number of bursts appearing in a fixed period of time as a function of the bias and calculated the average time between bursts  $\tau$ . We show the result in the left side of Fig. 4.3(a) (lower switching point). We see that we obtain a rate which increases with bias voltage. From the rate, we can also obtain a probability, following Ref. [183]. The disappearance of the oscillatory behavior occurs abruptly when increasing the bias. However, the position in voltage for this disappearance is not exactly the same in each ramp. We have thus performed 10000 ramps and made a histogram of the number of times we observe the exit at a given bias. We see the result in the right side of Fig. 4.3(a) (upper switching point). Using again Ref. [183] we can calculate a switching rate, which also increases with bias voltage, and from it the switching probability. When increasing the temperature (Fig. 4.3(b)), we observe that the histogram broadens, suggesting thermally activated behavior.

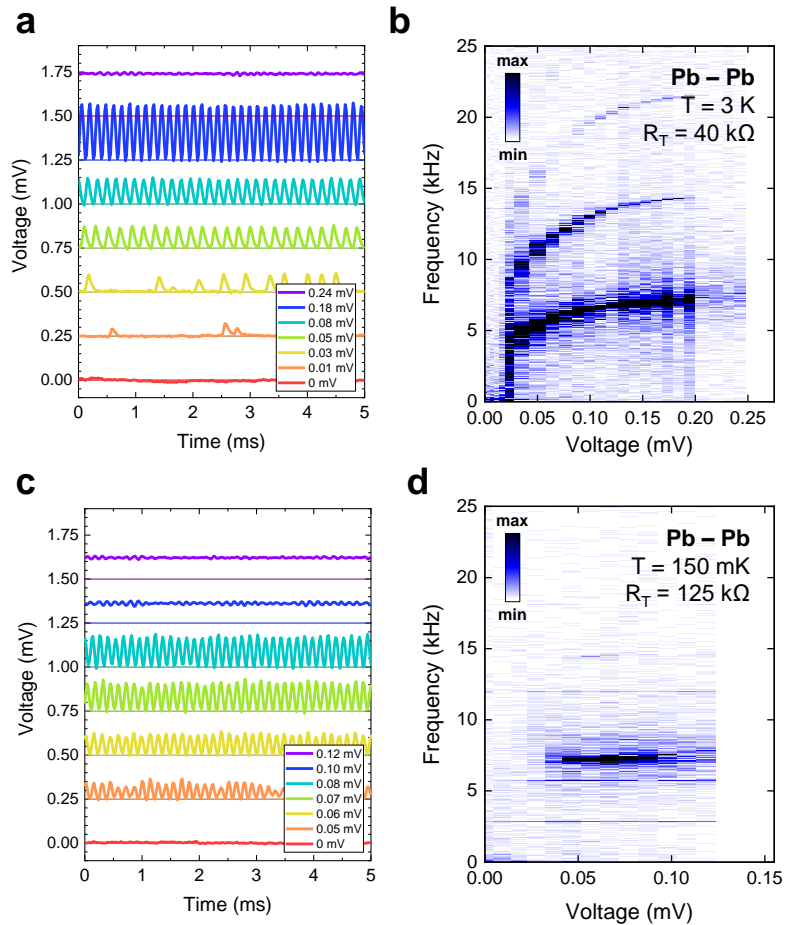


**Figure 4.5:** In (a) we show the time dependent voltage across a junction with the same resistance as in Fig. 4.2 ( $40 \text{ k}\Omega$ ) and at a temperature of  $3 \text{ K}$ . In (b) we show the Fourier transform of the time dependence, with the intensity given by the bar on the right. In (c,d) we show the same, for a temperature of  $150 \text{ mK}$  and a junction with a resistance of  $125 \text{ k}\Omega$ .

The behavior of the Josephson signal thus remains with qualitatively the same features when increasing temperature, albeit with reduced critical values above 1.2 K, as shown in Fig. 4.5(a). Increasing the tunneling resistance decreases the Josephson signal, but oscillations can be easily detected, as shown in Fig. 4.5(c). The absence of higher order harmonics in the latter experiment can be associated to a decrease in the bandwidth due to the increasing resistance.

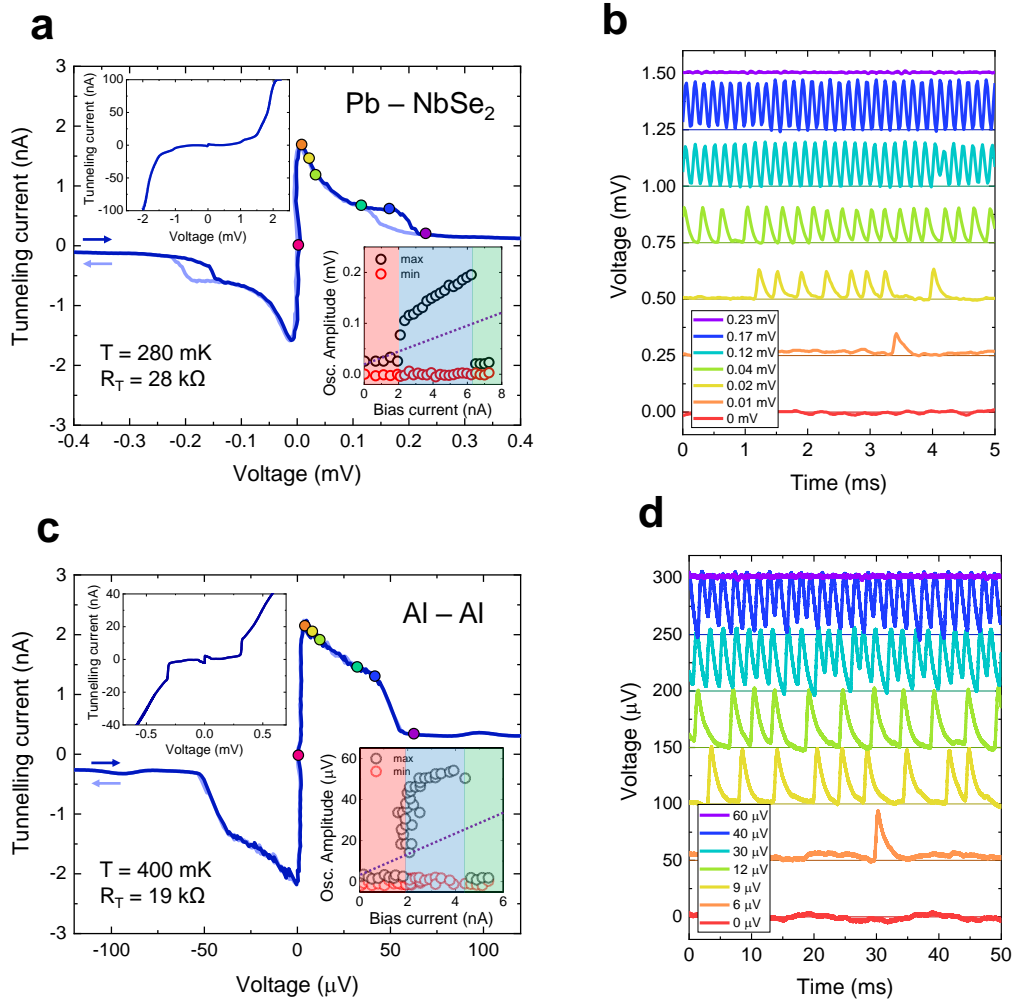


**Figure 4.6:** In (a) we show the Josephson current in a STM made with a tip of Pb and a sample of 2H-NbSe<sub>2</sub>. The colored dots correspond to the positions where we have acquired the time dependent voltage shown in (b). Curves are shifted for clarity by 0.25 mV on the vertical axis. The time averaged voltage is given in the legend. Similarly to Fig. 4.2(a), in the upper left inset we show the complete IV curve up to the superconducting gap. Also in the lower bottom inset we show the maximum (black) and minimum (red) of the oscillations and highlight the same three regimes as before in the same colors. In (c), (d) we show the same measurements as in (a) and (b), but with tip and sample of Al. In this case, in (d) curves are shifted only 50  $\mu$ V vertically.

### 4.1.3 Low frequency AC Josephson effect in other junctions

We performed comparable measurements in experiments on Al–Al and Pb–2H-NbSe<sub>2</sub>. We show the results in Fig. 4.6. The T<sub>c</sub> of 2H-NbSe<sub>2</sub> is very similar to the T<sub>c</sub> of Pb and we observe very similar features as with Pb. In Al, the energy scales are reduced due to the lower T<sub>c</sub> with respect to Pb, and again the oscillatory behavior and frequency dependence are qualitatively the same as with Pb.

## 4.2 Model for the low frequency AC Josephson effect

The classical RCSJ model presented briefly in subsection 1.4.2 cannot account for the observed behavior. With a finite bias current  $I_b$ , the model produces an oscillatory behavior. For low values of the parameter  $\eta = I_b/I_c$ , which is the normalized bias current, its associated frequency  $\omega_P$  can be approximated as:

$$\omega_P = \omega_0 (1 - \eta^2)^{\frac{1}{4}} = \frac{2\pi}{\Phi_0} (1 - \eta^2)^{\frac{1}{4}} \quad (4.1)$$

For the measured values of our experiment, the time scales associated to the oscillating Josephson current is around 300 GHz, which is far beyond our measurable bandwidth and well above the detected low frequency oscillation measured at 7.2 kHz. Thus, in collaboration with Prof. Alfredo Levy Yeyati and Dr. Samuel Escribano, we present here an extended feedback delayed RCSJ model.

### 4.2.1 Delayed feedback-driven RCSJ model

Our circuit is shown in Fig. 4.7(a). The behavior of the I-V converter or transimpedance amplifier is important. From the OP amplifier equations, we know that the voltage in both inputs to the OP is the same. As one input is grounded, this produces a low impedance connection between one side of the junction and ground. The junction is biased by a current. The OP amplifier provides a feedback current through the resistor  $R_F$  which is exactly equal to the current flowing through the junction. The output of the circuit is then the voltage at the point  $I_m$ , which is proportional to the current through the junction. The current through the junction follows the RCSJ model, but the junction is connected to the feedback circuit of the OP amplifier. The feedback is delayed on a time scale which is given by the resistor  $R_F$  and the circuit capacitance in parallel to this resistor (not shown in Fig. 4.7(a)). The latter includes, in particular, the capacitance to ground of the wiring into the cryostat. The RCSJ equation with a feedback term is given by:

$$\frac{dx_2}{d\tau} = -\frac{1}{\beta} [\sin(x_1) + x_2 + i] + k[x_2(t - t_*) - x_2(t)] \quad (4.2)$$

being  $t_*$  the time constant of the feedback circuit and  $k$  a coupling term. When the voltage is zero below the critical current,  $x_2 = 0$  and we yet again recover

Equation 1.25, the first Josephson relation. However, above the critical current we can still have a solution with zero bias voltage. If at a certain time window,  $x_2(t - t_*) - x_2(t) < 0$ , then adding the additional feedback term is equivalent to reducing the current  $i$  in Equation 4.2. Thus, there is a range of bias currents  $i > 1$  above the critical current of the junction where the feedback effectively reduces the tilt in the washboard potential: the system oscillates between a state where the feedback reduces the tilt and a state in which it increases the tilt (see Fig. 4.7(b)). The oscillations induced by the feedback occur over a period  $t_*$ .

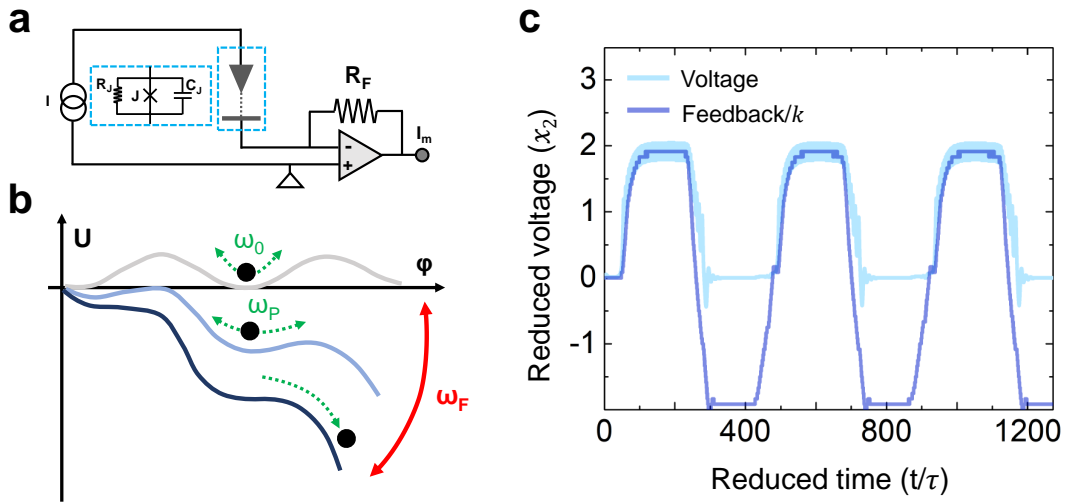


**Figure 4.7:** (a) Simplified circuit used in a STM setup. A bias is applied to a superconducting tip (grey vertical triangle) and the tunneling current flows into a superconducting sample (grey horizontal bar). We model the tip-sample junction through a standard RCSJ model, so that the blue dotted boxes are equivalent. The current flowing through the circuit is measured using an operational amplifier (grey horizontal triangle) in a current-to-voltage converter configuration. The operational amplifier's feedback mechanism nulls both entrances, in such a way that the current flows through  $R_F$  to ground, creating a voltage at the output which is proportional to the tunnel current. In presence of an oscillating current, the feedback responds with a delay, determined by  $R_F$  and the capacitance of the circuit. (b) As we show in the text, the feedback periodically eliminates and enhances the bias current, i.e. the tilt in  $U$  (red arrow) at a frequency  $\omega_F$ . (c) We show in light blue  $x_2(t)$  obtained from Equation 4.2 for the parameters indicated in the text and a current slightly above  $I_c$ . We show in dark blue the term  $(x_2(t - t_*) - x_2(t))$  in Equation 4.2. We have chosen the units at the y-axis in such a way that the result of RCSJ without feedback is 1. We see by this comparison that the feedback oscillates between a state where it provides twice the voltage across the junction as compared to the non-feedback case, and a state where it exactly compensates the tilt of the washboard potential and leads to zero voltage across the junction. Thus, the feedback periodically returns the junction to the zero voltage state above the critical current.

As an example, in Fig. 4.7(c) we plot  $x_2$ , i.e. the voltage, as a function of time

normalized to  $\tau$ . The feedback is divided by  $k$ . We use  $k = 2$ ,  $\beta = 4$  and  $t_*/\tau = 200$ . We can see that  $x_2$  switches between zero voltage where the feedback term is exactly equivalent to  $i$  in Equation 4.2, and a finite voltage state where the magnitude of  $x_2$  is twice the one obtained in absence of feedback as the feedback term enhances the tilt of the washboard potential.

Equation 4.2 has regimes with different degrees of stability and, adding temperature fluctuations, provides qualitatively the same results as we observe in the experiment.

## 4.2.2 Dynamics at the Josephson and the feedback frequencies

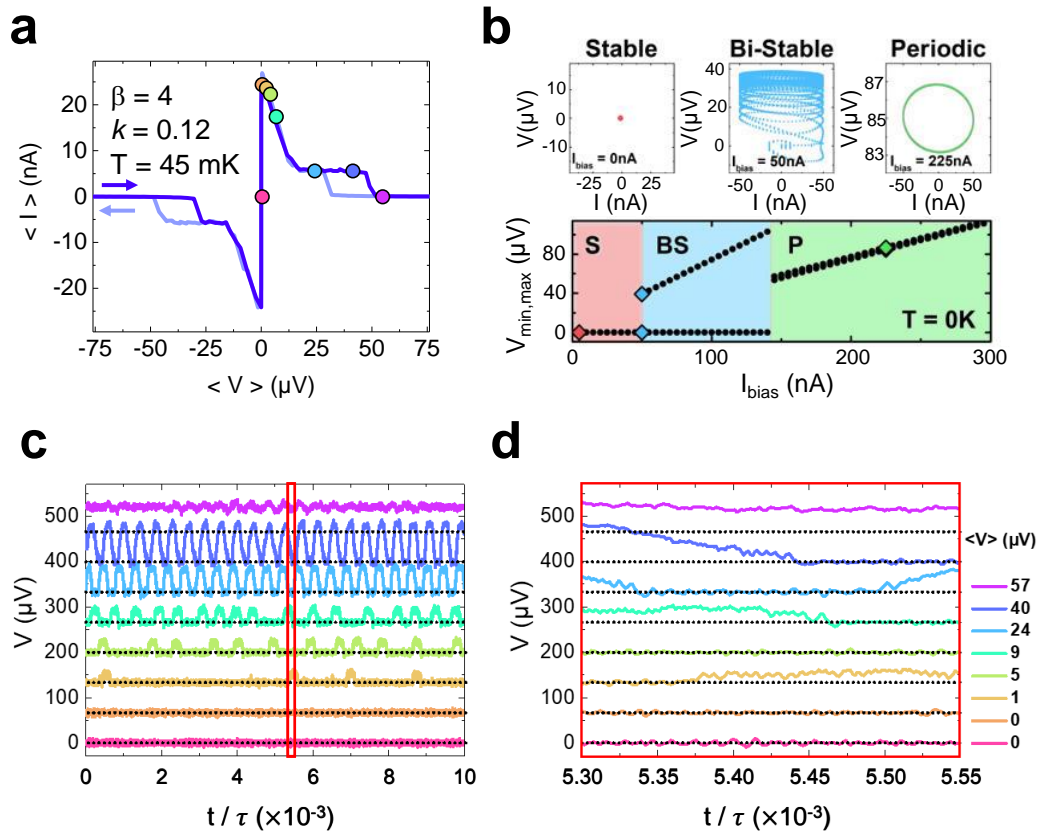


**Figure 4.8:** (a) Time-averaged I-V curve for the parameters indicated in the graph, where we can identify the main features observed in the experiment. In (b) we show as black dots the maximum and minimum values of the voltage across the junction and identify three different branches which correspond to different trajectories in the I-V plane, plotted in the upper part of the panel. Note that the color palette for each branch is the same we employed previously in the insets of Fig. 4.2(a) and Fig. 4.6(a) and (c). In the next panels we show a long (c) and short (d) time ranges taken at the colored dots marked in (a).

We show in Fig. 4.8(a) the time-averaged current and bias of the junction with the parameters indicated in the panel (calculations made by Samuel Escribano and A. Levy Yeyati, as well as by David Perconte). We can reproduce the main features observed in the experiment, like the hysteresis and the shoulder plateau after the peak. In a similar way to Fig. 4.2, we choose some fixed bias points and show the time evolution in Fig. 4.8(c) and (d). Note that Fig. 4.8(d) is just a zoom inside the red square region marked in Fig. 4.8(c). We reproduce again the main features of the voltage vs time curves, like the stochastic bursts right after the peak and the constant oscillation above the critical current, which suddenly disappears at an upper switching point. Finally, in Fig. 4.8(b) we show as black dots the maximum and minimum value of the voltage with time and obtain the same three differentiated regions we identified in the inset of Fig. 4.2(a). In order to discuss this behavior and avoid thermal noise we set here  $T=0$ . At low bias, we observe a stable DC Josephson current with zero voltage through the junction. At intermediate bias, above the critical current, there is a bi-stable behavior. The junction switches between a state with zero voltage and a state with a finite voltage. At still higher bias values, we find periodic oscillations at high frequencies (not shown in Fig. 4.8(b)).

### 4.3 Conclusion

The observed new AC Josephson effect is a surprising connection between high frequency Cooper pair quantum oscillations, thermal noise and low frequency electronics. It is completely reproduced by the RCSJ model with a delayed feedback term added. First, it fully explains the shoulder plateau observed previously in DC measurements as a consequence of time averaging the newly observed AC behavior. This validates the measurement of the shoulder plateau as a measurement of the local Josephson coupling. Second, it provides a stable Josephson coupling at a bias that is well above the critical current. It should be interesting to explore this effect further, as it might be useful in the design of SQUID or high frequency electronics. As we show in Fig. 4.8(c), when the junction switches, the current is oscillating at very high frequencies in the position where the DC voltage is finite. Therefore, the existence of low frequency oscillations is a direct evidence of the high frequency AC Josephson oscillations, which can be detected by measuring a low frequency signal. The junction thus acts as an intermediate frequency amplifier, allowing the measurement of high frequency Josephson oscillations at a fixed frequency in the kHz range. We can speculate that nanofabricated rings with two parallel junctions (having similar resistance and capacitances as the ones obtained in STM) coupled to a feedback circuit might also show this novel feedback behavior at low frequencies. We did not investigate this possibility, but we can anticipate a low frequency (radiofrequency) modulation of the critical current. And third, it allows for measuring the Josephson effect at the atomic scale by measuring the signal at exactly one frequency, using a sharp notch filter after the I-V converter. This should considerably improve the signal to noise ratio in Josephson Scanning Spectroscopy.

## 5 | Correlations and bound states in 2H-NbSe<sub>1.8</sub>S<sub>0.2</sub>

Transition metal dichalcogenides have been traditionally studied in depth using STM. The layered structure generally provides excellent surfaces where STM can be easily used to measure the atomic structure and the density of states. As shown in the introduction, superconductivity and vortex lattices have been extensively studied, in 2H-NbSe<sub>2</sub> as well as in other similar layered compounds [76, 14, 184, 185, 79, 24, 26]. Very recently, it has been shown that few layers of these systems also show superconducting properties. The critical temperature is strongly reduced in single layers of 2H-NbSe<sub>2</sub> [75] and enhanced in single layers of 2H-TaSe<sub>2</sub> and 2H-TaS<sub>2</sub> [186, 187], sometimes offering radically new superconducting properties, such as heavy fermion [188] or Ising superconductivity [189]. Whenever STM measurements of the superconducting gap are available, these share a seemingly unavoidable extreme smearing [190, 191], with tunneling conductance having a large zero bias density of states and small coherence peaks, and which contrasts to the clean *s*-wave tunneling conductance curves ubiquitously obtained in the bulk [76, 14, 184, 185, 79]. This situation is very different also to results in another single layer superconductor, FeSe [192], which shows a zero density of states at low energies. These results raise the question for the origin of the finite density of states at the Fermi level in transition metal dichalcogenides.

On the other hand, it is well known that superconductivity is depressed through the exchange interaction between Cooper pairs and magnetic impurities and through the orbital interaction that leads to vortices. Both perturbations induce a finite density of states inside the superconducting gap. In vortices, the superconducting density of states is often not zero close to the vortex center due to the formation of in-gap CdGM states [25, 76, 14].

Similarly, the so-called gapless state can occur in presence of magnetic impurities [39, 193]. This gapless superconductivity occurs for a very large concentration of magnetic impurities [42]. Isolated magnetic impurities locally induce in-gap YSR states [194, 50, 195, 196, 197, 198]. The influence of reduced dimensionality in superconductors with a small amount of magnetic impurities has not been studied.

Recently, it has been shown that chains of magnetic atoms present a peak at zero energy that has been associated to Majorana excitations [199, 200, 201]. To be able to identify and use such unconventional states, it is important to characterize and understand the behavior of YSR states in the superconductor. Here in particular we address the issue of reduced dimensionality and the influence of the vortex

lattice. I will show that reduced dimensionality produces significant modifications of the superconducting density of states in the whole sample, leading to gapless superconductivity at very small magnetic impurity concentrations. To this end, I will address the behavior of isolated magnetic impurities in the superconductor  $2\text{H-NbSe}_{1.8}\text{S}_{0.2}$ . I will also study the mutual influence of magnetic impurities and vortices in detail, both in  $2\text{H-NbSe}_2$  and  $2\text{H-NbSe}_{1.8}\text{S}_{0.2}$ . Magnetic impurities lead to a axially asymmetric superconducting density of states around vortex cores.

## 5.1 YSR states in $2\text{H-NbSe}_2$ : state of the art

As introduced in [subsection 1.2.5](#), isolated magnetic impurities produce YSR bound states in the superconducting gap. The position of the peaks as well as the spatial distribution of such states provides useful information about the magnetic and electronic properties of the material [50, 202].

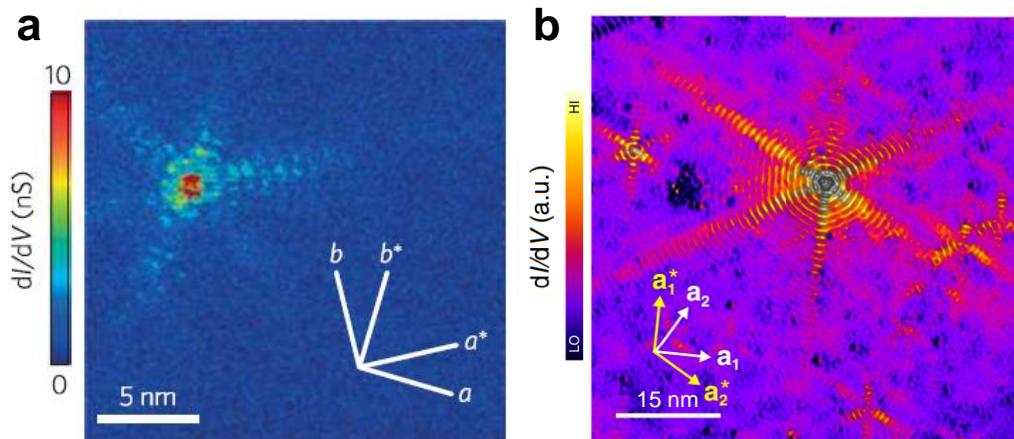


**Figure 5.1:** Adapted from Refs. [50, 202]. Experimental results of STS measurements on  $2\text{H-NbSe}_2$  (a) and  $\text{La}(0001)$  (b) with magnetic impurities.

We see in [Fig. 5.1\(a\)](#) that the impurity on a  $2\text{H-NbSe}_2$  surface shows a characteristic sixfold shape [50]. We also show results in  $\text{La}(0001)$  surface in [Fig. 5.1\(b\)](#) [202]. The oscillatory behavior of the YSR density of states close to impurities is strongly linked to the band structure: along certain directions, the wavefunction extends to longer distances, providing the extended patterns we see in [Fig. 5.1\(a,b\)](#) along the arms of the star. These directions coincide with positions where the band structure has particular properties [50, 202]; for instance in  $2\text{H-NbSe}_2$ , the sixfold star shape follows the direction of the CDW, suggesting that along these directions there is a stronger interaction with the magnetic impurity, probably due to a stronger density of states [203]. This is further analyzed in great detail in experiments where Fe is deposited in different places with respect to the CDW [198]. An additional interesting work studies in detail the influence of the

two band character of 2H-NbSe<sub>2</sub> in the shape of the density of states [197]. In La, the directions coincide clearly with flat portions of the Fermi surface [202]. These provide enhanced electronic interactions and have been shown to strongly influence scattering also on the normal state [120]. On the other hand, coupling between close lying impurities in 2H-NbSe<sub>2</sub> was studied in Ref. [196]. Other systems presenting a strong influence of the crystal lattice in YSR states are Nb [204] and  $\beta$ -Bi<sub>2</sub>Pd [205, 206].

Here we study 2H-NbSe<sub>2</sub> doped with S in 10% of the Se sites, i.e. 2H-NbSe<sub>1.8</sub>S<sub>0.2</sub>. These samples also contain embedded Fe impurities below 150 ppm. We show that the level of disorder introduced by the small amount of S doping significantly enhances the density of states in between isolated magnetic impurities, leading to gapless superconductivity. By comparing the oscillatory patterns around isolated impurities with band structure calculations made by the group of J. Baldoví in Valencia, we see that YSR oscillatory patterns occur in certain directions in which the density of states is enhanced. Calculations show that this enhancement is due to the effect of randomly distributed S. The S dopants, being located at different positions in each layer, produce a reduction of the dimensionality, making each layer different from its neighbor. The reduced dimensionality allows for the observation of certain wave vectors in the YSR states in 2H-NbSe<sub>1.8</sub>S<sub>0.2</sub> that are absent in 2H-NbSe<sub>2</sub>. We attribute this to the enhanced DOS along certain band structure hot spots appearing due to the reduced dimensionality in 2H-NbSe<sub>1.8</sub>S<sub>0.2</sub>. Furthermore, we also analyze the effect of magnetic impurities in the CdGM vortex core states.

## 5.2 Spatial extension of YSR states in 2H-NbSe<sub>1.8</sub>S<sub>0.2</sub> at zero magnetic field

### 5.2.1 Influence of S doping

We show in Fig. 5.2(a) a YSR impurity in pure 2H-NbSe<sub>2</sub>. We identify the sixfold pattern described previously (see Fig. 5.1(a)). However in 2H-NbSe<sub>1.8</sub>S<sub>0.2</sub>, when we measure Fe impurities we find instead a threefold pattern, as shown in Fig. 5.2(b).

We can compare this result with theoretical calculations, which were made by J. Baldoví in Valencia and are described in Ref. [32]. We show the atomic positions of Nb and Se in 2H-NbSe<sub>2</sub> in Fig. 5.2(c) and of Nb, Se and S in 2H-NbSe<sub>1.8</sub>S<sub>0.2</sub> in Fig. 5.2(d). We see that S (yellow atoms in Fig. 5.2(d)) produces slight distortions in the atomic positions in each layer. We also see that the position of each S atom in a layer is random and that those lying close to the Fe impurity (red blob in Fig. 5.2(c,d)) influence the environment of the Fe impurity. A calculation of the spin density at the impurity (red for spin up and blue for spin down in Fig. 5.2(c,d)) brings more insight. We see that the exchange coupling between magnetic Fe and the neighboring atoms occurs mainly with Nb atoms in pure 2H-NbSe<sub>2</sub>. As we describe below, almost all Fermi surface sheets are derived from Nb orbitals (see Fig. 5.5(c) and (d)). The exchange coupling in 2H-NbSe<sub>2</sub> is antiferromagnetic and has a sixfold symmetry, which is very similar to the sixfold symmetry of the YSR

state. This suggests that the anisotropy of the exchange coupling is influenced by the anisotropy of the band structure. In  $2H\text{-NbSe}_{1.8}\text{S}_{0.2}$ , the exchange coupling is also antiferromagnetic and occurs with both Nb and Se. This implies a threefold exchange anisotropy. In addition, because of the Se by S substitution, the exchange coupling has a slight additional anisotropy (towards the top in the upper panel of Fig. 5.2(d), where S atoms are located in the regions with smaller exchange coupling in the layer immediately below, as shown in the lower panel of Fig. 5.2(d)). Therefore, the distribution of S atoms modifies the in-plane anisotropy of the exchange coupling of the Fe impurities, as we show in Fig. 5.2(b).

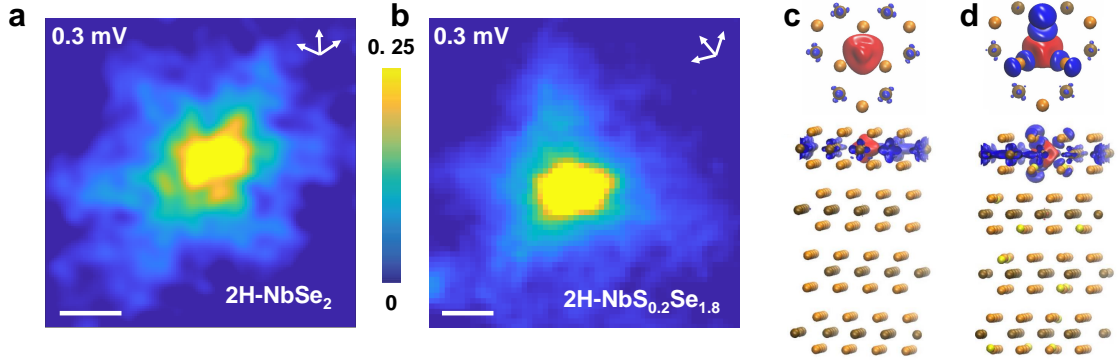


**Figure 5.2:** Measured tunneling conductance maps at a Fe impurity in  $2H\text{-NbSe}_2$  (a) and in  $2H\text{-NbSe}_{1.8}\text{S}_{0.2}$  (b). White arrows provide the crystalline directions of the atomic Se lattice and white scale bars are 2 nm long. (c) Spin density isosurface of  $2H\text{-NbSe}_2$  and (d) of  $2H\text{-NbSe}_{1.8}\text{S}_{0.2}$  obtained from DFT+U calculations. Red stands for spin up and blue for spin down charge density. The isosurface is plotted for an imbalance by 0.002 of the spin density. The Fe atom (not shown) is located on the red spot, substituting a Nb atom. Se atoms are orange and Nb atoms ochre. We represent the two uppermost unit cells from the top. S atoms are located randomly in the layers below, shown in the lower panel of (c) and (d). Calculations are made on four Nb-Se and Nb-Se-S layers, using  $4 \times 4 \times 2$  sized slabs.

### 5.2.2 Oscillatory pattern of YSR states in $2H\text{-NbSe}_{1.8}\text{S}_{0.2}$

To further analyze the origin of the coupling that leads to the YSR states, we can investigate the oscillatory behavior in detail. To this end, we have to take a closer look on a large image, showing a couple of Fe impurities and study the tunneling conductance at many bias voltages with great detail. In each case, we make a C6 symmetrization of the FFT, to unveil more clearly the wave vectors of the oscillations in the YSR states. These results are presented in Fig. 5.3.

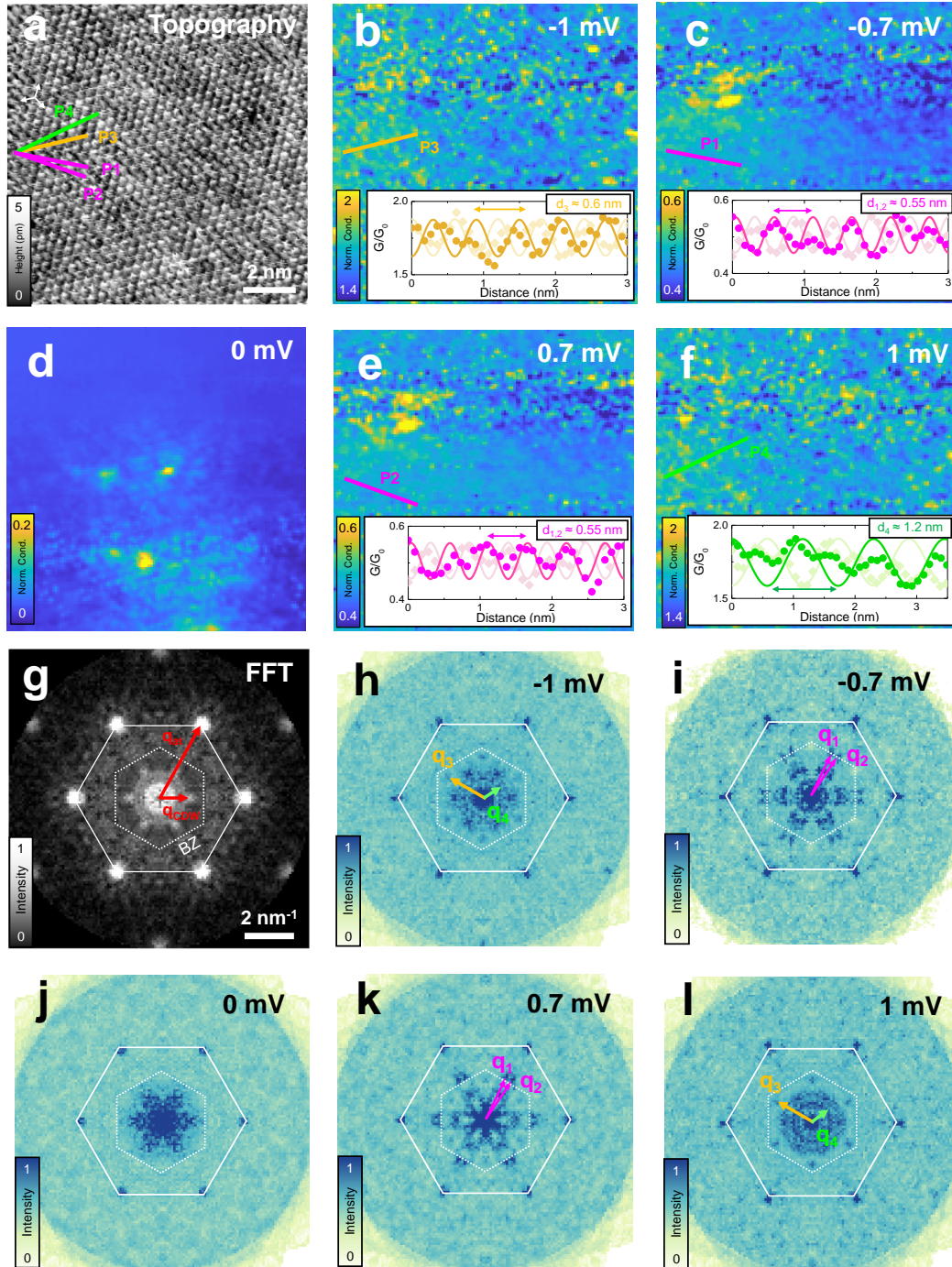


**Figure 5.3:** (a) Topography of a small field of view in  $2H\text{-NbSe}_{1.8}\text{S}_{0.2}$  (scale bar given in the bottom right part of the panel). Color scale corresponds to height changes, following the scale bar on the bottom left. (b-f) Tunneling conductance maps in the same field of view, for the bias voltages marked at the top right part. The tunneling conductance color scale is given by the bar on the bottom left. We select a few profiles and plot these as insets (points are data from the image and the lines are a guide to the eye, dark colors are at a positive bias and light colors at a negative bias). (g) 2D-FFT of (a). (h-l) 2D-FFT of (b-f). The Fourier transforms are  $C6$  symmetrized. Colored arrows in (h-l) show the main scattering wave vectors, named  $q_{1-4}$ .

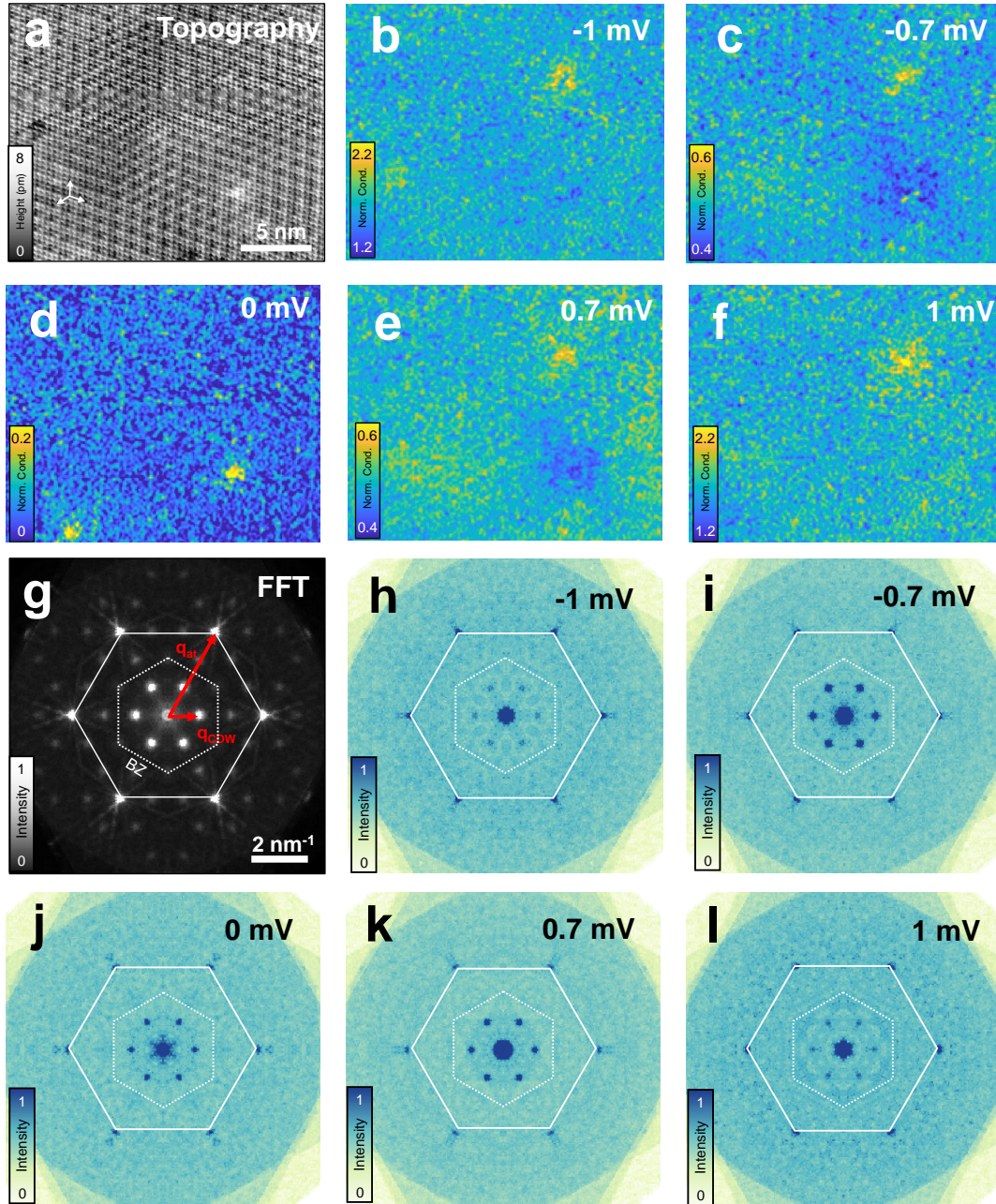


**Figure 5.4:** (a) Topography of a small field of view in  $2H-NbSe_2$  (scale bar given in the bottom right part of the panel). Color scale corresponds to height changes, following the scale bar on the bottom left. (b-f) Tunneling conductance maps in the same field of view, for the bias voltages marked at the top right part. The tunneling conductance color scale is given by the bar on the bottom left. (g) 2D-FFT of (a). (h-l) 2D-FFT of (b-f). The Fourier transforms are  $C_6$  symmetrized.

Let us first focus on the real space conductance maps (Fig. 5.3(b-f)). We best see the locations of the Fe impurities in (d). These produce an oscillatory pattern that extends over the field of view. We focus on the pattern on one side of the field of view, shown by the colored lines in the topography (Fig. 5.3(a)). We trace the

tunneling conductance as a function of the position along the colored lines in (b-f) and identify an oscillatory pattern. When comparing this oscillatory pattern for positive and negative bias voltages, we observe a  $\pi$  phase shift, reminiscent of YSR oscillations that extend from the Fe impurity sites [50, 31].

The Fourier transform brings more insight into the origin of these oscillations (Fig. 5.3(h-l)). As mentioned before, the Fourier transform is C6-symmetrized, in order to reduce the noise and be able to identify the spots in Fourier space. The Fourier transform of the topography (Fig. 5.3(d)) serves as a reference for the positions of the atomic and CDW Bragg peaks. We see that the oscillations at  $\pm 1$  mV have two wave vectors, both different from the CDW and atomic lattice and marked in Fig. 5.3(h,l) as  $q_3$  and  $q_4$ . At  $\pm 0.7$  mV, these two wave vectors are no longer visible in the images and we find two different wave vectors, which are symmetric with respect to the crystalline direction  $\Gamma M$  and which we label  $q_1$  and  $q_2$  at Fig. 5.3(i,k). Notice that while  $q_1$ ,  $q_2$  and  $q_3$  are vectors pointing to spots in Fourier space,  $q_4$  rather points to a circle, which is more clearly visible for the electron states in Fig. 5.3(l).

We can compare these results with observations in a field of view of similar size in pure 2H-NbSe<sub>2</sub>, which we show in Fig. 5.4. We see that all the abovementioned wave vectors  $q_{1-4}$  are absent in this case. The scattering signal shows the anisotropies that have been unveiled previously, with a star shaped pattern [50] as in Fig. 5.2(a).

Thus, we conclude that the enhanced scattering along these wave vectors  $q_{1-4}$  observed in 2H-NbSe<sub>1.8</sub>S<sub>0.2</sub> is due to the substitution of Se by S. To understand this point, we compare our experimental results again with calculations of the electronic band structure made by Jose Baldoví. The Fermi surfaces obtained for 2H-NbSe<sub>2</sub> and 2H-NbSe<sub>1.8</sub>S<sub>0.2</sub> on similarly sized slabs are shown in Fig. 5.5(a) and (b). Both Fermi surfaces resemble in their shape: there are two nearly two-dimensional Nb-derived sheets, centered at the  $\Gamma$  point of the Brillouin zone and other two Nb-derived also nearly two-dimensional sheets at the Brillouin zone corners in K. Furthermore, there is a Se derived three-dimensional pancake at the center of the Brillouin zone. We see that the wave vectors at around  $\pm 0.7$  mV ( $q_1$  and  $q_2$  in Fig. 5.3(h,l)) can be identified with highly directional scattering between symmetry-equivalent spots of the outer Nb-derived quasi-2D sheets centered at K (magenta arrows in Fig. 5.5(a)). On the other hand, at  $\pm 1$  mV, we find  $q_3$  that joins the flat portions of the outer Nb-derived quasi-2D  $\Gamma$ -centered bands (yellow arrow in Fig. 5.5(a)). Finally, also at  $\pm 1$  mV, we detect another wave vector associated to the 3D Se derived pancake pocket, which we identify as  $q_4$  (green arrow in Fig. 5.5(a)).

The calculated band structures of 2H-NbSe<sub>2</sub> and 2H-NbSe<sub>1.8</sub>S<sub>0.2</sub> are shown in Fig. 5.5(c) and (d). Note that we show in red the bands at the basal  $\Gamma MK$  plane, and in blue at the top and bottom Brillouin zone ALH planes. To perform the calculations in 2H-NbSe<sub>1.8</sub>S<sub>0.2</sub>, it was needed to use finite slabs using the relaxed atomic positions. This leads to the usual multiple sub-bands characteristic of slabs. It is therefore important to compare results obtained in slabs of the same size in 2H-NbSe<sub>2</sub> and in 2H-NbSe<sub>1.8</sub>S<sub>0.2</sub>.

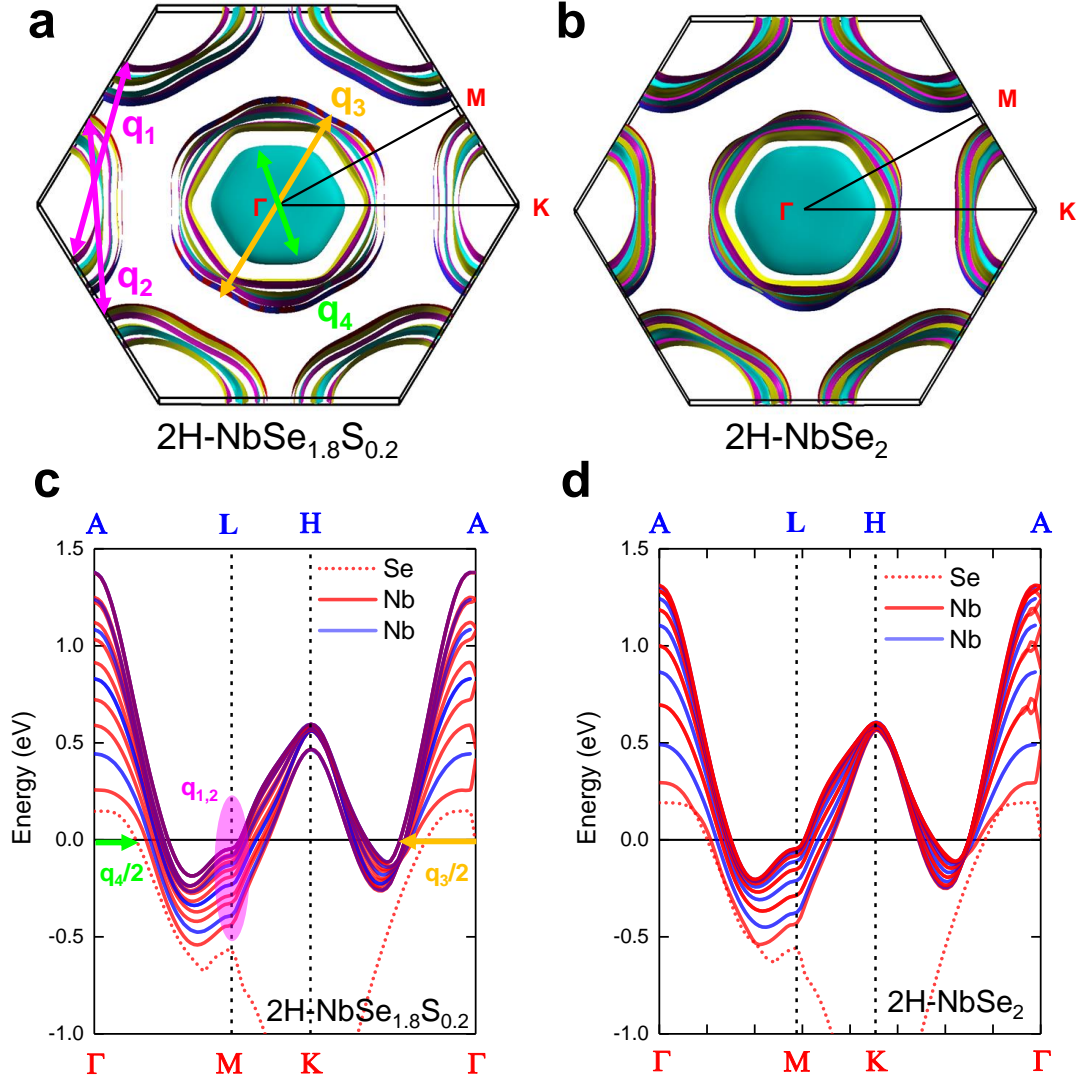


**Figure 5.5:** In (a) we show the Fermi surface of an infinitely repeated relaxed  $4\times 4\times 2$  unit cells slabs of  $2\text{H-NbSe}_{1.8}\text{S}_{0.2}$ , projected to the hexagonal basal plane. Notice that bands are split due to the boundary conditions, as explained in the text. In (a) we plot with colored arrows the wave vectors  $q_{1-4}$  shown in in Fig. 5.3(h-l). We see that we can find nearly the same wave vector in each inequivalent layer, with only small changes in its direction or magnitude. In (b) we show the Fermi surface of  $2\text{H-NbSe}_2$  for comparison, calculated on same sized slabs. The same colors code for the bands as in (a) has been used. In (c) and (d), we plot the whole calculated band structure of  $2\text{H-NbSe}_{1.8}\text{S}_{0.2}$  and  $2\text{H-NbSe}_2$ , respectively. Notice that bands are split due to the finite size of the slab edges. We plot in red the bands in the  $\Gamma\text{MK}$  plane at  $z=0$ , and in blue the bands in the ALH plane at  $z=\pm\pi/2$ . The red and blue lines have a certain transparency, hence fully overlapping bands will appear purple. We observe that the overall overlap between blue and red bands (i.e. the 2D-character of the bands) is greatly enhanced in the S doped case, and thus the purple color is predominant in (c).

Qualitatively, the results in 2H-NbSe<sub>2</sub> shown in Fig. 5.5(d) are similar as in the bulk [207, 208], except for the multiple sub-bands. We see, in particular, that the band character is never completely 2D, i.e. that the blue and red bands never fully overlap. Nevertheless, a simple visual comparison between Fig. 5.5(a) and (b) suggests that the 2D-character in the S doped sample is greatly enhanced. We find strongly two-dimensional bands in 2H-NbSe<sub>1.8</sub>S<sub>0.2</sub> (Fig. 5.5(c)) along  $\Gamma K$  and  $MK$  directions. To highlight the 2D-character, we have plotted the bands for  $k_z = 0$  in red and for  $k_z = \pm\pi/2$  in blue, allowing for a certain degree of transparency. We see that in Fig. 5.5(c) there are many sub-bands where there is a strong overlap between  $k_z = 0$  and  $k_z = \pm\pi/2$ . Thus, the dispersion relation becomes significantly 2D. Along  $\Gamma K$  we can identify the wave vector  $q_3$ , which is then enhanced in 2H-NbSe<sub>1.8</sub>S<sub>0.2</sub> with respect to 2H-NbSe<sub>2</sub> because of the reduced dimensionality. We also see that along  $MK$ , the bands are more 2D, but the density of states is increased close to the M point, due to flattening of the bands around the van Hove anomaly [209]. This allows us to identify the wave vectors  $q_1$  and  $q_2$ . Finally, the inner Se derived pocket shrinks in 2H-NbSe<sub>1.8</sub>S<sub>0.2</sub>, so that the oscillatory pattern due to this pocket can be more easily discerned than in 2H-NbSe<sub>2</sub>.

Thus, we see that the main effect of the Se by S substitution is to reduce the dimensionality of the system. Each layer is different from the adjacent layer, due to the random distribution of S atoms inside the structure. This enhances long range YSR states with an oscillatory pattern connected with portions of the Fermi surface having a pronounced 2D-character.

### 5.2.3 Gapless superconductivity in areas with a very large concentration of Fe impurities

The distribution of Fe inside the sample is random, which means that there are arbitrarily large variations in the density of impurities at local scale. As we show now, we can find places on the sample where the average distance between impurities is of 25 nm, and other places on the sample where the average distance between impurities goes down to 18 nm (previously shown results were obtained in fields of view with average interimpurity distance  $>22$  nm). In Fig. 5.6 we show the tunneling conductance maps in five different fields of view, each one approximately 100 nm in lateral size, with different average interimpurity distances, indicated on top of each column. Let us first remark that there are no significant fluctuations of the density of states for voltages well above the quasiparticle peaks (not shown in Fig. 5.6). At zero bias (central row of Fig. 5.6) we observe clear spots at each impurity. The spots have all a similar size. Notice that, while the tunneling conductance in between spots is zero in (a-c), it is finite in (d,e). This situation changes at a finite bias ( $\pm 0.7$  mV in Fig. 5.6). Spots are clearly much more extended in space than at zero bias in (a-c). In (d,e), by contrast, there is no apparent dependence of the spot size with the bias voltage.

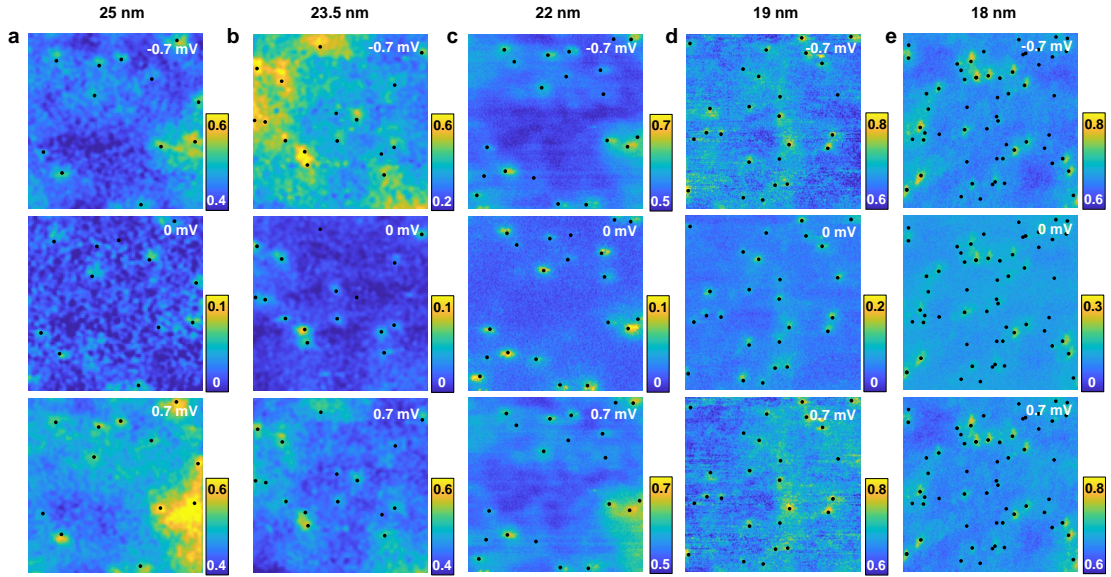


**Figure 5.6:** (a-e) Tunneling conductance maps made at the bias voltages marked in each panel (-0.7 mV top, 0 mV middle and 0.7 mV bottom). Maps are taken in different fields of view, with increasing number of YSR states from (a) to (e). The position of magnetic impurities is indicated with black dots, and the average distance between dots is indicated in the top part of each column. The size of all images is  $100 \times 100 \text{ nm}^2$ . The color scale in conductance normalized to its high bias voltage value is given by the color bars at the bottom right of each panel.

Let us discuss in detail the situation depicted in Fig. 5.6. In (a) we show a field of view where the average distance between Fe impurities is of 25 nm. The Fe impurities provide, at zero bias, round spots between 10 and 20 nm lateral size. Far from the impurities, the tunneling conductance is essentially zero. When we look on the conductance at negative bias, we observe that the spots extend to larger distances (top panel of Fig. 5.6(a)). For positive bias (bottom panel of Fig. 5.6(a)), the same spots extend to even larger distances. In Fig. 5.6(b) we show a field of view with practically the same Fe impurity density, the average distance between impurities is of 23.5 nm. Here we observe qualitatively the same effect, YSR spots that increase their spatial extension for finite bias voltages. But the spatial extension is now much larger for positive bias (top panel of Fig. 5.6(b)). In other fields of view, with a larger density of Fe impurities (and thus shorter average interimpurity distances, see Fig. 5.6(c-e)), we observe that the bias voltage asymmetry in the spatial extension is essentially lost. Furthermore, the zero bias tunneling conductance in between impurities deviates significantly from zero. Notice, for instance in Fig. 5.6(e), middle panel, that the zero bias conductance is non-zero even in areas where there are practically no Fe impurities.

We can further follow this behavior in the extension of the YSR states by calculating the radially-averaged autocorrelation function  $ACF$  as a function of the distance  $r$ ,  $ACF(r)$  for different bias voltages (see subsection 2.4.4). In an image showing spots, as the middle panel in Fig. 5.6(a),  $ACF(r)$  decreases to zero and

the decay provides a measure of the average size of the spots in the image. When spots become larger as in the image at 0.7 mV in Fig. 5.6(a), the decay length of  $ACF(r)$  increases. In Fig. 5.7 (a-e) we show the results for the fields of view of Fig. 5.6. Close to zero bias,  $ACF(r)$  decays exponentially with a distance of about 10 nm in Fig. 5.7 (a-e). At a finite bias voltage, we observe a considerable increase of the decay distance of  $ACF(r)$  up to somewhat above 20 nm (white crosses in Fig. 5.7(a-e)). The  $ACF(r)$  shows a non-zero correlation at distances of nearly 100 nm. Furthermore, the decay distance is different for positive and negative bias voltages. The field of view considered in Fig. 5.7(a) has impurities whose extension for positive bias is much larger than those at negative bias. This reverses in Fig. 5.7(b). However, for Fig. 5.7(d) and in particular in Fig. 5.7(e),  $ACF(r)$  shows a strong energy-independent exponential decay at distances of order of 10 nm. At the same time, the averaged tunneling conductance vs bias voltage on each field of view Fig. 5.7(f) shows a conductance that remains close to zero at low bias in Fig. 5.7(a-c), but is finite in Fig. 5.7(d,e).

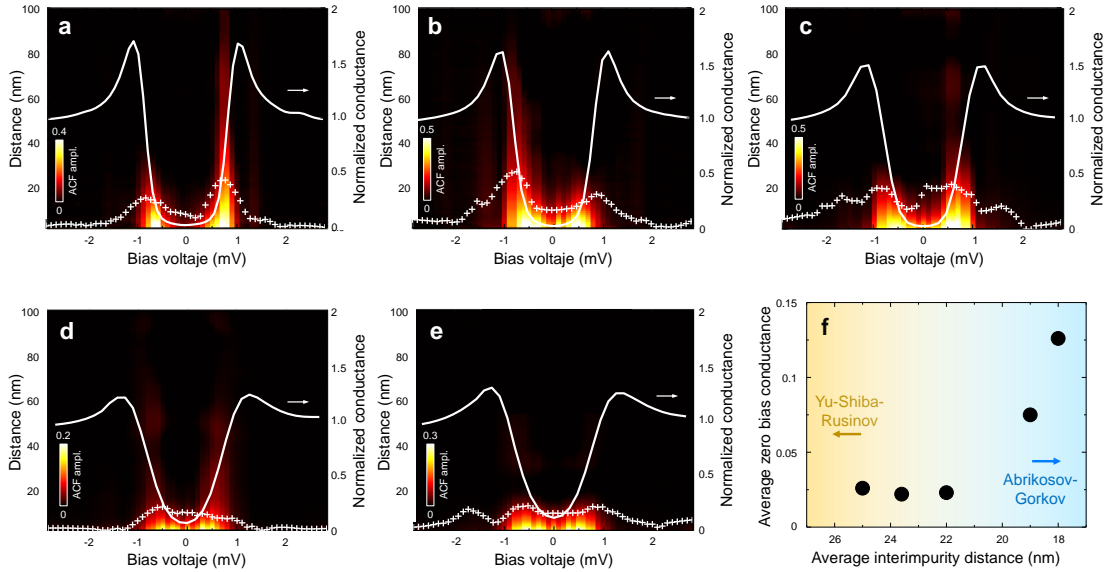


**Figure 5.7:** In (a)-(e) we show the average tunneling conductance over the maps shown in Fig. 5.6 as a white line (right y-axis). We further show as a color scale (from black to yellow, color bars shown in the bottom left of each panel) the  $ACF$  of the image in each case as a function of the distance  $r$  (left y-axis). We mark with white crosses line the decay length obtained from an exponential fit to  $ACF(r)$  as a function of the bias voltage (left y-axis). In (f) we show the average zero bias conductance as a function of the average interimpurity distance, as a measure of the surface density of Fe, in different fields of view.

## 5.2.4 Discussion

In summary, we observe that YSR impurities in  $2\text{H-NbSe}_{1.8}\text{S}_{0.2}$  present a behavior that is substantially different from the behavior observed previously in  $2\text{H-NbSe}_2$ .

First, the in-plane asymmetry of the YSR states is strongly influenced by the location of randomly placed S atoms around each Fe impurity. This leads to an oscillatory YSR pattern that does not show the sixfold pattern of pure 2H-NbSe<sub>2</sub>. Instead, we observe patterns that are related to particular features of the Fermi surface, due to the  $\Gamma$  and K centered Nb bands. The S induced disorder uncouples layers from each other, favoring an effective reduction of the dimensionality in the YSR oscillatory pattern. As a consequence, we observe oscillatory patterns that extend large distances. In large fields of view, the patterns overlap and provide strongly electron-hole asymmetric tunneling conductance maps, which extend the influence of the magnetic impurities over large areas in the sample. When the number of magnetic impurities becomes large, the overlap also occurs for zero bias, leading effectively to gapless superconductivity.

It is quite remarkable that gapless superconductivity appears with a very small concentration of Fe impurities (0.0003 Fe atoms per unit cell). Our results suggest that reduced dimensionality enhances the effect of magnetic impurities on the density of states of quasi-2D superconductors.

As transition metals are very difficult to chemically separate from each other, it is extremely difficult to obtain samples of Nb-based superconductors without a small amount of Fe, Mn or other magnetic transition metal impurities. Thus, the observed gapless superconductivity in the single layer limit of 2H-NbSe<sub>2</sub> could be the result of the enhanced influence of isolated magnetic impurities on the superconducting tunneling conductance.

### 5.3 Vortex cores with magnetic impurities in 2H-NbSe<sub>1.8</sub>S<sub>0.2</sub> and 2H-NbSe<sub>2</sub>

The interaction of YSR states with CdGM states has been largely overlooked, as they have been usually considered independent phenomena ranging their own very different typical sizes. To understand this interaction, we have analyzed results in fields of view where the average distance between impurities was larger than 22 nm, both in 2H-NbSe<sub>2</sub> and in 2H-NbSe<sub>1.8</sub>S<sub>0.2</sub> so that superconductivity is fully gapped.

Although both are essentially perturbations in the superconducting order parameter, the nature of YSR and CdGM states is quite different. YSR states appear at a single or a few subgap energies and exhibit oscillations at the Fermi wavelength  $\lambda_F$  that can be resolved with atomic scale local density of states (LDOS) measurements [194, 210, 50, 211]. By contrast, CdGM states are spin degenerate and form a quasi-continuum with a level separation  $\Delta^2/E_F$  (where  $\Delta$  is the superconducting gap and  $E_F$  is the Fermi energy), which is usually small compared to  $\Delta$ . Thus, their discreteness and their mixed electron hole character only appears at very low temperatures or for  $\Delta \approx E_F$  and in absence of scattering, in the so-called quantum limit [29]. Otherwise, thermal excitations or defects produce dephasing resulting in an electron-hole symmetric LDOS pattern at vortex cores. Thus, in most cases, CdGM states are electron-hole symmetric and their features in the LDOS extend to much larger distances than those of YSR states.

### 5.3.1 Asymmetric vortex cores in presence of magnetic impurities in 2H-NbSe<sub>1.8</sub>S<sub>0.2</sub> and 2H-NbSe<sub>2</sub>

We show vortices in close proximity to YSR impurities in Fig. 5.8(a),(c). When we make the difference between images taken at positive and negative bias voltages,  $\frac{\delta G(\mathbf{r},V)}{G_0} = \frac{G(\mathbf{r},V)-G(\mathbf{r},-V)}{G_0}$  (with  $G_0$  the averaged tunneling conductance for bias voltages above the gap), we observe that vortex cores are not axially symmetric (Fig. 5.8(b) and (d)).

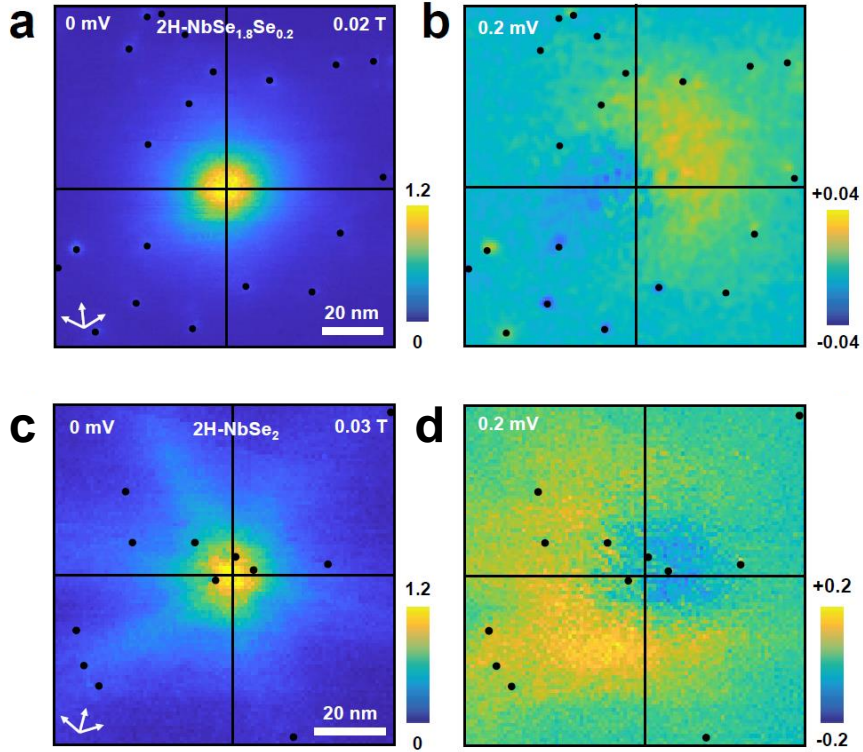


**Figure 5.8:** (a) Zero bias conductance map of a vortex in 2H-NbSe<sub>1.8</sub>S<sub>0.2</sub>. (b) Map showing the difference between the normalized tunneling conductance at positive and negative bias voltages  $\frac{\delta G(\mathbf{r},V)}{G_0} = \frac{G(\mathbf{r},V)-G(\mathbf{r},-V)}{G_0}$  at  $|V|=0.2$  mV and in the same field of view as (a). The same quantities are plotted for 2H-NbSe<sub>2</sub> in (c) and (d). Color scales are given by the bars on the right side of panels (a) and (c) for the zero bias conductance, and on the right side of panels (b) and (d) for  $\frac{\delta G(\mathbf{r},V)}{G_0}$ . Fe impurities are marked by black dots. Vortex centers are at the crossing point between the black lines. White arrows in (a), (c) give the directions of the Se lattice.

Vortex cores in 2H-NbSe<sub>2</sub> have a characteristic star shape while, in contrast, in NbSe<sub>1.8</sub>S<sub>0.2</sub> their cores are completely round, as seen in Fig. 5.8 (c) and (a), respectively. In both cases the energy dependence of the vortex core CdGM states is completely symmetric, as they originate from symmetric gaps, and the spatial dependence follows the axial dependence imposed by the in-plane anisotropies of the material. The inclusion of YSR states in their vicinity however fundamentally

changes their coupling and affects the spatial distribution, causing as we will show a strong axial electron-hole asymmetry.

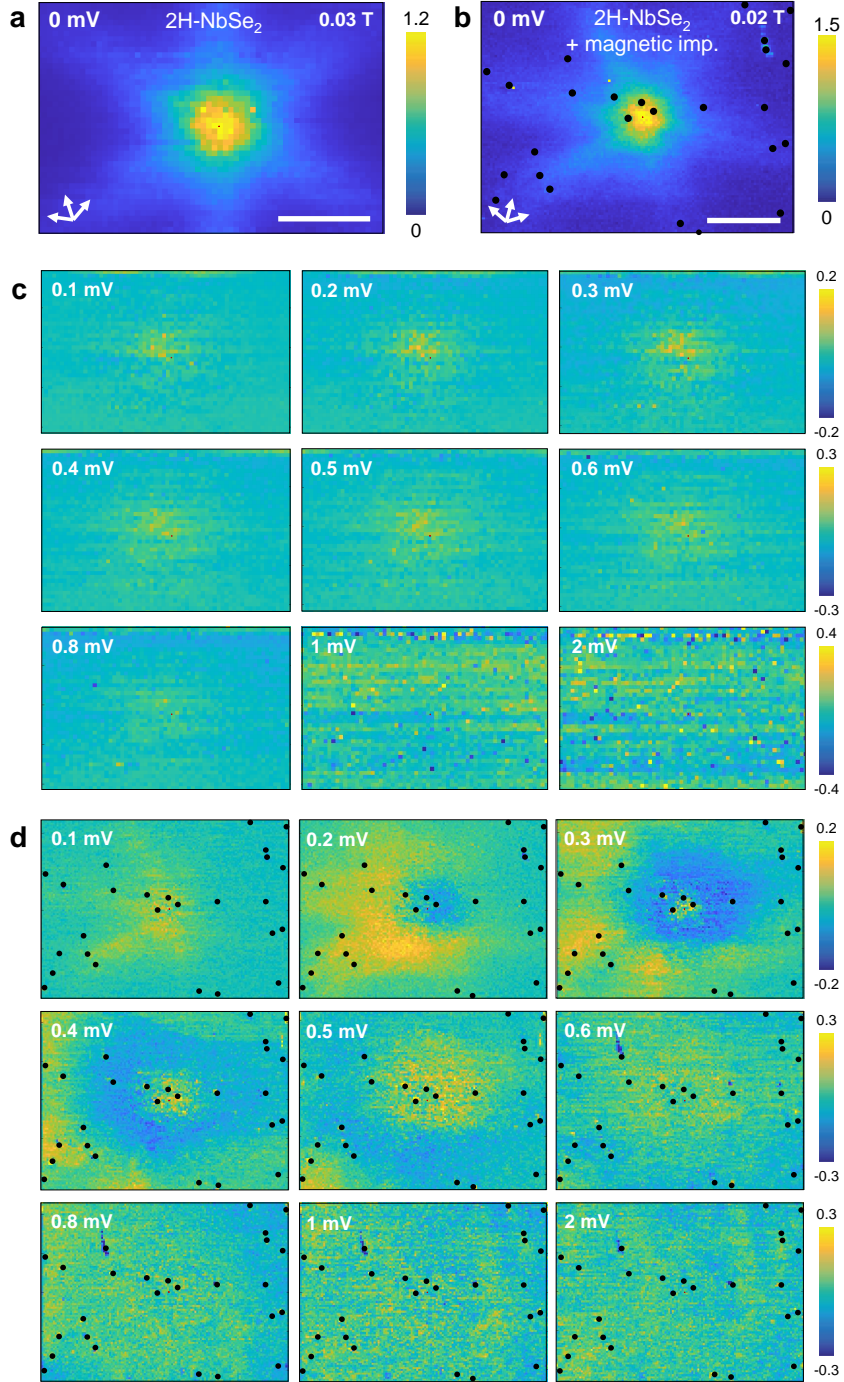


**Figure 5.9:** (a) shows a vortex imaged in a field of view without YSR impurities in 2H-NbSe<sub>2</sub>. We show  $\frac{\delta G(\mathbf{r}, V)}{G_0}$  of this vortex as a function of the bias voltage (indicated in each panel) in (c). In (b) we show the same image as in the previous figure (d) and in (d) we provide  $\frac{\delta G(\mathbf{r}, V)}{G_0}$  as a function of the bias voltage. White scale bars are 20 nm long. The atomic Se lattice directions are shown by white arrows.

We also measured for comparison a spectroscopic map under similar conditions in 2H-NbSe<sub>2</sub> without magnetic impurities. We observe that in this absence of YSR impurities the vortex is, for all  $\frac{\delta G(\mathbf{r},V)}{G_0}$ , axially symmetric. The results are comparatively presented in Fig. 5.9 for the case with and without magnetic impurities.

The asymmetry is thus related to the presence of YSR states close to the vortex cores. As the distribution of Fe impurities is random, the electron-hole asymmetry in vortex cores lying on different places is also different. We can see this in the three vortices imaged in Fig. 5.10.

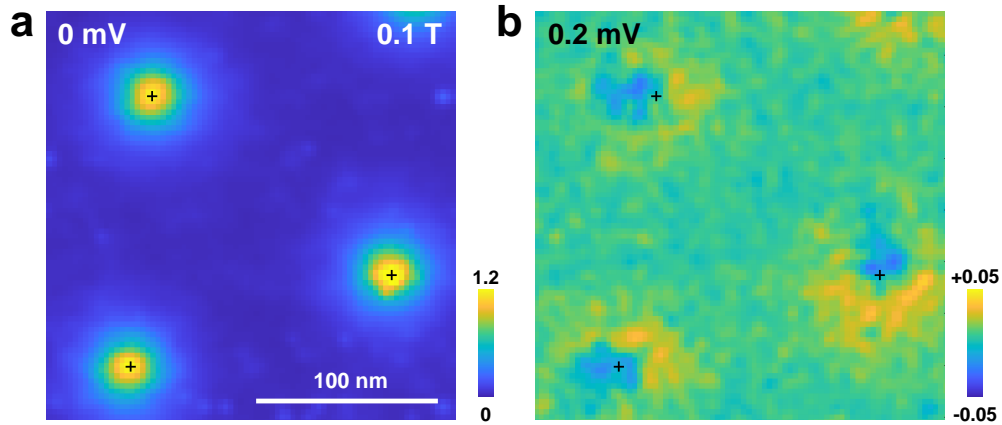


**Figure 5.10:** (a) shows the zero bias conductance map over a very large large surface, such that we can observe three vortices. The center of the vortices is marked with a black cross and the conductance color scale is on the right side. In (b) we show  $\frac{\delta G(\mathbf{r},V)}{G_0}$ , with its scale also on the right. We can observe that the asymmetry axis is different and random for each of the vortices.

### 5.3.2 Theoretical model for the CdGM - YSR coupling

To further understand these features, Sunghun Park and Alfredo Levy Yeyati have made a model where they calculate CdGM states, taking into account the influence of YSR states. The results are shown in Fig. 5.11. We see that they were able to make calculations taking into account the precise positions of the CdGM states we found in the experiment over the whole field of view. We see that the calculations match to a large extent the experiment.

These calculations also bring insight into the origin of the electron-hole asymmetry. It is shown that the asymmetric electron-hole features of the YSR density of states are transferred to the CdGM states.

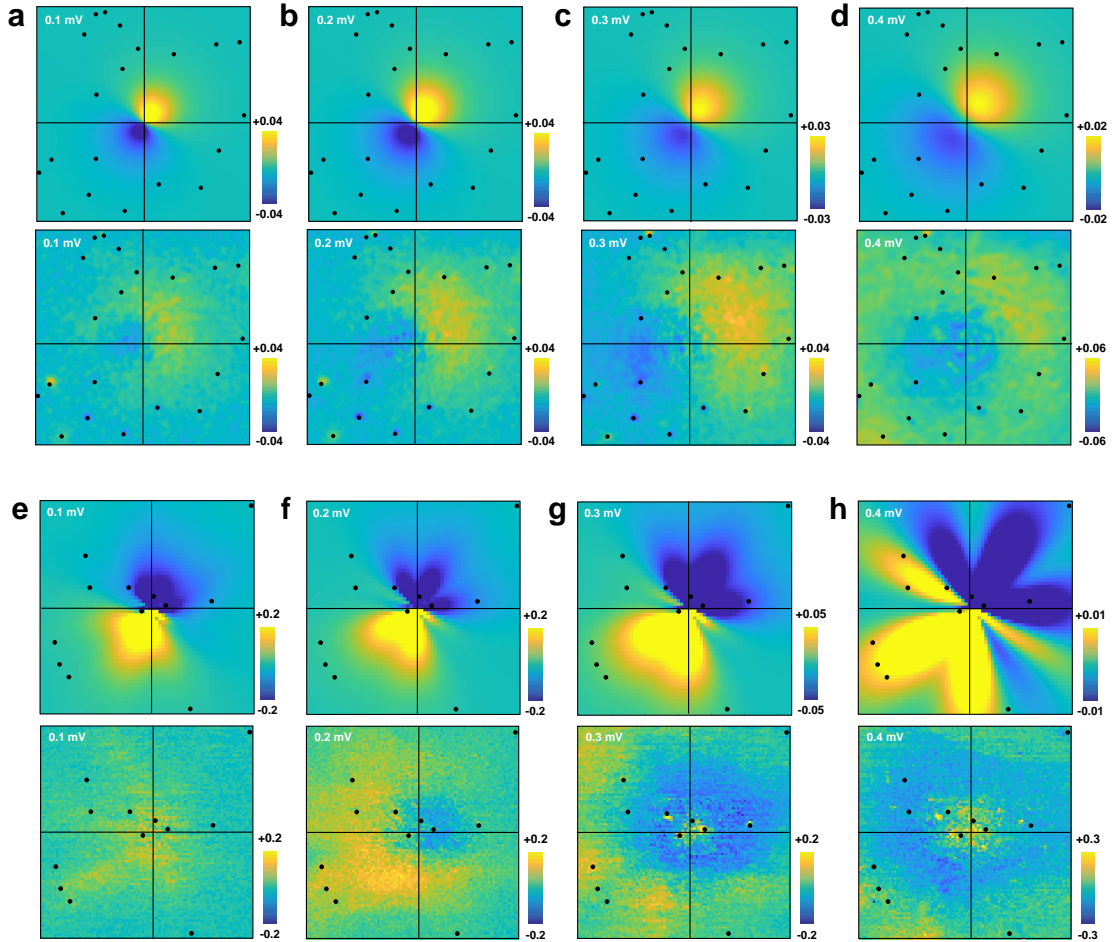


**Figure 5.11:** We show  $\frac{\delta G(\mathbf{r}, V)}{G_0} = \frac{G(\mathbf{r}, V) - G(\mathbf{r}, -V)}{G_0}$  for the bias voltages marked in each panel, obtained from calculations (upper panels) and experiment (lower panels). Black dots provide the position of magnetic impurities. Color scale is given by the bars on the right. (a) to (d) correspond to the  $2H\text{-NbSe}_{1.8}\text{Se}_{0.2}$  sample and (e) to (h) correspond to the  $2H\text{-NbSe}_2$  sample.

### 5.3.3 Discussion

Our combined experimental and theoretical results demonstrate that YSR states couple with CdGM states through exchange interaction and produce electron-hole axially asymmetric vortex cores. This opens the gate to the study of such coupling in other superconductors with different electronic properties. For instance, we propose  $\beta\text{-Bi}_2\text{Pd}$  as a promising candidate system, since both the CdGM states [212, 205, 213] and the YSR states [205] have been extensively characterized but their mutual influence is yet to be addressed.

Bound states in vortex cores have been considered in the past mostly to address the influence of pair potential disturbances on vortex pinning [214]. Our results show nonetheless that the vortex positions are uninfluenced by the presence of magnetic impurities.

As we see in [chapter 3](#), unconventional superconductors like BaFe<sub>2</sub>(As<sub>1-x</sub>P<sub>x</sub>)<sub>2</sub> often show pair breaking at atomic impurities and vortices at the same time [[215](#), [216](#), [112](#), [217](#)]. Our results suggest that vortex bound states might be strongly influenced by such impurities, although a theory for the interplay between YSR and CdGM states with a pairing interaction different from *s*-wave is required to analyze this further.

## 5.4 Conclusion

Our experimental results and supporting calculations show that the S substitution effectively reduces the dimensionality of the electronic band structure in 2H-NbSe<sub>1.8</sub>S<sub>0.2</sub>, increasing its 2D-character and enhancing the electronic interactions with YSR states. We find in 2H-NbSe<sub>1.8</sub>S<sub>0.2</sub> an increased oscillatory component of YSR states that enhances their spatial extension, which is absent in 2H-NbSe<sub>2</sub>. Furthermore, this intensified scattering smears the density of states in regions with a higher surface density of magnetic impurities and eventually closes the gap, realising an effective gapless superconductor.

We also studied the interaction between YSR states and CdGM states at vortex cores. We observe that in the presence of magnetic impurities, CdGM states couple to neighbouring YSR states through exchange interaction and inherit their characteristic electron-hole asymmetry, becoming axially asymmetric.

# 6 | General conclusions

In this Ph.D. thesis we have measured several samples with STM at very low temperatures in order to study their local correlations and electronic properties. This chapter is aimed to review what I think that are the most relevant conclusions of the results presented in this work.

I have used an existing STM setup, which I have considerably modified and improved, achieving results with a much better spatial resolution. Furthermore, I have worked in improving visualization techniques by developing numerical methods that allow rendering relevant phenomena, such as local strain, interference effects and disorder from the images obtained with the STM.

Using these techniques, I have studied the competition between magnetism and superconductivity in  $\text{BaFe}_2(\text{As}_{0.7}\text{P}_{0.3})_2$  and  $\text{BaFe}_2(\text{As}_{0.56}\text{P}_{0.44})_2$ . I have focused my studies in a compound far from the magnetic transition ( $\text{BaFe}_2(\text{As}_{0.56}\text{P}_{0.44})_2$ ) and exactly at the point where it disappears ( $\text{BaFe}_2(\text{As}_{0.7}\text{P}_{0.3})_2$ ), which is also at the QCP. In both cases, I have measured for the first time the vortex lattice and vortex cores, as well as the electronic band structure. As for the vortex lattice, I find a hexagonal lattice in  $\text{BaFe}_2(\text{As}_{0.56}\text{P}_{0.44})_2$  and a square lattice in  $\text{BaFe}_2(\text{As}_{0.7}\text{P}_{0.3})_2$ , with a strong tendency to lock to the crystalline lattice. Also the vortex core shape is square and aligned with the atomic lattice in  $\text{BaFe}_2(\text{As}_{0.7}\text{P}_{0.3})_2$ , while in  $\text{BaFe}_2(\text{As}_{0.56}\text{P}_{0.44})_2$  the vortex cores are round. The magnetic field dependence of the vortex core size shows a completely unexpected and anomalous behavior in  $\text{BaFe}_2(\text{As}_{0.7}\text{P}_{0.3})_2$ . At small magnetic fields, when vortices are isolated, we observe an increase of the vortex core size with the magnetic field, reaching a maximum and then decaying to  $\xi_{H_{c2}}$  at higher fields. In  $\text{BaFe}_2(\text{As}_{0.56}\text{P}_{0.44})_2$  the vortex core size is equal to  $\xi_{H_{c2}}$  and independent of the field. This behavior is related to the diverging mass close to the QCP, which causes the vortex cores to enter the quantum limit in  $\text{BaFe}_2(\text{As}_{0.7}\text{P}_{0.3})_2$  at low fields. Also I have determined the electronic band structure through QPI measurements in  $\text{BaFe}_2(\text{As}_{0.7}\text{P}_{0.3})_2$ , and I found a very anisotropic superconducting gap that together with the V-shaped superconducting density of states at low bias strongly supports the presence of nodes in certain directions of the gap structure.

Then I developed new techniques to better study superconducting properties, addressing in particular the Josephson effect, instead of the density of states. I found a totally unexpected time-dependent behavior in the Josephson current that allows for an improved measurement of the Josephson effect with a STM. This phenomenon is the result of the coupling between the junction and the attached measurement circuit and could be exploited to enhance the sensitivity in Scanning

Josephson Spectroscopy. We provide a detailed analysis and modelling of the results as a delayed feedback driven RCSJ resonator. We show that the oscillatory behavior is a new regime for Josephson junction physics, which might be useful to improve Josephson circuits where the resistance is similar to the resistance of Josephson junctions made with the STM.

I have also studied the problem of isolated YSR magnetic impurities (Fe atoms) in the compounds  $2\text{H-NbSe}_2$  and in  $2\text{H-NbSe}_{1.8}\text{S}_{0.2}$ . I have found that when the concentration of YSR impurities exceeds a certain threshold in  $\text{NbSe}_{1.8}\text{S}_{0.2}$  the perturbation of isolated magnetic impurities on the superconducting properties overlap with each other, with a finite density of states at the Fermi level. A careful analysis of the interference pattern close to YSR impurities in both  $2\text{H-NbSe}_{1.8}\text{S}_{0.2}$  and  $2\text{H-NbSe}_2$  shows that impurity states in  $2\text{H-NbSe}_{1.8}\text{S}_{0.2}$  are connected due to interfering quasiparticles at the inner and outer pockets of the Fermi surface, whereas no such interference is observed in pure  $2\text{H-NbSe}_2$ . Calculations made elsewhere show that the 2D-character of the Fermi surface is considerably enhanced by the S doping. Taking these insights together, I conclude that the enhanced density of states of  $2\text{H-NbSe}_{1.8}\text{S}_{0.2}$  induces an overlapping density of states between magnetic impurities and can lead to a macroscopically finite density of states at the Fermi level and thus to gapless superconductivity.

Finally, I have addressed the behavior of vortex cores in presence of isolated and very diluted YSR impurities. I have carefully characterized the density of states of the vortex cores and found that it is particle-hole axially asymmetric. The asymmetry is present in both  $2\text{H-NbSe}_{1.8}\text{S}_{0.2}$  and  $2\text{H-NbSe}_2$ . Analyzing the properties of isolated YSR impurities at zero field, I have found that the S-induced disorder leads to a reduction in the symmetry of the YSR states from sixfold to threefold. This has allowed validating calculations made elsewhere and estimating the magnetic moment at the Fe impurities from these calculations. To explain the axial particle-hole asymmetry, I have compared my results to a model calculation made elsewhere where the influence of the YSR states in the vortex cores is considered carefully. Our results show that the particle-hole asymmetry of YSR states is transferred to the vortex core states. In all we have been able to show how vortex cores are affected by YSR impurities, unveiling a hitherto unexpected axial asymmetry in the density of states of quantum vortices.

I also would like to mention that I have contributed to the synthesis and characterization of novel superconducting materials, achieving the first large set of superconducting compounds synthesized in the laboratory [83, 84, 85]. Thanks to this effort, I have been able to isolate relevant issues in the materials that I have studied which are due to the synthesis, considerably easing the search for the behavior relevant to the coexistence of superconductivity and magnetism.

# 7 | Conclusiones generales

En esta tesis doctoral hemos medido varias muestras con STM a muy bajas temperaturas con el fin de estudiar sus correlaciones locales y propiedades electrónicas. Este capítulo tiene el objetivo de repasar las que, en mi opinión, son las conclusiones más relevantes presentadas en este trabajo.

Utilizando estas técnicas, he estudiado la competición entre magnetismo y superconductividad en  $\text{BaFe}_2(\text{As}_{0.7}\text{P}_{0.3})_2$  y  $\text{BaFe}_2(\text{As}_{0.56}\text{P}_{0.44})_2$ . He centrado mis estudios en un compuesto alejado de la transición magnética ( $\text{BaFe}_2(\text{As}_{0.56}\text{P}_{0.44})_2$ ) y otro situado justo donde desaparece ( $\text{BaFe}_2(\text{As}_{0.7}\text{P}_{0.3})_2$ ) y se ha sugerido la existencia de un punto crítico cuántico. En ambos compuestos he medido por primera vez la red de vórtices y el tamaño del núcleo de los vórtices, así como la estructura de bandas electrónica. Sobre la red de vórtices, se observa una red hexagonal en  $\text{BaFe}_2(\text{As}_{0.56}\text{P}_{0.44})_2$  y una red cuadrada en  $\text{BaFe}_2(\text{As}_{0.7}\text{P}_{0.3})_2$ , con una fuerte tendencia a alinearse con los ejes cristalinicos. También la forma del núcleo de los vórtices es cuadrada y se alinea con los ejes atómicos en  $\text{BaFe}_2(\text{As}_{0.7}\text{P}_{0.3})_2$ , mientras que en  $\text{BaFe}_2(\text{As}_{0.56}\text{P}_{0.44})_2$  los núcleos son redondos. La dependencia con el campo magnético del tamaño del núcleo de los vórtices muestra un comportamiento inesperado y anómalo en  $\text{BaFe}_2(\text{As}_{0.7}\text{P}_{0.3})_2$ . A campos bajos, cuando los vórtices están alejados, se observa un incremento del tamaño del núcleo con el campo magnético, que alcanza un máximo para luego descender hasta  $\xi_{H_{c2}}$  a campos altos. En  $\text{BaFe}_2(\text{As}_{0.56}\text{P}_{0.44})_2$ , el tamaño del núcleo es igual a  $\xi_{H_{c2}}$  e independiente del campo magnético. Este comportamiento se debe a la divergencia de la masa efectiva cerca del punto crítico cuántico, que provoca que los núcleos de los vórtices en  $\text{BaFe}_2(\text{As}_{0.7}\text{P}_{0.3})_2$  entren en el límite cuántico. También he determinado la estructura de bandas electrónica de  $\text{BaFe}_2(\text{As}_{0.7}\text{P}_{0.3})_2$  a través de medidas de los patrones de interferencia de cuasipartículas, observando un gap superconductor muy anisótropo que, sumado a la forma de V de la densidad de estados a bajas energías confirma la presencia de nodos en ciertas direcciones de la estructura del gap.

He desarrollado nuevas técnicas para mejorar el estudio de las propiedades superconductoras y en particular del efecto Josephson, en lugar de la densidad de estados. He descubierto un comportamiento oscilatorio inesperado de la corriente Josephson que ha permitido mejorar la medida del efecto Josephson con STM. Este fenómeno es el resultado del acoplamiento entre la unión y el circuito de medida asociado y podría explotarse para incrementar la sensibilidad en la espectroscopía Josephson de barrido. He realizado un análisis de los resultados y lo he modelizado como un resonador RCSJ con una retroalimentación retardada. He demostrado que el comportamiento oscilatorio es un nuevo régimen en la física de uniones Josephson, que puede ser útil para mejorar los circuitos Josephson donde la resistencia sea

similar a aquella de las uniones Josephson en un STM.

También he estudiado el problema de impurezas magnéticas YSR aisladas (átomos de Fe) en los compuestos  $2\text{H-NbSe}_2$  y  $2\text{H-NbSe}_{1.8}\text{S}_{0.2}$ . He encontrado que cuando la concentración de impurezas YSR excede un cierto umbral en  $2\text{H-NbSe}_{1.8}\text{S}_{0.2}$ , la perturbación de cada impureza magnética aislada en las propiedades superconductoras solapa con las demás, con una densidad de estados finita en el nivel de Fermi. Un análisis detallado del patrón de interferencia por dispersión cerca de impurezas YSR en ambos compuestos  $2\text{H-NbSe}_2$  y  $2\text{H-NbSe}_{1.8}\text{S}_{0.2}$  muestra que en este último están conectadas con las cuasipartículas dispersadas en las bandas internas y externas de la superficie de Fermi, mientras que en  $2\text{H-NbSe}_2$  puro este fenómeno de interferencia no se observa. Las simulaciones realizadas por otro equipo colaborador muestran que el carácter bidimensional de la superficie de Fermi se ve considerablemente realzado debido al dopaje de S. Teniendo todo esto en cuenta, concluyo que la mayor densidad de estados en  $2\text{H-NbSe}_{1.8}\text{S}_{0.2}$  induce un solape entre las densidades de estados de las impurezas magnéticas y puede conducir macroscópicamente a una densidad de estados finita en el nivel de Fermi y, por consiguiente, a superconductividad sin gap.

Finalmente, he tratado el comportamiento del núcleo de los vórtices en presencia de impurezas magnéticas YSR muy diluidas. He caracterizado con detalle la densidad de estados del núcleo de los vórtices y he encontrado que existe una asimetría axial electrón-hueco. La asimetría está presente tanto en  $2\text{H-NbSe}_{1.8}\text{S}_{0.2}$  como en  $2\text{H-NbSe}_2$ . Analizando las propiedades de impurezas magnéticas YSR aisladas a campo cero, he visto que el desorden asociado al S reduce la simetría de los estados de YSR desde un orden seis a orden tres. Esto ha permitido validar simulaciones realizadas por un equipo colaborador y estimar el momento magnético del Fe en las impurezas. Para explicar la asimetría axial electrón-hueco, he comparado mis resultados con un modelo realizado por otro equipo colaborador donde se considera explícitamente la influencia de cada estado de YSR en el núcleo de los vórtices. Los resultados muestran que la asimetría electrón-hueco de los estados de YSR se transfiere hacia los estados del núcleo de los vórtices. En definitiva, he podido mostrar cómo los vórtices se ven afectados por las impurezas de YSR, descubriendo una hasta ahora desconocida asimetría axial en la densidad de estados de los vórtices cuánticos.

Por último, me gustaría mencionar que también he contribuido a la síntesis y caracterización de nuevos materiales superconductores, habiendo sintetizado un número relevante de compuestos superconductores en el propio laboratorio [83, 84, 85]. Gracias a dicho esfuerzo, he podido aislar cuestiones relevantes en los materiales estudiados de aquellas debidas a la propia síntesis, facilitando considerablemente la búsqueda de comportamientos interesantes para la coexistencia de superconductividad y magnetismo.

# Publications

- S. Park, **V. Barrena**, S. Mañas-Valero, J. Baldoví, A. Fente, E. Herrera, F. Mompeán, M. García-Hernández, A. Rubio, E. Coronado, I. Guillamón, A. Levy Yeyati and H. Suderow, “Coherent coupling between vortex bound states and magnetic impurities in 2D layered superconductors”, *Nat. Comm.* **12** 4668 (2021).
- **V. Barrena et al.**, “Enhanced spatial extension of YSR states in 2H-NbSe<sub>1.8</sub>S<sub>0.2</sub> with magnetic impurities”, in preparation (2022).
- **V. Barrena et al.**, “Low frequency AC Josephson effect in STM with a delayed feedback”, in preparation (2022).
- **V. Barrena et al.**, “Vortex core imaging and QPI close to the quantum critical point in BaFe<sub>2</sub>(As<sub>1-x</sub>P<sub>x</sub>)<sub>2</sub>”, in preparation (2022).
- E. Herrera, **V. Barrena**, I. Guillamón, J. A. Galvis, W. J. Herrera, J. Castilla, D. Aoki, J. Flouquet and H. Suderow, “1D charge density wave in the hidden order state of URu<sub>2</sub>Si<sub>2</sub>”, *Communications Physics* **4** 98 (2021).
- B. Wu, **V. Barrena**, H. Suderow and I. Guillamón, “Huge linear magnetoresistance due to open orbits in  $\gamma$ -Bi<sub>2</sub>Pt”, *Phys. Rev. Research* **2** 022042(R) (2020).
- J. Benito-Llorens, E. Herrera, **V. Barrena**, B. Wu, N. Heinsdorf, V. Borisov, R. Valentí, W.R. Meier, S. Bud’ko, P. C. Canfield, I. Guillamón and H. Suderow, “Anisotropic superconductivity in the spin-vortex antiferromagnetic superconductor CaK(Fe<sub>0.95</sub>Ni<sub>0.05</sub>)<sub>4</sub>As<sub>4</sub>”, *Phys. Rev. B* **103**, L060506 (2021).
- B. Wu, **V. Barrena**, F. Mompeán, M. García-Hernández, H. Suderow and I. Guillamón, “Linear nonsaturating magnetoresistance in the Nowotny chimney ladder compound Ru<sub>2</sub>Sn<sub>3</sub>”, *Phys. Rev. B* **101**, 205123 (2020).
- S. V. Postolova, A. Y. Mironov, **V. Barrena**, J. Benito-Llorens, J. G. Rodrigo, H. Suderow, M. R. Baklanov, T. I. Baturina and V. M. Vinokur, “Superconductivity in a disordered metal with Coulomb interactions”, *Phys. Rev. Research* **2**, 033307 (2020).
- M. Fernández-Lomana, **V. Barrena**, B. Wu, S. Delgado, F. Mompeán, M. García-Hernández, H. Suderow and I. Guillamón, “Large magnetoresistance in the iron-free pnictide superconductor LaRu<sub>2</sub>P<sub>2</sub>”, *Journal of Physics: Condensed Matter*, vol. **33**, number 14 (2021).
- F. Martín-Vega, **V. Barrena**, R. Sánchez-Barquilla, M. Fernández-Lomana, J. Benito-Llorens, B. Wu, A. Fente, D. Perconte-Duplain, I. Horcas, R. López,

## Publications

- J. Blanco, J.A. Higuera, S. Mañas-Valero, N.-H. Jo, J. Schmidt, P.C. Canfield, G. Rubio-Bollinger, J.G. Rodrigo, E. Herrera, I. Guillamón and H. Suderow, “Simplified feedback control system for scanning tunneling microscopy”, *Rev. Sci. Instruments* **92**, 103705 (2021).
- R. Álvarez-Montoya, S. Delgado, J. Castilla, J. Navarrete, N. Díaz-Contreras, J. R. Marijuan, **V. Barrena**, I. Guillamón and H. Suderow, “Methods to simplify cooling of liquid helium cryostats”, *HardwareX* vol. 5, e00058 (2019).

# Bibliography

- [1] H. K. Onnes *Proceedings of the Royal Academy of Arts and Sciences*, vol. 14, p. 818, 1911.
- [2] W. Meissner and R. Ochsenfeld, “Ein neuer Effekt bei Eintritt der Supraleitfähigkeit,” *Naturwissenschaften*, vol. 21, no. 44, pp. 787–788, 1933.
- [3] F. London and H. London, “The electromagnetic equations of the supraconductor,” *Proceedings of the Royal Society of London A: mathematical, physical and engineering sciences*, vol. 149, no. 866, pp. 71–88, 1935.
- [4] L. Landau, “On the theory of phase transitions,” *Zh. Eksp. Teor. Fiz.*, vol. 7, pp. 19–32, 1937.
- [5] L. D. Landau and V. L. Ginzburg, “On the theory of superconductivity,” *Zh. Eksp. Teor. Fiz.*, vol. 20, p. 1064, 1950. in *Collected Papers of L.D. Landau*, Pergamon (1965).
- [6] L. N. Cooper, “Bound electron pairs in a degenerate Fermi gas,” *Phys. Rev.*, vol. 104, pp. 1189–1190, 1956.
- [7] W. Kohn and J. M. Luttinger, “New mechanism for superconductivity,” *Phys. Rev. Lett.*, vol. 15, pp. 524–526, 1965.
- [8] K. Miyake and N. K. Sato, “Unconventional cooper pairing in the superconducting state of UPd<sub>2</sub>Al<sub>3</sub>,” *Phys. Rev. B*, vol. 63, p. 052508, 2001.
- [9] H. Suhl, B. T. Matthias, and L. R. Walker, “Bardeen-Cooper-Schrieffer theory of superconductivity in the case of overlapping bands,” *Phys. Rev. Lett.*, vol. 3, pp. 552–554, 1959.
- [10] G. Rubio-Bollinger, H. Suderow, and S. Vieira, “Tunneling spectroscopy in small grains of superconducting MgB<sub>2</sub>,” *Phys. Rev. Lett.*, vol. 86, no. 24, pp. 5582–5584, 2001.
- [11] P. Martinez-Samper, J. G. Rodrigo, G. Rubio-Bollinger, H. Suderow, S. Vieira, S. Lee, and S. Tajima, “Scanning tunneling spectroscopy in MgB<sub>2</sub>,” *Physica C: Superconductivity*, vol. 385, no. 1–2, pp. 233 – 243, 2003.
- [12] V. G. Kogan, “Macroscopic anisotropy in superconductors with anisotropic gaps,” *Phys. Rev. B*, vol. 66, no. 2, p. 020509, 2002.

## Bibliography

- [13] J. Benito-Llorens, E. Herrera, V. Barrena, B. Wu, N. Heinsdorf, V. Borisov, R. Valentí, W. R. Meier, S. Bud'ko, P. C. Canfield, I. Guillamón, and H. Suderow, “Anisotropic superconductivity in the spin-vortex antiferromagnetic superconductor  $\text{CaK}(\text{Fe}_{0.95}\text{Ni}_{0.05})_4\text{As}_4$ ,” *Phys. Rev. B*, vol. 103, no. 6, p. L060506, 2021.
- [14] I. Guillamón, H. Suderow, S. Vieira, L. Cario, P. Diener, and P. Rodière, “Superconducting density of states and vortex cores of  $2\text{H-NbS}_2$ ,” *Phys. Rev. Lett.*, vol. 101, p. 166407, 2008.
- [15] M. Crespo, H. Suderow, S. Vieira, S. Bud'ko, and P. C. Canfield, “Thermal expansion measured by STM in the magnetic superconductor  $\text{ErNi}_2\text{B}_2\text{C}$ ,” *Physica B: Condensed Matter*, vol. 378-380, pp. 471–472, 2006.
- [16] V. L. Ginzburg, “Ferromagnetic superconductors,” *Soviet Physics JETP*, vol. 4, no. 2, pp. 153–160, 1957.
- [17] A. A. Abrikosov, “On the magnetic properties of superconductors of the second group,” *Zh. Eksp. Teor. Fiz.*, vol. 32, pp. 1442–1452, 1957.
- [18] P. C. Canfield, P. L. Gammel, and D. J. Bishop, “New magnetic superconductors: a toy box for solid-state physicists,” *Physics Today*, vol. 51, no. 10, pp. 40–46, 1998.
- [19] M. R. Eskildsen, A. B. Abrahamsen, D. López, P. L. Gammel, D. J. Bishop, N. H. Andersen, K. Mortensen, and P. C. Canfield, “Flux line lattice reorientation in the borocarbide superconductors with  $H\parallel a$ ,” *Phys. Rev. Lett.*, vol. 86, no. 2, pp. 320–323, 2001.
- [20] A. V. Putilov, C. Di Giorgio, V. L. Vadimov, D. J. Trainer, E. M. Lechner, J. L. Curtis, M. Abdel-Hafiez, O. S. Volkova, A. N. Vasiliev, D. A. Chareev, G. Karapetrov, A. E. Koshelev, A. Y. Aladyshkin, A. S. Mel'nikov, and M. Iavarone, “Vortex-core properties and vortex-lattice transformation in  $\text{FeSe}$ ,” *Phys. Rev. B*, vol. 99, no. 14, p. 144514, 2019.
- [21] V. Barrena *in preparation*, 2021.
- [22] U. Essmann and H. Träuble, “The direct observation of individual flux lines in type II superconductors,” *Physics Letters A*, vol. 24, no. 10, pp. 526 – 527, 1967.
- [23] Y. Fasano and M. Menghini, “Magnetic-decoration imaging of structural transitions induced in vortex matter,” *Supercond. Sci. Technol.*, vol. 21, no. 2, p. 023001, 2008.
- [24] H. F. Hess, R. B. Robinson, R. C. Dynes, J. M. Valles, and J. V. Waszczak, “Scanning-tunneling-microscope observation of the Abrikosov flux lattice and the density of states near and inside a fluxoid,” *Phys. Rev. Lett.*, vol. 62, pp. 214–216, 1989.

## Bibliography

- [25] C. Caroli, P. G. deGennes, and J. Matricon, “Bound fermion states on a vortex line in a type II superconductor,” *Physics Letters*, vol. 9, no. 4, pp. 307 – 309, 1964.
- [26] H. F. Hess, R. B. Robinson, and J. V. Waszczak, “Vortex-core structure observed with a scanning tunneling microscope,” *Phys. Rev. Lett.*, vol. 64, pp. 2711–2714, 1990.
- [27] H. Hess, R. Robinson, and J. Waszczak, “STM spectroscopy of vortex cores and the flux lattice,” *Physica B: Condensed Matter*, vol. 169, no. 1, pp. 422 – 431, 1991.
- [28] F. Gygi and M. Schlüter, “Self-consistent electronic structure of a vortex line in a type-II superconductor,” *Phys. Rev. B*, vol. 43, pp. 7609–7621, 1991.
- [29] N. Hayashi, T. Isoshima, M. Ichioka, and K. Machida, “Low-lying quasiparticle excitations around a vortex core in quantum limit,” *Phys. Rev. Lett.*, vol. 80, pp. 2921–2924, 1998.
- [30] N. Hayashi, M. Ichioka, and K. Machida, “Effects of gap anisotropy upon the electronic structure around a superconducting vortex,” *Phys. Rev. B*, vol. 56, no. 14, pp. 9052–9063, 1997.
- [31] A. Fente, *Visualizing the influence of defects and impurities on pnictide and chalcogenide superconductors*. PhD thesis, Universidad Autónoma de Madrid, 2017.
- [32] S. Park, V. Barrena, S. Mañas Valero, J. J. Baldoví, A. Fente, E. Herrera, F. Mompeán, M. García-Hernández, A. Rubio, E. Coronado, I. Guillamón, A. L. Yeyati, and H. Suderow, “Coherent coupling between vortex bound states and magnetic impurities in 2D layered superconductors,” *Nature Communications*, vol. 12, no. 1, p. 4668, 2021.
- [33] V. G. Kogan and N. V. Zhelezina, “Field dependence of the vortex core size,” *Phys. Rev. B*, vol. 71, p. 134505, 2005.
- [34] A. Fente, E. Herrera, I. Guillamón, H. Suderow, S. Mañas Valero, M. Galbiati, E. Coronado, and V. G. Kogan, “Field dependence of the vortex core size probed by scanning tunneling microscopy,” *Phys. Rev. B*, vol. 94, p. 014517, 2016.
- [35] A. Schmid, “A time dependent Ginzburg-Landau equation and its application to the problem of resistivity in the mixed state,” *Physik der kondensierten Materie*, vol. 5, no. 4, pp. 302–317, 1966.
- [36] J. R. Clem, “Simple model for the vortex core in a type II superconductor,” *Journal of Low Temperature Physics*, vol. 18, no. 5, pp. 427–434, 1975.

## Bibliography

- [37] A. Fente, W. R. Meier, T. Kong, V. G. Kogan, S. L. Bud'ko, P. C. Canfield, I. Guillamón, and H. Suderow, "Influence of multiband sign-changing superconductivity on vortex cores and vortex pinning in stoichiometric high- $T_c$   $\text{CaKFe}_4\text{As}_4$ ," *Phys. Rev. B*, vol. 97, p. 134501, 2018.
- [38] A. Vargunin and M. A. Silaev, "Field dependence of the vortex-core size in dirty two-band superconductors," *Phys. Rev. B*, vol. 100, p. 014516, 2019.
- [39] B. T. Matthias, H. Suhl, and E. Corenzwit, "Spin exchange in superconductors," *Phys. Rev. Lett.*, vol. 1, pp. 92–94, 1958.
- [40] B. T. Matthias, H. Suhl, and E. Corenzwit, "Further experiments concerning the spin-electron interactions in superconductors," *Journal of Physics and Chemistry of Solids*, vol. 13, no. 1, pp. 156 – 159, 1960.
- [41] B. T. Matthias, "Superconductivity and ferromagnetism," *IBM Journal of Research and Development*, vol. 6, no. 2, pp. 250–255, 1962.
- [42] A. A. Abrikosov and L. P. Gor'kov, "Contribution to the theory of superconducting alloys with paramagnetic impurities," *Zh. Eksp. Teor. Fiz.*, vol. 39, pp. 1781–1796, February 1961. English translation: *J. Exptl. Theoret. Phys.*, **12**, 1243 (1961).
- [43] F. Reif and M. A. Woolf, "Energy gap in superconductors containing paramagnetic impurities," *Phys. Rev. Lett.*, vol. 9, pp. 315–316, 1962.
- [44] M. A. Woolf and F. Reif, "Effect of magnetic impurities on the density of states of superconductors," *Phys. Rev.*, vol. 137, pp. A557–A564, 1965.
- [45] S. Skalski, O. Betbeder-Matibet, and P. R. Weiss, "Properties of superconducting alloys containing paramagnetic impurities," *Phys. Rev.*, vol. 136, pp. A1500–A1518, 1964.
- [46] L. Yu, "Bound state in superconductors with paramagnetic impurities," *Acta Physica Sinica*, vol. 21, no. 1, p. 75, 1965.
- [47] H. Shiba, "Classical spins in superconductors," *Progress of Theoretical Physics*, vol. 40, no. 3, pp. 435–451, 1968.
- [48] A. I. Rusinov, "Superconductivity near a paramagnetic impurity," *J. Exptl. Theoret. Phys Lett.*, vol. 9, pp. 85–87, 1968.
- [49] L. Bulaevskii, A. I. Buzdin, M. Kulić, and S. Panjukov, "Coexistence of superconductivity and magnetism theoretical predictions and experimental results," *Advances in Physics*, vol. 34, no. 2, pp. 175–261, 1985.
- [50] G. C. Ménard, S. Guissart, C. Brun, S. Pons, V. S. Stolyarov, F. Debontridder, M. V. Leclerc, E. Janod, L. Cario, D. Roditchev, P. Simon, and T. Cren, "Coherent long-range magnetic bound states in a superconductor," *Nat. Phys.*, vol. 11, no. 12, pp. 1013–1016, 2015.

## Bibliography

- [51] P. J. Ray, “Structural investigation of  $\text{La}_{2-x}\text{Sr}_x\text{CuO}_{4+y}$ ,” Master’s thesis, Niels Bohr Institute, University of Copenhagen, 2015.
- [52] J. I. Shimoyama, “Potentials of iron-based superconductors for practical future materials,” *Superconductor Science and Technology*, vol. 27, no. 4, p. 044002, 2014.
- [53] J. G. Bednorz and K. A. Müller, “Possible highTc superconductivity in the Ba-La-Cu-O system,” *Zeitschrift für Physik B Condensed Matter*, vol. 64, no. 2, pp. 189–193, 1986.
- [54] Y. Kamihara, T. Watanabe, M. Hirano, and H. Hosono, “Iron-based layered superconductor  $\text{La}[\text{O}_{1-x}\text{F}_x]\text{FeAs}$  ( $x = 0.05\text{--}0.12$ ) with  $T_c = 26\text{ K}$ ,” *Journal of the American Chemical Society*, vol. 130, no. 11, pp. 3296–3297, 2008.
- [55] Y. Kamihara, H. Hiramatsu, M. Hirano, R. Kawamura, H. Yanagi, T. Kamiya, and H. Hosono, “Iron-based layered superconductor:  $\text{LaOFeP}$ ,” *Journal of the American Chemical Society*, vol. 128, no. 31, pp. 10012–10013, 2006.
- [56] T. Watanabe, H. Yanagi, T. Kamiya, Y. Kamihara, H. Hiramatsu, M. Hirano, and H. Hosono, “Nickel-based oxyphosphide superconductor with a layered crystal structure,  $\text{LaNiOP}$ ,” *Inorganic Chemistry*, vol. 46, no. 19, pp. 7719–7721, 2007.
- [57] K. Cho, A. Fente, S. Teknowijoyo, M. A. Tanatar, K. R. Joshi, N. M. Nusran, T. Kong, W. R. Meier, U. Kaluarachchi, I. Guillamón, H. Suderow, S. L. Bud’ko, P. C. Canfield, and R. Prozorov, “Nodeless multiband superconductivity in stoichiometric single-crystalline  $\text{CaKFe}_4\text{As}_4$ ,” *Phys. Rev. B*, vol. 95, p. 100502, 2017.
- [58] W. R. Meier, T. Kong, U. S. Kaluarachchi, V. Taufour, N. H. Jo, G. Drachuck, A. E. Böhmer, S. M. Saunders, A. Sapkota, A. Kreyssig, M. A. Tanatar, R. Prozorov, A. I. Goldman, F. F. Balakirev, A. Gurevich, S. L. Bud’ko, and P. C. Canfield, “Anisotropic thermodynamic and transport properties of single-crystalline  $\text{CaKFe}_4\text{As}_4$ ,” *Phys. Rev. B*, vol. 94, p. 064501, 2016.
- [59] J. Paglione and R. L. Greene, “High-temperature superconductivity in iron-based materials,” *Nat Phys*, vol. 6, no. 9, pp. 645–658, 2010.
- [60] A. Chubukov and P. J. Hirschfeld, “Iron-based superconductors, seven years later,” *Physics Today*, vol. 68, no. 6, pp. 46–52, 2015.
- [61] R. M. Fernandes, A. I. Coldea, H. Ding, I. R. Fisher, P. J. Hirschfeld, and G. Kotliar, “Iron pnictides and chalcogenides: a new paradigm for superconductivity,” *Nature*, vol. 601, no. 7891, pp. 35–44, 2022.
- [62] I. I. Mazin, D. J. Singh, M. D. Johannes, and M. H. Du, “Unconventional superconductivity with a sign reversal in the order parameter of  $\text{LaFeAsO}_{1-x}\text{F}_x$ ,” *Phys. Rev. Lett.*, vol. 101, p. 057003, 2008.

## Bibliography

- [63] S. Sachdev, *Quantum Phase Transitions*. Cambridge: Cambridge University Press, 2 ed., 2011.
- [64] T. Shibauchi, A. Carrington, and Y. Matsuda, “A quantum critical point lying beneath the superconducting dome in iron pnictides,” *Annu. Rev. Condens. Matter Phys.*, vol. 5, no. 1, pp. 113–135, 2014.
- [65] B. D. Josephson, “Possible new effects in superconductive tunnelling,” *Physics Letters*, vol. 1, no. 7, pp. 251–253, 1962.
- [66] A. Barone and G. Paterno, *Physics and applications of the Josephson effect*, vol. 1. Wiley Online Library, 1982.
- [67] K. K. Likharev and J. Lukens, “Dynamics of Josephson junctions and circuits,” *Physics Today*, vol. 41, no. 11, p. 122, 1988.
- [68] D. E. McCumber, “Effect of AC impedance on DC voltage-current characteristics of superconductor weak-link junctions,” *Journal of Applied Physics*, vol. 39, no. 7, pp. 3113–3118, 1968.
- [69] W. C. Stewart, “Current-voltage characteristics of Josephson junctions,” *Appl. Phys. Lett.*, vol. 12, no. 8, pp. 277–280, 1968.
- [70] S. Carabello, J. G. Lambert, J. Mlack, W. Dai, Q. Li, K. Chen, D. Cunnane, X. X. Xi, and R. C. Ramos, “Microwave resonant activation in hybrid single-gap/two-gap Josephson tunnel junctions,” *Journal of Applied Physics*, vol. 120, no. 12, p. 123904, 2016.
- [71] S. Manzeli, D. Ovchinnikov, D. Pasquier, O. V. Yazyev, and A. Kis, “2d transition metal dichalcogenides,” *Nature Reviews Materials*, vol. 2, no. 8, p. 17033, 2017.
- [72] D. E. Moncton, J. D. Axe, and F. J. DiSalvo, “Study of superlattice formation in 2H-NbSe<sub>2</sub> and 2H-TaSe<sub>2</sub> by neutron scattering,” *Phys. Rev. Lett.*, vol. 34, pp. 734–737, 1975.
- [73] T. Yokoya, T. Kiss, A. Chainani, S. Shin, M. Nohara, and H. Takagi, “Fermi surface sheet-dependent superconductivity in 2H-NbSe<sub>2</sub>,” *Science*, vol. 294, no. 5551, pp. 2518–2520, 2001.
- [74] H. Suderow, V. G. Tissen, J. P. Brison, J. L. Martínez, and S. Vieira, “Pressure induced effects on the fermi surface of superconducting 2H-NbSe<sub>2</sub>,” *Phys. Rev. Lett.*, vol. 95, p. 117006, 2005.
- [75] V. G. Tissen, M. R. Osorio, J. P. Brison, N. M. Nemes, M. García-Hernández, L. Cario, P. Rodière, S. Vieira, and H. Suderow, “Pressure dependence of superconducting critical temperature and upper critical field of 2H-NbS<sub>2</sub>,” *Phys. Rev. B*, vol. 87, p. 134502, 2013.

## Bibliography

- [76] I. Guillamón, H. Suderow, F. Guinea, and S. Vieira, “Intrinsic atomic-scale modulations of the superconducting gap of 2H-NbSe<sub>2</sub>,” *Phys. Rev. B*, vol. 77, p. 134505, 2008.
- [77] J. Wilson, F. D. Salvo, and S. Mahajan, “Charge-density waves and superlattices in the metallic layered transition metal dichalcogenides,” *Advances in Physics*, vol. 24, no. 2, pp. 117–201, 1975.
- [78] Y. Hamaue and R. Aoki, “Effects of organic intercalation on lattice vibrations and superconducting properties of 2H-NbS<sub>2</sub>,” *Journal of the Physical Society of Japan*, vol. 55, no. 4, pp. 1327–1335, 1986.
- [79] J. A. Galvis, E. Herrera, I. Guillamón, S. Vieira, and H. Suderow, “Vortex cores and vortex motion in superconductors with anisotropic Fermi surfaces,” *Physica C: Superconductivity and its Applications*, vol. 533, pp. 2–8, 2017.
- [80] X. Liu, Y. X. Chong, R. Sharma, and J. C. S. Davis, “Discovery of a Cooper-pair density wave state in a transition-metal dichalcogenide,” *Science*, vol. 372, no. 6549, pp. 1447–1452, 2021.
- [81] M. Chen, Q. Tang, X. Chen, Q. Gu, H. Yang, Z. Du, X. Zhu, E. Wang, Q.-H. Wang, and H.-H. Wen, “Direct visualization of sign-reversal  $s^{\pm}$  superconducting gaps in FeTe<sub>0.55</sub>Se<sub>0.45</sub>,” *Phys. Rev. B*, vol. 99, no. 1, p. 014507, 2019.
- [82] J. A. Galvis, E. Herrera, I. Guillamón, J. Azpeitia, R. F. Luccas, C. Munuera, M. Cuenca, J. A. Higuera, N. Díaz, M. Pazos, M. García-Hernandez, A. Buendía, S. Vieira, and H. Suderow, “Three axis vector magnet set-up for cryogenic scanning probe microscopy,” *Rev. Sci. Instruments*, vol. 86, no. 1, 2015.
- [83] B. Wu, V. Barrena, H. Suderow, and I. Guillamón, “Huge linear magnetoresistance due to open orbits in  $\gamma$ -PtBi<sub>2</sub>,” *Phys. Rev. Research*, vol. 2, p. 022042, 2020.
- [84] B. Wu, V. Barrena, F. Mompeán, M. García-Hernández, H. Suderow, and I. Guillamón, “Linear nonsaturating magnetoresistance in the nowotny chimney ladder compound Ru<sub>2</sub>Sn<sub>3</sub>,” *Phys. Rev. B*, vol. 101, p. 205123, 2020.
- [85] M. Fernández-Lomana, V. Barrena, B. Wu, S. Delgado, F. Mompeán, M. García-Hernández, H. Suderow, and I. Guillamón, “Large magnetoresistance in the iron-free pnictide superconductor LaRu<sub>2</sub>P<sub>2</sub>,” *Journal of Condensed Matter*, vol. 33, no. 14, 2021.
- [86] H. London, ed., *Proceedings of the 2<sup>nd</sup> International Conference on Low Temperature Physics*, (Oxford, UK), Oxford Univ. Press, 1951.
- [87] H. London, G. R. Clarke, and E. Mendoza, “Osmotic pressure of He<sup>3</sup> in liquid He<sup>4</sup>, with proposals for a refrigerator to work below 1°K,” *Phys. Rev.*, vol. 128, pp. 1992–2005, Dec 1962.

## Bibliography

- [88] O. Lounasmaa, *Experimental principles and methods below 1 K*. Academic Press: London and New York, 1974.
- [89] D. O. Edwards, D. F. Brewer, P. Seligman, M. Skertic, and M. Yaqub, “Solubility of He<sup>3</sup> in liquid He<sup>4</sup> at 0°K,” *Phys. Rev. Lett.*, vol. 15, pp. 773–775, 1965.
- [90] I. Guillamón, *Orden y desorden en superconductividad*. PhD thesis, Universidad Autónoma de Madrid, 2009.
- [91] A. Fente, I. Guillamón, S. Ran, S. Vieira, H. Suderow, S. L. Bud’ko, and P. C. Canfield, “Observation of unreconstructed square atomic square lattice in Ca(Fe<sub>0.965</sub>Co<sub>0.035</sub>)<sub>2</sub>As<sub>2</sub> cleaved at very low temperatures,” *Journal of Physics: Conference Series*, vol. 568, no. 2, p. 022046, 2014.
- [92] H. Suderow, I. Guillamón, and S. Vieira, “Compact very low temperature scanning tunneling microscope with mechanically driven horizontal linear positioning stage,” *Rev. Sci. Instruments*, vol. 82, no. 3, 2011.
- [93] R. Álvarez Montoya, S. Delgado, J. Castilla, J. Navarrete, N. D. Contreras, J. R. Marijuan, V. Barrena, I. Guillamón, and H. Suderow, “Methods to simplify cooling of liquid helium cryostats,” *HardwareX*, vol. 5, p. e00058, 2019.
- [94] G. Binnig, H. Rohrer, C. Gerber, and E. Weibel, “Vacuum tunneling,” *Physica B+C*, vol. 109, pp. 2075 – 2077, 1982.
- [95] G. Binnig, H. Rohrer, C. Gerber, and E. Weibel, “Tunneling through a controllable vacuum gap,” *Applied Physics Letters*, vol. 40, no. 2, pp. 178–180, 1982.
- [96] G. Binnig, H. Rohrer, C. Gerber, and E. Weibel, “Surface studies by scanning tunneling microscopy,” *Phys. Rev. Lett.*, vol. 49, pp. 57–61, 1982.
- [97] G. Binnig and H. Rohrer, “Scanning tunneling microscopy,” *Surface Science*, vol. 126, no. 1–3, pp. 236 – 244, 1983.
- [98] J. Bardeen, “Tunnelling from a many-particle point of view,” *Phys. Rev. Lett.*, vol. 6, pp. 57–59, 1961.
- [99] J. Tersoff and D. R. Hamann, “Theory and application for the scanning tunneling microscope,” *Phys. Rev. Lett.*, vol. 50, pp. 1998–2001, 1983.
- [100] J. Tersoff and D. R. Hamann, “Theory of the scanning tunneling microscope,” *Phys. Rev. B*, vol. 31, pp. 805–813, 1985.
- [101] J. Benito-Llorens, *Vortex lattices under stress : visualizing the superconducting vortex lattice in presence of disorder and magnetism*. PhD thesis, Universidad Autónoma de Madrid, 2020.

## Bibliography

- [102] E. Herrera, *Visualizing the influence of the Fermi surface on superconductivity*. PhD thesis, Universidad Autónoma de Madrid, 2016.
- [103] A. Fente, I. Guillamón, S. Ran, S. Vieira, H. Suderow, S. L. Bud'ko, and P. C. Canfield, “Observation of unreconstructed square atomic square lattice in  $\text{Ca}(\text{Fe}_{0.965}\text{Co}_{0.035})_2\text{As}_2$  cleaved at very low temperatures,” *Journal of Physics: Conference Series*, vol. 568, no. 2, p. 022046, 2014.
- [104] P. C. Canfield and Z. Fisk, “Growth of single crystals from metallic fluxes,” *Philosophical Magazine Part B*, vol. 65, no. 6, pp. 1117–1123, 1992.
- [105] P. C. Canfield and I. R. Fisher, “High-temperature solution growth of intermetallic single crystals and quasicrystals,” *Journal of Crystal Growth*, vol. 225, no. 2–4, pp. 155 – 161, 2001. Proceedings of the 12<sup>th</sup> American Conference on Crystal Growth and Epitaxy.
- [106] P. C. Canfield, *Solution Growth of Intermetallic Single Crystals: A Beginner's Guide*, vol. 2 of *Book Series on Complex Metallic Alloys*. Singapore: World Scientific, E. Belin-Ferré ed., 2010.
- [107] A. Iyo, K. Kawashima, T. Kinjo, T. Nishio, S. Ishida, H. Fujihisa, Y. Gotoh, K. Kihou, H. Eisaki, and Y. Yoshida, “New-structure-type Fe-based superconductors:  $\text{CaAFe}_4\text{As}_4$  ( $A = \text{K}, \text{Rb}, \text{Cs}$ ) and  $\text{SrAFe}_4\text{As}_4$  ( $A = \text{Rb}, \text{Cs}$ ),” *Journal of the American Chemical Society*, vol. 138, no. 10, pp. 3410–3415, 2016.
- [108] W. R. Meier, T. Kong, S. L. Bud'ko, and P. C. Canfield, “Optimization of the crystal growth of the superconductor  $\text{CaKFe}_4\text{As}_4$  from solution in the  $\text{FeAs}-\text{CaFe}_2\text{As}_2-\text{KFe}_2\text{As}_2$  system,” *Phys. Rev. Materials*, vol. 1, no. 1, p. 013401, 2017.
- [109] J. G. Analytis, J.-H. Chu, R. D. McDonald, S. C. Riggs, and I. R. Fisher, “Enhanced Fermi-surface nesting in superconducting  $\text{BaFe}_2(\text{As}_{1-x}\text{P}_x)_2$  revealed by the de Haas–van Alphen effect,” *Phys. Rev. Lett.*, vol. 105, no. 20, p. 207004, 2010.
- [110] A. Damascelli, Z. Hussain, and Z.-X. Shen, “Angle-resolved photoemission studies of the cuprate superconductors,” *Rev. Mod. Phys.*, vol. 75, pp. 473–541, 2003.
- [111] J. E. Hoffman, K. McElroy, D. H. Lee, K. M. Lang, H. Eisaki, S. Uchida, and J. C. Davis, “Imaging quasiparticle interference in  $\text{Bi}_2\text{Sr}_2\text{CaCu}_2\text{O}_{8+\delta}$ ,” *Science*, vol. 297, pp. 1148–1151, 2002.
- [112] M. P. Allan, T.-M. Chuang, F. Masee, Y. Xie, N. Ni, S. L. Bud'ko, G. S. Boebinger, Q. Wang, D. S. Dessau, P. C. Canfield, M. S. Golden, and J. C. Davis, “Anisotropic impurity states, quasiparticle scattering and nematic transport in underdoped  $\text{Ca}(\text{Fe}_{1-x}\text{Co}_x)_2\text{As}_2$ ,” *Nat. Phys.*, vol. 9, no. 4, pp. 220–224, 2013.

## Bibliography

- [113] L. Petersen, P. T. Sprunger, P. Hofmann, E. Lægsgaard, B. G. Briner, M. Doering, H.-P. Rust, A. M. Bradshaw, F. Besenbacher, and E. W. Plummer, “Direct imaging of the two-dimensional Fermi contour: Fourier-transform STM,” *Phys. Rev. B*, vol. 57, pp. R6858–R6861, 1998.
- [114] M. F. Crommie, C. P. Lutz, and D. M. Eigler, “Imaging standing waves in a two-dimensional electron gas,” *Nature*, vol. 363, no. 6429, pp. 524–527, 1993.
- [115] Y. Hasegawa and P. Avouris, “Direct observation of standing wave formation at surface steps using scanning tunneling spectroscopy,” *Phys. Rev. Lett.*, vol. 71, pp. 1071–1074, 1993.
- [116] J. E. Hoffman, *A search for alternative electronic order in the high temperature superconductor  $\text{Bi}_2\text{Sr}_2\text{CaCu}_2\text{O}_{8+\delta}$  by scanning tunneling microscopy*. PhD thesis, University of California, Berkeley, 2003.
- [117] P. J. Hirschfeld, D. Altenfeld, I. Eremin, and I. I. Mazin, “Robust determination of the superconducting gap sign structure via quasiparticle interference,” *Phys. Rev. B*, vol. 92, p. 184513, 2015.
- [118] N. V. Khotkevych-Sanina, Y. A. Kolesnichenko, and J. M. van Ruitenbeek, “Fermi surface contours obtained from STM images around surface point defects,” *New J. Phys.*, vol. 15, p. 123013, 2013.
- [119] S. Lounis, P. Zahn, A. Weismann, M. Wenderoth, R. G. Ulbrich, I. Mertig, P. H. Dederichs, and S. Blügel, “Theory of real space imaging of Fermi surfaces,” *Phys. Rev. B*, vol. 83, p. 035427, 2011.
- [120] A. Weismann, M. Wenderoth, S. Lounis, P. Zahn, N. Quaas, R. G. Ulbrich, P. H. Dederichs, and S. Blügel, “Seeing the Fermi surface in real space by nanoscale electron focusing,” *Science*, vol. 323, no. 5918, pp. 1190–1193, 2009.
- [121] J. E. Hoffman, “Spectroscopic scanning tunneling microscopy insights into Fe-based superconductors,” *Reports on Progress in Physics*, vol. 74, no. 12, p. 124513, 2011.
- [122] F. Martín-Vega, V. Barrena, R. Sánchez-Barquilla, M. Fernández-Lomana, J. Benito Llorens, B. Wu, A. Fente, D. Perconte Duplain, I. Horcas, R. López, J. Blanco, J. A. Higuera, S. Mañas-Valero, N. H. Jo, J. Schmidt, P. C. Canfield, G. Rubio-Bollinger, J. G. Rodrigo, E. Herrera, I. Guillamón, and H. Suderow, “Simplified feedback control system for scanning tunneling microscopy,” *Rev. Sci. Instruments*, vol. 92, no. 10, p. 103705, 2021.
- [123] S. V. Postolova, A. Y. Mironov, V. Barrena, J. Benito-Llorens, J. G. Rodrigo, H. Suderow, M. R. Baklanov, T. I. Baturina, and V. M. Vinokur, “Superconductivity in a disordered metal with Coulomb interactions,” *Phys. Rev. Research*, vol. 2, p. 033307, 2020.
- [124] P. Giraldo-Gallo, Y. Zhang, C. Parra, H. Manoharan, M. Beasley, T. Geballe, M. Kramer, and I. Fisher, “Stripe-like nanoscale structural phase separation in superconducting  $\text{BaPb}_{1-x}\text{Bi}_x\text{O}_3$ ,” *Nat Comm*, vol. 6, p. 8231, 2015.

## Bibliography

- [125] M. Fratini, N. Poccia, A. Ricci, G. Campi, M. Burghammer, G. Aeppli, and A. Bianconi, “Scale-free structural organization of oxygen interstitials in  $\text{La}_2\text{CuO}_{4+y}$ ,” *Nature*, vol. 466, no. 7308, pp. 841–844, 2010.
- [126] C. Parra, J. Aristizabal, B. Arce, F. Montero-Silva, S. Lascano, R. Henriquez, P. Lazcano, P. Giraldo-Gallo, C. Ramírez, T. Henrique Rodrigues da Cunha, and A. Barrera de Brito, “Graphene coating as an effective barrier to prevent bacteria-mediated dissolution of gold,” *Metals*, vol. 11, no. 1, 2021.
- [127] B. Li, P. Lu, J. Liu, J. Sun, S. Li, X. Zhu, and H.-H. Wen, “Pressure induced enhancement of superconductivity in  $\text{LaRu}_2\text{P}_2$ ,” *Scientific Reports*, vol. 6, p. 24479, 2016.
- [128] W. Yu, A. A. Aczel, T. J. Williams, S. L. Bud’ko, N. Ni, P. C. Canfield, and G. M. Luke, “Absence of superconductivity in single-phase  $\text{CaFe}_2\text{As}_2$  under hydrostatic pressure,” *Phys. Rev. B*, vol. 79, p. 020511, 2009.
- [129] S. Ran, S. L. Bud’ko, D. K. Pratt, A. Kreyssig, M. G. Kim, M. J. Kramer, D. H. Ryan, W. N. Rowan-Weetaluktuk, Y. Furukawa, B. Roy, A. I. Goldman, and P. C. Canfield, “Stabilization of an ambient-pressure collapsed tetragonal phase in  $\text{CaFe}_2\text{As}_2$  and tuning of the orthorhombic-antiferromagnetic transition temperature by over 70 K via control of nanoscale precipitates,” *Phys. Rev. B*, vol. 83, p. 144517, 2011.
- [130] S. Seo, V. A. Sidorov, H. Lee, D. Jang, Z. Fisk, J. D. Thompson, and T. Park, “Pressure effects on the heavy-fermion antiferromagnet  $\text{CeAuSb}_2$ ,” *Phys. Rev. B*, vol. 85, no. 20, p. 205145, 2012.
- [131] V.-N. Phan, “Superconductivity in Ce-based heavy-fermion systems under high pressure,” *Phys. Rev. B*, vol. 101, no. 24, p. 245120, 2020.
- [132] M. J. Lawler, K. Fujita, J. Lee, A. R. Schmidt, Y. Kohsaka, C. K. Kim, H. Eisaki, S. Uchida, J. C. Davis, J. P. Sethna, and E.-A. Kim, “Intra-unit-cell electronic nematicity of the high- $T_c$  copper-oxide pseudogap states,” *Nature*, vol. 466, no. 7304, pp. 347–351, 2010.
- [133] E. Herrera, V. Barrena, I. Guillamón, J. A. Galvis, W. J. Herrera, J. Castilla, D. Aoki, J. Flouquet, and H. Suderow, “1D charge density wave in the hidden order state of  $\text{URu}_2\text{Si}_2$ ,” *Communications Physics*, vol. 4, no. 1, p. 98, 2021.
- [134] M. Rotter, M. Tegel, D. Johrendt, I. Schellenberg, W. Hermes, and R. Pöttgen, “Spin-density-wave anomaly at 140 K in the ternary iron arsenide  $\text{BaFe}_2\text{As}_2$ ,” *Phys. Rev. B*, vol. 78, no. 2, p. 020503, 2008.
- [135] M. Rotter, M. Pangerl, M. Tegel, and D. Johrendt, “Superconductivity and crystal structures of  $(\text{Ba}_{1-x}\text{K}_x)\text{Fe}_2\text{As}_2$  ( $x=0-1$ ),” *Angewandte Chemie International Edition*, vol. 47, no. 41, pp. 7949–7952, 2008.

## Bibliography

- [136] H. Chen, Y. Ren, Y. Qiu, W. Bao, R. H. Liu, G. Wu, T. Wu, Y. L. Xie, X. F. Wang, Q. Huang, and X. H. Chen, “Coexistence of the spin-density wave and superconductivity in  $(\text{Ba}_{1-x}\text{K}_x)\text{Fe}_2\text{As}_2$ ,” *Europhys. Lett.*, vol. 85, no. 1, p. 17006, 2009.
- [137] A. S. Sefat, R. Jin, M. A. McGuire, B. C. Sales, D. J. Singh, and D. Mandrus, “Superconductivity at 22 K in Co-doped  $\text{BaFe}_2\text{As}_2$  crystals,” *Phys. Rev. Lett.*, vol. 101, p. 117004, 2008.
- [138] S. Kasahara, T. Shibauchi, K. Hashimoto, K. Ikada, S. Tonegawa, R. Okazaki, H. Shishido, H. Ikeda, H. Takeya, K. Hirata, T. Terashima, and Y. Matsuda, “Evolution from non-Fermi- to Fermi-liquid transport via isovalent doping in  $\text{BaFe}_2(\text{As}_{1-x}\text{P}_x)_2$  superconductors,” *Phys. Rev. B*, vol. 81, no. 18, p. 184519, 2010.
- [139] S. Jiang, H. Xing, G. Xuan, C. Wang, Z. Ren, C. Feng, J. Dai, Z. Xu, and G. Cao, “Superconductivity up to 30 K in the vicinity of the quantum critical point in  $\text{BaFe}_2(\text{As}_{1-x}\text{P}_x)_2$ ,” *Journal of Physics: Condensed Matter*, vol. 21, no. 38, p. 382203, 2009.
- [140] K. Hashimoto, K. Cho, T. Shibauchi, S. Kasahara, Y. Mizukami, R. Katsumata, Y. Tsuruhara, T. Terashima, H. Ikeda, M. A. Tanatar, H. Kitano, N. Salovich, R. W. Giannetta, P. Walmsley, A. Carrington, R. Prozorov, and Y. Matsuda, “A sharp peak of the zero-temperature penetration depth at optimal composition in  $\text{BaFe}_2(\text{As}_{1-x}\text{P}_x)_2$ ,” *Science*, vol. 336, no. 6088, pp. 1554–1557, 2012.
- [141] H. Shishido, A. F. Bangura, A. I. Coldea, S. Tonegawa, K. Hashimoto, S. Kasahara, P. M. C. Rourke, H. Ikeda, T. Terashima, R. Settai, Y. Ōnuki, D. Vignolles, C. Proust, B. Vignolle, A. McCollam, Y. Matsuda, T. Shibauchi, and A. Carrington, “Evolution of the fermi surface of  $\text{BaFe}_2(\text{As}_{1-x}\text{P}_x)_2$  on entering the superconducting dome,” *Phys. Rev. Lett.*, vol. 104, no. 5, p. 057008, 2010.
- [142] P. Walmsley, C. Putzke, L. Malone, I. Guillamón, D. Vignolles, C. Proust, S. Badoux, A. I. Coldea, M. D. Watson, S. Kasahara, Y. Mizukami, T. Shibauchi, Y. Matsuda, and A. Carrington, “Quasiparticle mass enhancement close to the quantum critical point in  $\text{BaFe}_2(\text{As}_{1-x}\text{P}_x)_2$ ,” *Phys. Rev. Lett.*, vol. 110, p. 257002, 2013.
- [143] C. Putzke, P. Walmsley, J. D. Fletcher, L. Malone, D. Vignolles, C. Proust, S. Badoux, P. See, H. E. Beere, D. A. Ritchie, S. Kasahara, Y. Mizukami, T. Shibauchi, Y. Matsuda, and A. Carrington, “Anomalous critical fields in quantum critical superconductors,” *Nature Communications*, vol. 5, p. 5679, 2014.
- [144] J. Dai, Q. Si, J.-X. Zhu, and E. Abrahams, “Iron pnictides as a new setting for quantum criticality,” *PNAS*, vol. 106, no. 19273850, pp. 4118–4121, 2009.

## Bibliography

- [145] E. Abrahams and Q. Si, “Quantum criticality in the iron pnictides and chalcogenides,” *Journal of Physics: Condensed Matter*, vol. 23, no. 22, p. 223201, 2011.
- [146] X. Luo, V. Stanev, B. Shen, L. Fang, X. S. Ling, R. Osborn, S. Rosenkranz, T. M. Benseman, R. Divan, W.-K. Kwok, and U. Welp, “Antiferromagnetic and nematic phase transitions in  $\text{BaFe}_2(\text{As}_{1-x}\text{P}_x)_2$  studied by AC microcalorimetry and SQUID magnetometry,” *Phys. Rev. B*, vol. 91, no. 9, p. 094512, 2015.
- [147] S. Kasahara, H. J. Shi, K. Hashimoto, S. Tonegawa, Y. Mizukami, T. Shibauchi, K. Sugimoto, T. Fukuda, T. Terashima, A. H. Nevidomskyy, and Y. Matsuda, “Electronic nematicity above the structural and superconducting transition in  $\text{BaFe}_2(\text{As}_{1-x}\text{P}_x)_2$ ,” *Nature*, vol. 486, no. 7403, pp. 382–385, 2012.
- [148] E. Thewalt, I. M. Hayes, J. P. Hinton, A. Little, S. Patankar, L. Wu, T. Helm, C. V. Stan, N. Tamura, J. G. Analytis, and J. Orenstein, “Imaging anomalous nematic order and strain in optimally doped  $\text{BaFe}_2(\text{As,P})_2$ ,” *Phys. Rev. Lett.*, vol. 121, no. 2, p. 027001, 2018.
- [149] J. Ma, M. Yi, G. Affeldt, I. Hayes, C. Jozwiak, A. Bostwick, E. Rotenberg, J. Analytis, R. Birgeneau, and A. Lanzara, “Spatial nematic fluctuation in  $\text{BaFe}_2(\text{As}_{1-x}\text{P}_x)_2$  revealed by spatially and angle-resolved photoemission spectroscopy,” *Phys. Rev. B*, vol. 101, no. 9, p. 094515, 2020.
- [150] A. P. Dioguardi, T. Kissikov, C. H. Lin, K. R. Shirer, M. M. Lawson, H.-J. Grafe, J.-H. Chu, I. R. Fisher, R. M. Fernandes, and N. J. Curro, “NMR evidence for inhomogeneous nematic fluctuations in  $\text{BaFe}_2(\text{As}_{1-x}\text{P}_x)_2$ ,” *Phys. Rev. Lett.*, vol. 116, no. 10, p. 107202, 2016.
- [151] T. Adachi, M. Nakajima, Y. Gallais, S. Miyasaka, and S. Tajima, “Superconducting gap and nematic resonance at the quantum critical point observed by Raman scattering in  $\text{BaFe}_2(\text{As}_{1-x}\text{P}_x)_2$ ,” *Phys. Rev. B*, vol. 101, no. 8, p. 085102, 2020.
- [152] K. Hashimoto, M. Yamashita, S. Kasahara, Y. Senshu, N. Nakata, S. Tonegawa, K. Ikada, A. Serafin, A. Carrington, T. Terashima, H. Ikeda, T. Shibauchi, and Y. Matsuda, “Line nodes in the energy gap of superconducting  $\text{BaFe}_2(\text{As}_{1-x}\text{P}_x)_2$  single crystals as seen via penetration depth and thermal conductivity,” *Phys. Rev. B*, vol. 81, no. 22, p. 220501, 2010.
- [153] Y. Zhang, Z. R. Ye, Q. Q. Ge, F. Chen, J. Jiang, M. Xu, B. P. Xie, and D. L. Feng, “Nodal superconducting-gap structure in ferropnictide superconductor  $\text{BaFe}_2(\text{As}_{0.7}\text{P}_{0.3})_2$ ,” *Nature Physics*, vol. 8, no. 5, pp. 371–375, 2012.
- [154] M. Yamashita, Y. Senshu, T. Shibauchi, S. Kasahara, K. Hashimoto, D. Watanabe, H. Ikeda, T. Terashima, I. Vekhter, A. B. Vorontsov, and Y. Matsuda, “Nodal gap structure of superconducting  $\text{BaFe}_2(\text{As}_{1-x}\text{P}_x)_2$  from angle-resolved thermal conductivity in a magnetic field,” *Phys. Rev. B*, vol. 84, no. 6, p. 060507, 2011.

## Bibliography

- [155] T. Yoshida, S. Ideta, T. Shimojima, W. Malaeb, K. Shinada, H. Suzuki, I. Nishi, A. Fujimori, K. Ishizaka, S. Shin, Y. Nakashima, H. Anzai, M. Arita, A. Ino, H. Namatame, M. Taniguchi, H. Kumigashira, K. Ono, S. Kasahara, T. Shibauchi, T. Terashima, Y. Matsuda, M. Nakajima, S. Uchida, Y. Tomioka, T. Ito, K. Kihou, C. H. Lee, A. Iyo, H. Eisaki, H. Ikeda, R. Arita, T. Saito, S. Onari, and H. Kontani, “Anisotropy of the superconducting gap in the iron-based superconductor  $\text{BaFe}_2(\text{As}_{1-x}\text{P}_x)_2$ ,” *Scientific Reports*, vol. 4, no. 1, p. 7292, 2014.
- [156] T. Sonobe, T. Shimojima, A. Nakamura, M. Nakajima, S. Uchida, K. Kihou, C. H. Lee, A. Iyo, H. Eisaki, K. Ohgushi, and K. Ishizaka, “Orbital-anisotropic electronic structure in the nonmagnetic state of  $\text{BaFe}_2(\text{As}_{1-x}\text{P}_x)_2$  superconductors,” *Scientific Reports*, vol. 8, no. 1, p. 2169, 2018.
- [157] L. Vinnikov, A. Friedman, I. Felner, A. Troshina, and Y. Yeshurun, “Vortex structure and magnetic properties of  $\text{BaFe}_2(\text{As}_{1-x}\text{P}_x)_2$  single crystals,” *Journal of Physics: Conference Series*, vol. 507, no. 1, p. 012013, 2014.
- [158] Y. Lamhot, A. Yagil, N. Shapira, S. Kasahara, T. Watashige, T. Shibauchi, Y. Matsuda, and O. M. Auslaender, “Local characterization of superconductivity in  $\text{BaFe}_2(\text{As}_{1-x}\text{P}_x)_2$ ,” *Phys. Rev. B*, vol. 91, no. 6, p. 060504, 2015.
- [159] A. Yagil, Y. Lamhot, A. Almoalem, S. Kasahara, T. Watashige, T. Shibauchi, Y. Matsuda, and O. M. Auslaender, “Diamagnetic vortex barrier stripes in underdoped  $\text{BaFe}_2(\text{As}_{1-x}\text{P}_x)_2$ ,” *Phys. Rev. B*, vol. 94, no. 6, p. 064510, 2016.
- [160] H. Nakaoka, Y. Yamakawa, and H. Kontani, “Pairing mechanism for nodal  $s$ -wave superconductivity in  $\text{BaFe}_2(\text{As,P})_2$ : Analysis beyond Migdal-Eliashberg formalism,” *Phys. Rev. B*, vol. 98, no. 12, p. 125107, 2018.
- [161] L. Shan, Y. L. Wang, B. Shen, B. Zeng, Y. Huang, A. Li, D. Wang, H. Yang, C. Ren, Q. H. Wang, S. H. Pan, and H. H. Wen, “Observation of ordered vortices with andreev bound states in  $\text{Ba}_{0.6}\text{K}_{0.4}\text{Fe}_2\text{As}_2$ ,” *Nature Physics*, vol. 7, pp. 325–331, 2011.
- [162] A. Fente, A. Correa-Orellana, A. E. Böhmer, A. Kreyssig, S. Ran, S. L. Bud’ko, P. C. Canfield, F. J. Mompean, M. García-Hernández, C. Munuera, I. Guillamón, and H. Suderow, “Direct visualization of phase separation between superconducting and nematic domains in co-doped  $\text{CaFe}_2\text{As}_2$  close to a first-order phase transition,” *Phys. Rev. B*, vol. 97, no. 1, p. 014505, 2018.
- [163] H. Sakata, M. Oosawa, K. Matsuba, N. Nishida, H. Takeya, and K. Hirata, “Imaging of vortex lattice in single crystal  $\text{YNi}_2\text{B}_2\text{C}$  by STM,” *Physica C: Superconductivity*, vol. 341-348, pp. 1015–1018, 2000.
- [164] S. L. Bud’ko and P. C. Canfield, “Magnetism and superconductivity in rare earth-nickel-borocarbides,” *Comptes Rendus Physique*, vol. 7, no. 1, pp. 56–67, 2006.

## Bibliography

- [165] Y. Wang, P. J. Hirschfeld, and I. Vekhter, “Theory of quasiparticle vortex bound states in iron-based superconductors: Application to scanning tunneling spectroscopy of LiFeAs,” *Phys. Rev. B*, vol. 85, no. 2, p. 020506, 2012.
- [166] V. Grinenko, K. Iida, F. Kurth, D. V. Efremov, S.-L. Drechsler, I. Cherniavskii, I. Morozov, J. Hänisch, T. Förster, C. Tarantini, J. Jaroszynski, B. Maiorov, M. Jaime, A. Yamamoto, I. Nakamura, R. Fujimoto, T. Hatano, H. Ikuta, and R. Hühne, “Selective mass enhancement close to the quantum critical point in  $\text{BaFe}_2(\text{As}_{1-x}\text{P}_x)_2$ ,” *Scientific Reports*, vol. 7, no. 1, p. 4589, 2017.
- [167] M. Chen, X. Chen, H. Yang, Z. Du, X. Zhu, E. Wang, and H.-H. Wen, “Discrete energy levels of caroli-de gennes-matricon states in quantum limit in  $\text{fete0.55se0.45}$ ,” *Nature Communications*, vol. 9, p. 970, Mar 2018.
- [168] T. Yoshida, I. Nishi, S. Ideta, A. Fujimori, M. Kubota, K. Ono, S. Kasahara, T. Shibauchi, T. Terashima, Y. Matsuda, H. Ikeda, and R. Arita, “Two-dimensional and three-dimensional Fermi surfaces of superconducting  $\text{BaFe}_2(\text{As}_{1-x}\text{P}_x)_2$  and their nesting properties revealed by angle-resolved photoemission spectroscopy,” *Phys. Rev. Lett.*, vol. 106, no. 11, p. 117001, 2011.
- [169] J. M. Tranquada, B. J. Sternlieb, J. D. Axe, Y. Nakamura, and S. Uchida, “Evidence for stripe correlations of spins and holes in copper oxide superconductors,” *Nature*, vol. 375, pp. 561–563, 1995.
- [170] J. P. Carbotte, E. Schachinger, and D. N. Basov, “Coupling strength of charge carriers to spin fluctuations in high-temperature superconductors,” *Nature*, vol. 401, pp. 354–356, 1999.
- [171] R. Daou, J. Chang, D. LeBoeuf, O. Cyr-Choinière, F. Laliberté, N. Doiron-Leyraud, B. J. Ramshaw, R. Liang, D. A. Bonn, W. N. Hardy, and L. Taillefer, “Broken rotational symmetry in the pseudogap phase of a high- $T_c$  superconductor,” *Nature*, vol. 463, pp. 519–522, 2010.
- [172] P. Joyez, D. Vion, M. Götz, M. H. Devoret, and D. Esteve, “The Josephson effect in nanoscale tunnel junctions,” *Journal of Superconductivity*, vol. 12, no. 6, pp. 757–766, 1999.
- [173] B. Jäck, M. Eltschka, M. Assig, M. Etzkorn, C. R. Ast, and K. Kern, “Critical Josephson current in the dynamical Coulomb blockade regime,” *Phys. Rev. B*, vol. 93, no. 2, p. 020504, 2016.
- [174] P. Choubey, S. H. Joo, K. Fujita, Z. Du, S. D. Edkins, M. H. Hamidian, H. Eisaki, S. Uchida, A. P. Mackenzie, J. Lee, J. C. S. Davis, and P. J. Hirschfeld, “Atomic-scale electronic structure of the cuprate pair density wave state coexisting with superconductivity,” *PNAS*, vol. 117, no. 26, pp. 14805–14811, 2020.
- [175] M. Ternes, *Scanning tunneling spectroscopy at the single atom scale*. PhD thesis, EPFL, Lausanne, 2006.

## Bibliography

- [176] J. G. Rodrigo, V. Crespo, and S. Vieira, “Josephson current at atomic scale: Tunneling and nanocontacts using a STM,” *Physica C*, vol. 437-438, pp. 270–273, 2006.
- [177] I. Guillamón, H. Suderow, S. Vieira, and P. Rodiere, “Scanning tunneling spectroscopy with superconducting tips of Al,” *Physica C: Superconductivity and its Applications*, vol. 468, no. 7–10, pp. 537 – 542, 2008. Proceedings of the Fifth International Conference on Vortex Matter in Nanostructured Superconductors.
- [178] M. T. Randeria, B. E. Feldman, I. K. Drozdov, and A. Yazdani, “Scanning Josephson spectroscopy on the atomic scale,” *Phys. Rev. B*, vol. 93, no. 16, p. 161115, 2016.
- [179] R. C. Dynes and T. A. Fulton, “Supercurrent density distribution in Josephson junctions,” *Phys. Rev. B*, vol. 3, no. 9, pp. 3015–3023, 1971.
- [180] J. Senkpiel, S. Dambach, M. Etzkorn, R. Drost, C. Padurariu, B. Kubala, W. Belzig, A. L. Yeyati, J. C. Cuevas, J. Ankerhold, C. R. Ast, and K. Kern, “Single channel Josephson effect in a high transmission atomic contact,” *Communications Physics*, vol. 3, no. 1, p. 131, 2020.
- [181] H. Kimura, R. P. Barber, S. Ono, Y. Ando, and R. C. Dynes, “Josephson scanning tunneling microscopy: A local and direct probe of the superconducting order parameter,” *Phys. Rev. B*, vol. 80, no. 14, p. 144506, 2009.
- [182] D. Cho, K. M. Bastiaans, D. Chatzopoulos, G. D. Gu, and M. P. Allan, “A strongly inhomogeneous superfluid in an iron-based superconductor,” *Nature*, vol. 571, no. 7766, pp. 541–545, 2019.
- [183] T. A. Fulton and L. N. Dunkleberger, “Lifetime of the zero-voltage state in Josephson tunnel junctions,” *Broken rotational symmetry in the pseudogap*, vol. 9, no. 11, pp. 4760–4768, 1974.
- [184] J. A. Galvis, P. Rodière, I. Guillamon, M. R. Osorio, J. G. Rodrigo, L. Cario, E. Navarro-Moratalla, E. Coronado, S. Vieira, and H. Suderow, “Scanning tunneling measurements of layers of superconducting  $2h$ - $\text{TaSe}_2$ : Evidence for a zero-bias anomaly in single layers,” *Phys. Rev. B*, vol. 87, no. 9, p. 094502, 2013.
- [185] J. A. Galvis, L. Chiroli, I. Guillamón, S. Vieira, E. Navarro-Moratalla, E. Coronado, H. Suderow, and F. Guinea, “Zero-bias conductance peak in detached flakes of superconducting  $2H$ - $\text{TaS}_2$  probed by Scanning Tunneling Spectroscopy,” *Phys. Rev. B*, vol. 89, no. 22, p. 224512, 2014.
- [186] D. C. Freitas, P. Rodière, M. R. Osorio, E. Navarro-Moratalla, N. M. Nemes, V. G. Tissen, L. Cario, E. Coronado, M. García-Hernández, S. Vieira, M. Núñez-Regueiro, and H. Suderow, “Strong enhancement of

## Bibliography

- superconductivity at high pressures within the charge-density-wave states of 2H-TaS<sub>2</sub> and 2H-TaSe<sub>2</sub>,” *Phys. Rev. B*, vol. 93, no. 18, p. 184512, 2016.
- [187] E. Navarro-Moratalla, J. O. Island, S. Mañas-Valero, E. Pinilla-Cienfuegos, A. Castellanos-Gomez, J. Queda, G. Rubio-Bollinger, L. Chirolli, J. A. Silva-Guillén, N. Agraït, G. A. Steele, F. Guinea, H. S. J. van der Zant, and E. Coronado, “Enhanced superconductivity in atomically thin TaS<sub>2</sub>,” *Nature Communications*, vol. 7, no. 1, p. 11043, 2016.
- [188] V. Vaño, M. Amini, S. C. Ganguli, G. Chen, J. L. Lado, S. Kezilebieke, and P. Liljeroth, “Artificial heavy fermions in a van der Waals heterostructure,” *Nature*, vol. 599, no. 7886, pp. 582–586, 2021.
- [189] X. Xi, Z. Wang, W. Zhao, J.-H. Park, K. T. Law, H. Berger, L. Forró, J. Shan, and K. F. Mak, “Ising pairing in superconducting NbSe<sub>2</sub> atomic layers,” *Nature Physics*, vol. 12, no. 2, pp. 139–143, 2016.
- [190] M. M. Ugeda, A. J. Bradley, Y. Zhang, S. Onishi, Y. Chen, W. Ruan, C. Ojeda-Aristizabal, H. Ryu, M. T. Edmonds, H.-Z. Tsai, A. Riss, S.-K. Mo, D. Lee, A. Zettl, Z. Hussain, Z.-X. Shen, and M. F. Crommie, “Characterization of collective ground states in single-layer NbSe<sub>2</sub>,” *Nature Physics*, vol. 12, no. 1, pp. 92–97, 2016.
- [191] C. Rubio-Verdú, A. M. García-García, H. Ryu, D.-J. Choi, J. Zaldívar, S. Tang, B. Fan, Z.-X. Shen, S.-K. Mo, J. I. Pascual, and M. M. Ugeda, “Visualization of multifractal superconductivity in a two-dimensional transition metal dichalcogenide in the weak-disorder regime,” *Nano Lett.*, vol. 20, no. 7, pp. 5111–5118, 2020.
- [192] Q. Fan, W. H. Zhang, X. Liu, Y. J. Yan, M. Q. Ren, R. Peng, H. C. Xu, B. P. Xie, J. P. Hu, T. Zhang, and D. L. Feng, “Plain s-wave superconductivity in single-layer FeSe on SrTiO<sub>3</sub> probed by scanning tunnelling microscopy,” *Nature Physics*, vol. 11, no. 11, pp. 946–952, 2015.
- [193] H. Suhl and B. T. Matthias, “Impurity scattering in superconductors,” *Phys. Rev.*, vol. 114, pp. 977–988, 1959.
- [194] A. Yazdani, B. A. Jones, C. P. Lutz, M. F. Crommie, and D. M. Eigler, “Probing the local effects of magnetic impurities on superconductivity,” *Science*, vol. 275, no. 5307, pp. 1767–1770, 1997.
- [195] S. Kezilebieke, R. Žitko, M. Dvorak, T. Ojanen, and P. Liljeroth, “Observation of coexistence of Yu-Shiba-Rusinov states and spin-flip excitations,” *Nano Lett.*, vol. 19, no. 7, pp. 4614–4619, 2019.
- [196] S. Kezilebieke, M. Dvorak, T. Ojanen, and P. Liljeroth, “Coupled Yu-Shiba-Rusinov states in molecular dimers on NbSe<sub>2</sub>,” *Nano Lett.*, vol. 18, no. 4, pp. 2311–2315, 2018.

## Bibliography

- [197] J. Senkpiel, C. Rubio-Verdú, M. Etzkorn, R. Drost, L. M. Schoop, S. Dambach, C. Padurariu, B. Kubala, J. Ankerhold, C. R. Ast, and K. Kern, “Robustness of Yu-Shiba-Rusinov resonances in the presence of a complex superconducting order parameter,” *Phys. Rev. B*, vol. 100, p. 014502, 2019.
- [198] E. Liebhaber, S. Acero González, R. Baba, G. Reece, B. W. Heinrich, S. Rohlf, K. Rossnagel, F. von Oppen, and K. J. Franke, “Yu-Shiba-Rusinov states in the charge-density modulated superconductor NbSe<sub>2</sub>,” *Nano Lett.*, vol. 20, no. 1, pp. 339–344, 2020.
- [199] B. E. Feldman, M. T. Randeria, J. Li, S. Jeon, Y. Xie, Z. Wang, I. K. Drozdov, B. Andrei Bernevig, and A. Yazdani, “High-resolution studies of the Majorana atomic chain platform,” *Nature Physics*, vol. 13, no. 3, pp. 286–291, 2017.
- [200] J. Röntynen and T. Ojanen, “Topological superconductivity and high Chern numbers in 2D ferromagnetic Shiba lattices,” *Phys. Rev. Lett.*, vol. 114, no. 23, p. 236803, 2015.
- [201] S. Nadj-Perge, I. K. Drozdov, J. Li, H. Chen, S. Jeon, J. Seo, A. H. MacDonald, B. A. Bernevig, and A. Yazdani, “Observation of Majorana fermions in ferromagnetic atomic chains on a superconductor,” *Science*, vol. 346, no. 6209, pp. 602–607, 2014.
- [202] H. Kim, L. Rózsa, D. Schreyer, E. Simon, and R. Wiesendanger, “Long-range focusing of magnetic bound states in superconducting lanthanum,” *Nature Communications*, vol. 11, no. 1, p. 4573, 2020.
- [203] J. A. Galvis, E. Herrera, C. Berthod, S. Vieira, I. Guillamón, and H. Suderow, “Tilted vortex cores and superconducting gap anisotropy in 2H-NbSe<sub>2</sub>,” *Communications Physics*, vol. 1, no. 1, p. 30, 2018.
- [204] F. Küster, S. Brinker, S. Lounis, S. S. P. Parkin, and P. Sessi, “Long range and highly tunable interaction between local spins coupled to a superconducting condensate,” *Nature Communications*, vol. 12, no. 1, p. 6722, 2021.
- [205] D.-J. Choi, C. G. Fernández, E. Herrera, C. Rubio-Verdú, M. M. Ugeda, I. Guillamón, H. Suderow, J. I. Pascual, and N. Lorente, “Influence of magnetic ordering between Cr adatoms on the Yu-Shiba-Rusinov states of the  $\beta$ -Bi<sub>2</sub>Pd superconductor,” *Phys. Rev. Lett.*, vol. 120, p. 167001, 2018.
- [206] J. Ortuzar, S. Trivini, M. Rouco, J. Zaldivar, J. I. Pascual, and F. S. Bergeret, “Yu-Shiba-Rusinov states in 2D superconductors with arbitrary Fermi contours,” 2021.
- [207] K. Rossnagel, O. Seifarth, L. Kipp, M. Skibowski, D. Voß, P. Krüger, A. Mazur, and J. Pollmann, “Fermi surface of 2H-NbSe<sub>2</sub> and its implications on the charge-density-wave mechanism,” *Phys. Rev. B*, vol. 64, p. 235119, Nov. 2001.

## Bibliography

- [208] J. A. Silva-Guillén, P. Ordejón, F. Guinea, and E. Canadell, “Electronic structure of 2H-NbSe<sub>2</sub> single-layers in the CDW state,” *2D Materials*, vol. 3, no. 3, p. 035028, 2016.
- [209] S. V. Borisenko, A. A. Kordyuk, V. B. Zabolotnyy, D. V. Evtushinsky, T. K. Kim, B. Buchner, A. N. Yaresko, V. D. Borisenko, and H. Berger, “Van Hove singularity as a possible origin of the bandwidth renormalization in layered superconductors,” *Journal of Physics and Chemistry of Solids*, vol. 72, pp. 562–564, 2011.
- [210] M. E. Flatté and J. M. Byers, “Local electronic structure of a single magnetic impurity in a superconductor,” *Phys. Rev. Lett.*, vol. 78, pp. 3761–3764, 1997.
- [211] B. W. Heinrich, J. I. Pascual, and K. J. Franke, “Single magnetic adsorbates on s-wave superconductors,” *Prog. Surf. Sci.*, vol. 93, pp. 1–19, 2018.
- [212] E. Herrera, I. Guillamón, J. A. Galvis, A. Correa, A. Fente, R. F. Lucas, F. J. Mompean, M. García-Hernández, S. Vieira, J. P. Brison, and H. Suderow, “Magnetic field dependence of the density of states in the multiband superconductor  $\beta$ -Bi<sub>2</sub>Pd,” *Phys. Rev. B*, vol. 92, p. 054507, 2015.
- [213] Y.-F. Lv, W.-L. Wang, Y.-M. Zhang, H. Ding, W. Li, L. Wang, K. He, C.-L. Song, X.-C. Ma, and Q.-K. Xue, “Experimental signature of topological superconductivity and Majorana zero modes on  $\beta$ -Bi<sub>2</sub>Pd thin films,” *Science Bulletin*, vol. 62, no. 12, pp. 852–856, 2017.
- [214] A. I. Larkin and Y. N. Ovchinnikov, “Resistance of layered superclean superconductors at low temperatures,” *Phys. Rev. B*, vol. 57, pp. 5457–5465, 1998.
- [215] Ø. Fischer, M. Kugler, I. Maggio-Aprile, C. Berthod, and C. Renner, “Scanning tunneling spectroscopy of high-temperature superconductors,” *Rev. Mod. Phys.*, vol. 79, pp. 353–419, 2007.
- [216] F. Masee, P. O. Sprau, Y.-L. Wang, J. C. S. Davis, G. Ghigo, G. D. Gu, and W.-K. Kwok, “Imaging atomic-scale effects of high-energy ion irradiation on superconductivity and vortex pinning in Fe(Se,Te),” *Science Advances*, vol. 1, no. 4, p. e1500033, 2015.
- [217] X. Chen, W. Duan, X. Fan, W. Hong, K. Chen, H. Yang, S. Li, H. Luo, and H.-H. Wen, “Friedel oscillations of vortex bound states under extreme quantum limit in KCa<sub>2</sub>Fe<sub>4</sub>As<sub>4</sub>F<sub>2</sub>,” *Phys. Rev. Lett.*, vol. 126, no. 25, p. 257002, 2021.